Mach Hawks Anti-Missile Missile Design: The Adder

Authors:

Jayda Hankins
AIAA # 1326156
Jayda M. Hankins

Ryan Hovey
AIAA # 1404959
Ryan Hovey

Addison Fastenau
AIAA # 1810433
Addison M Fastenau

Emily Shaw
AIAA # 1441718
Emily Shaw

Advisor: Dr. Ron Barrett-Gonzalez

AIAA # 022393

Co- Advisor: Dr. Adam Gorrell

AIAA # 211070

Benjamin Smit
AIAA # 1539107
Benjamin Smit

Carson Richardson
AIAA # 1325795

Charles Allen
AIAA # 1341415
Charles Allen

Cover Photo: Adder Missile Render

Acknowledgments

The authors of this report would like to thank the Jayhawk High-Powered Rocketry club for their help advising the project, as well as Dr. Arnold for her advice on the antenna design.

They would also like to thank their advisor and co-advisor, Dr. Barrett and Dr. Gorrell, for their continuous enthusiasm toward the subject matter and valuable insight on various aspects of the design.

Table of Contents

Page Number

Acknowledgments ii

List of Figures vii

List of Symbols vii

1 Introduction, General Concept of Operations, Mission Specification and Profile 1

1.1 Motivation . . . 1

1.2 Concept of Operations (ConOps) . . . 1

1.3 Mission Profile . . . 2

1.4 Mission Specification . . . 3

2 Historical Review, Competition in the Market 5

2.1 Historical Review . . . 5

2.2 Competition in the Market . . . 7

3 Threat Assessment 8

3.1 Artillery Rockets . . . 8

3.2 Glide Bombs . . . 10

3.3 Cruise Missiles . . . 10

3.4 Tactical Ballistic Missiles . . . 12

3.5 Drones . . . 13

3.6 Artillery Shells . . . 14

4 Abbreviated Operating Statement, Design Philosophy, and Configuration Constraints 14

5 Objectives, Requirements, and Design Optimization Function 15
5.1 Requirements . . . 15
5.2 Objectives . . . 16
5.3 Ancillary Objectives . . . 16
5.4 Function . . . 17

6 Compliance Matrix 17

7 STAMPED Analysis 19

8 Candidate Configuration Matrix Establishment 21

9 Application of Optimization Function and Requirements Flow Charts to Configurations and Down-selections 21

10 Weight Sizing 23

11 Powerplant Sizing 24

12 Seeker Selection and Design 25

13 Warhead Design 28

14 GCI and GNC Design 31

15 Class 1 & 2 Stability Analysis 34
15.1 Class 1 Analysis . . . 34
15.2 Class 2 Analysis . . . 39

16 Class 2 Performance Analysis 41

17 Structural Analysis 42

18 3-View, Advanced CAD, Situational Renderings, & Exploded Views 44

19 Manufacturing, Fielding, Logistics, Handling, & Deployment 48
19.1 Fielding and Logistics . . . 53
19.2 Handling and Deployment . . . 54
19.3 Bill of Materials . . . 54

20 Class 2 Cost Analysis 57

References 59

Appendix A: Class 1 Engine Installations

Appendix C: Class I Wing Layout Designs

Appendix C: Class I High Lift Device Sizing

Appendix D: Class I Empennage Design

Appendix E: Class I Landing Gear or Launcher Layout

Appendix F: Weight and Balance Analysis

Appendix G: Class 1 Drag Polar and Performance Analysis

Appendix I: Analysis of Weight and Balance, Stability and Control and L/D Results and Iterations

Appendix I: Class 1 Layout of Major Systems

Appendix K: Class 1 Structural Layout

Appendix K: Fault Tree Analysis

List of Figures

1.2.1 Concept of Operations 1
1.3.1 Nose-On Mission Profile 2
1.3.2 Tail Chase Mission Profile 3
2.1.1 RIM-116 SeaRAM and Aster 15 missiles. 5
2.1.2 Barak 8 and Tamir interceptor missiles. 5
2.1.3 SA-15 Gauntlet and AIM-9X missiles. 6
2.1.4 2K12 Kub and French MICA missiles. 6
2.1.5 FIM-92 Stinger and Umkhonto missile systems. 7
2.1.6 SPYDER and Crotale missile systems. 7
3.1.1 Example Artillery Rocket [1] 8
3.2.1 Example Glide Bomb [2] 10

3.3.1 Example Cruise Missile [3] . . . 10
3.4.1 Example Tactical Ballistic Missile [4] . . . 12
3.5.1 Example Drone [5] . . . 13
3.6.1 Example Artillery Shell [6] . . . 14
4.0.1 Sidewinder with SeaRAM Design Constraints . . . 15
7.0.1 Cost Plotted Against Range. [7] . . . 20
8.0.1 Fins Only Configuration . . . 21
8.0.2 Canard and Fins Configuration . . . 21
8.0.3 Strakes and Fins Configuration . . . 21
8.0.4 Canard Only Configuration . . . 21
8.0.5 Strakes Only Configuration . . . 21
11.0.1 Two-Stage Flight Simulation Generated by OpenRocket [8]. . . . 25
12.0.1 Atmospheric Transmissivity of Infrared Light [9] . . . 26
12.0.2 Diagram of a Threat Entering a Radar Detection Area . . . 27
12.0.3 Arrangement of Forward-Looking Sensors . . . 28
13.0.1 Diagram of vulnerable area of threat missile. . . . 29
13.0.2 Fragmentation area compared to vulnerable area. . . . 30
14.0.1 HFSS Antenna Model . . . 31
14.0.2 Reflected Power Across X-Band . . . 32
14.0.3 Antenna Gain Plot at 9 GHz . . . 32
14.0.4 Antenna Fin Integration . . . 34
15.1.1 Aerodynamic Center and Center of Gravity as a Function of Horizontal Tail Area . . . 36
15.1.2 C.G. of Vertical Tail Distance . . . 37
15.1.3 Directional X-Plot . . . 38
15.2.1 Updated Missile Design . . . 39
15.2.2 Sustainer Only Longitudinal X-Plot . . . 40
15.2.3 Sustainer and Stage Longitudinal X-Plot . . . 41
17.0.1 Finite Element Model of Adder . . . 43
17.0.2 Fringe Plot of Minimum Principal Stress . . . 44
17.0.3 Fringe Plot of Maximum Principal Stress . . . 44
18.0.1 Updated 3-View for Entire Adder Configuration . . . 45
18.0.2 Updated 3-View for Sustainer Only Adder Configuration . . . 45
18.0.3 Explosion View of the Adder . . . 47

18.0.4 Electronics System and Bulkhead Views . . . 47
18.0.5 Adder Sensors . . . 48
18.0.6 Adder Performing Tail Chase with Enemy Threat . . . 48
18.0.7 Adder Loaded in a Humvee . . . 48
18.0.8 Adder Launch . . . 48
18.0.9 Adder Upon Intercept with Enemy Target . . . 48
19.0.1 Manufacturing Floor Plan Floor One . . . 49
19.0.2 Manufacturing Floor Plan Floor Two . . . 50
19.0.3 Domestic Manufacturing Flow-chart . . . 51
19.0.4 Export Manufacturing Flow-chart . . . 51
19.0.5 Materials Breakout for Black Aluminum Version . . . 52
19.0.6 Materials Breakout for Shape Memory Alloy Version . . . 52
19.0.7 Warhead Integration Floor Plan . . . 53
20.0.1 Life-cycle Cost Influence by Phase . . . 57
20.0.2 Annual Life-cycle Cost Contribution . . . 58
20.0.3 Life-cycle Cost Projection by Calendar Year . . . 59
A.1 Proposed Model Rocket Motor . . . B-1
D.1 Class I Empennage Design Concept . . . F-1
F.1 First Stage Subsonic Weight and Balance Analysis . . . F-1
F.2 First Stage Supersonic Weight and Balance Analysis . . . F-2
F.3 Second Stage Subsonic Weight and Balance Analysis . . . F-2
F.4 Second Stage Supersonic Weight and Balance Analysis . . . F-2
F.5 Weight-CG Excursion Diagram . . . G-1
G.1 Perimeter Plot of Fuselage Cross Sections . . . G-2
G.2 Parasite Area Extrapolation . . . G-3
G.3 Supersonic Compressibility Drag Rise . . . G-4
G.4 Subsonic Compressibility Drag Rise . . . G-6
J.1 View of missile ”sleds” on NASAMS canisters [10] . . . J-1
J.2 AeroTech M1419 rocket thrust curve [11] . . . J-3
J.3 Cesaroni N5800 rocket thrust curve [12] . . . J-3
J.4 Electronic System Sizing Side View . . . J-5
J.5 Electronic System Sizing Front View . . . J-5
J.6 Wiring Diagram for Internal Electronic System . . . J-1

J.1 Explosion View of Structural Components K-1
K.1 Top-Level Missile Fault Tree K-1
K.2 Servo Actuator Fault Tree K-2
K.3 Battery Fault Tree K-2
K.4 Seeker Fault Tree K-3
K.5 Motor Fault Tree K-3
K.6 Computer Fault Tree K-3
K.7 Communications Fault Tree K-4
K.8 Uncontrollable Flight Fault Tree K-4

List of Symbols

Acronyms	Definition	Units
AC	Aerodynamic Center	~
AIAA	American Institute of Aeronautics and Astronautics	~
BA	Black Aluminum	~
BOM	Bill of Materials	~
CAD	Computer Aided Design	~
CEP	Circular Error Probable	~
CG	Center of Gravity	~
COTS	Commercial Off-The-Shelf	~
CP	Center of Pressure	~
DEW	Directed Energy Weapon	~
EW	Electronic Warfare	~
FIM	Fired Infrared Missile	~
FEM	Finite Element Model	~
GCI	Ground Control Intercept	~

Acronyms	Definition	Units
GNC	Guidance, Navigation, and Control	~
HELIOS	High Energy Laser with Integrated Optical-dazzler and Surveillance	~
IAI	Israel Aerospace Industries	~
IDF	Israel Defense Forces	~
IMU	Inertial Measurement Unit	~
IOC	Initial Operational Capability	~
IR	Infrared	~
MAD	Massed Aero Defense	~
MICA	Missile d'Interception, de Combat et d'Autodéfense	~
NATO	North Atlantic Treaty Organization	~
PRC	People's Republic of China	~
QA	Quality Assurance	~
RF	Radio Frequency	~
RFP	Request For Proposal	~
RDT&E	Research, Development, Test, and Evaluation	~
SACLOS	Semi-Active Command Line Of Sight	~
SAM	Surface-to-Air Missile	~
SHORAD	Short-Range Air Defense	~
SMA	Shape Memory Alloy	~
SPYDER	Surface-to-Air Python and Derby	~
TVC	Thrust Vector Control	~
UAS	Unmanned Aerial System	~
US/USA	United States of America	~
UV	Ultraviolet	~
VL	Vertical Launch	~

Acronyms	Definition	Units
VLS	Vertical Launch System	~

1. Introduction, General Concept of Operations, Mission Specification and Profile

The American Institute of Aeronautics and Astronautics (AIAA) sets a missile design competition each year. This year, the institute has put forth a low-cost anti-missile missile specification in the short-range air defense (SHORAD) role. The missile must cost less than $10,000 per unit and be able to intercept threats at ranges of 5 miles out and 30,000 feet in altitude. To this end, the Mach Hawks have developed a missile design named the Adder to complete this mission.

1.1. Motivation

As missiles continue to become more inexpensive, it becomes less economically feasible to use high-cost interceptors on these threats. Developing a low-cost anti-missile missile is therefore necessary to counter these threats to leave the more dangerous threats to the more capable missile defense systems. Additionally, developing a low-cost system to provide to allied nations as aid during conflicts such as in Ukraine would decrease the risk of losing advanced technology to an adversarial nation. Such a system could be used to intercept targets that would not be cost-effective to intercept otherwise, such as glide bombs and artillery rockets. It must be able to be launched from both a ground-based and a sea-based platform. Compatibility with existing systems is desired to lower costs and lessen strain on logistics chains.

1.2. Concept of Operations (ConOps)

This section will cover the concept of operations for the proposed missile design. The concept is shown in Figure 1.2.1.

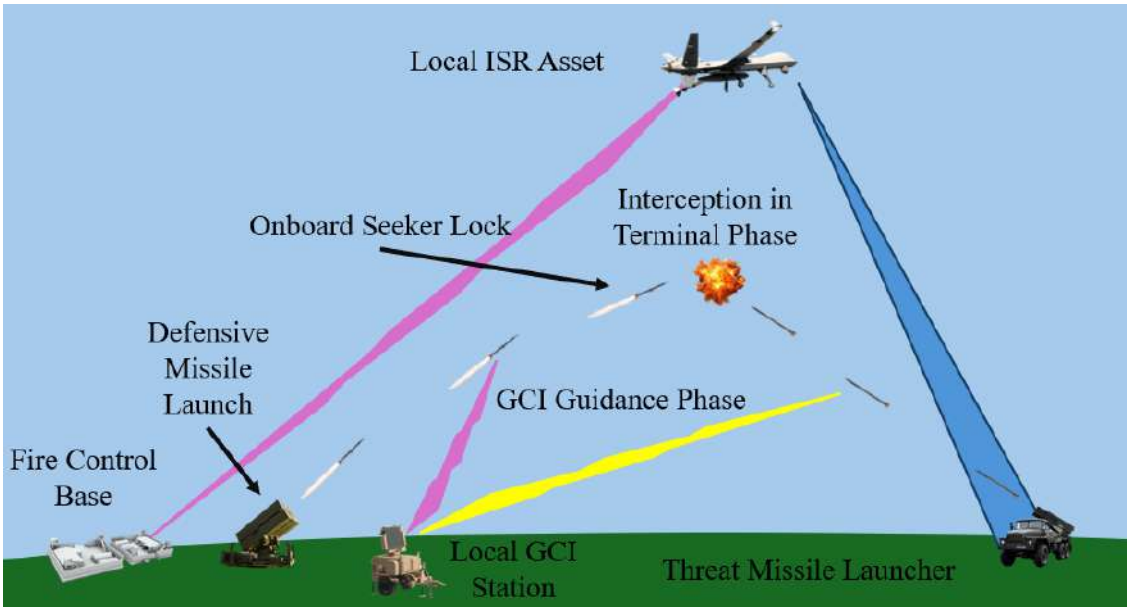

Fig. 1.2.1 Concept of Operations

1.3. Mission Profile

Two mission profiles were created for the proposed missile design which differ in how the targets are acquired and the altitude at which they are intercepted. The first mission profile details a nose-on interception at 30,000 foot altitude, which is the maximum intercept altitude outlined in the request for proposal. This mission profile requires target acquisition with the missile on the ground, and a launch of the missile towards the threat within one second. The missile uses command-link guidance to track the threat until it reaches a range at which the onboard seeker is able to successfully track the threat. At this point, the missile uses terminal guidance to dash out to the target range and altitude, and performs a nose-on interception of the enemy threat. This mission profile is shown in Figure 1.3.1.

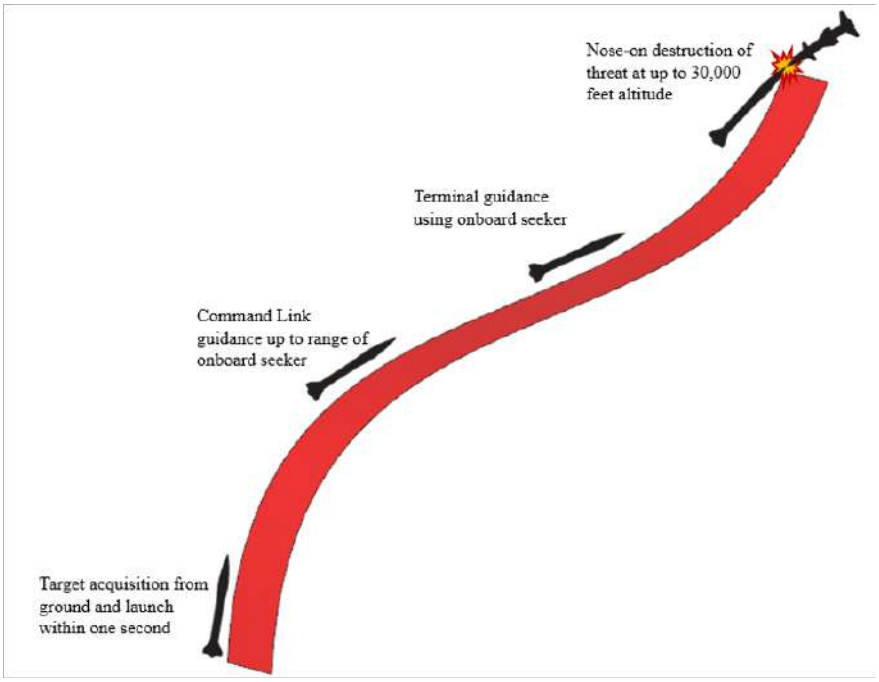

Fig. 1.3.1 Nose-On Mission Profile

The second mission profile details a low-flying tail-chase mission. In this scenario, the missile is again launched from the ground, where it is assumed to overfly the target. This scenario is specific to low-flying threats such as drones, which will not need to be intercepted at the maximum 30,000 foot altitude. The proposed missile will then use down-looking sensors on the nose cone curvature to detect the target. At the point that the target is detected, the missile performs a 180 degree U-turn to enter a tail-chase with the enemy threat. The forward-facing sensors then command the missile to terminal guidance where altitude decreases, before destruction of the threat from its tail. This mission profile is shown in Figure 1.3.2.

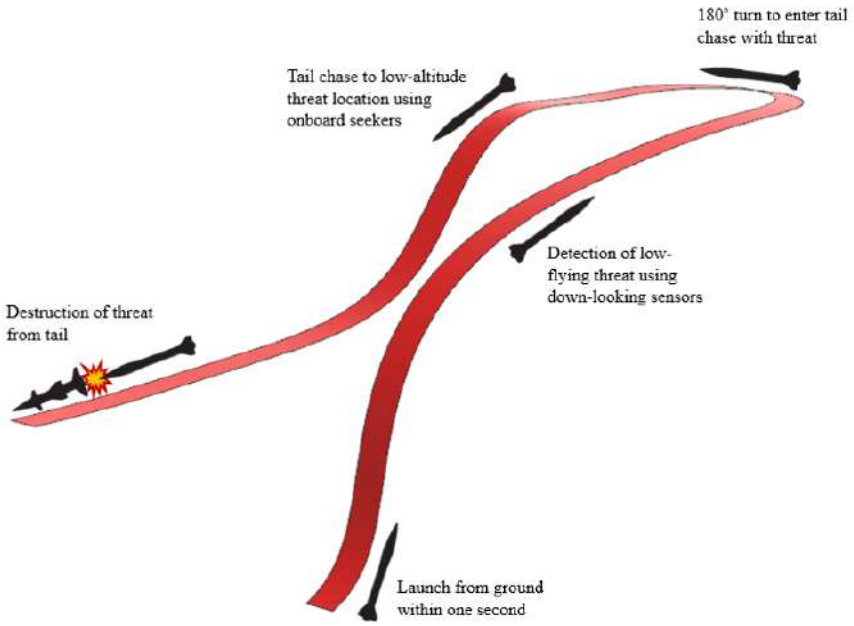

Fig. 1.3.2 Tail Chase Mission Profile

1.4. Mission Specification

The purpose of this section is to provide the specifications of both the anti-missile missile that has been designed by the authors, as well as the target missile that the designed anti-missile missile will intercept. These specifications are given in Table 1.4.1.

Table 1.4.1 Mission Specifications for Low-Cost Anti-Missile Missile [13]

Specification	Description
Interceptor Cost	Should not exceed $10,000 per missile.
Defense Radius	Horizontal defense radius of 5 miles (8 km) with 360° azimuthal coverage.
Engagement Altitude	Maximum engagement altitude of 30,000 feet.

Threat Missile Characteristics	• Ground range: 0.5 to 60 miles (1 to 100 km); • Maneuvering capability: Up to 3 g's of non-ballistic; • Speed: Up to Mach 3; • Unitary missile; • Minimum size range: 4 inches in diameter, 8 feet in length, 100 lbm mass; • Maximum size range: 24 inches in diameter, 20 feet in length, 4000 lbm.
Launch Platforms	• Threshold: Fixed, ground-based launcher installations; • Objective: Mobile ground-based launchers (e.g., trucks or tanks); • Objective: Ship-mounted launchers; • Compatibility with existing launcher systems is desired.
Launch Readiness	Must transition from dormant to launch-ready state in less than 1 second. Battle management system provides threat data just before launch with ±5% error in azimuth, range, altitude, and velocity.
Guidance	May include command data links or in-flight updates, at the team's discretion.
Storage and Maintenance	Must be compatible with safe storage, transportation, and handling for at least 10 years without maintenance.
Production Quantity	1,000 missiles per year for 10 years, plus 100 missiles for developmental testing.
Development Timeline	Design and development start in October 2025, with initial operational capability by December 2030.

2. Historical Review, Competition in the Market

2.1. Historical Review

The following discusses a range of surface-to-air and air-to-air missiles, highlighting their capabilities, history, and key features.

((a)) RIM-116 SeaRAM [14]

((b)) Aster 15 [15]

Fig. 2.1.1 RIM-116 SeaRAM and Aster 15 missiles.

The RIM-116 SeaRAM is a lightweight, quick-reaction, fire-and-forget missile designed to destroy anti-ship cruise missiles and air/surface threats. Developed jointly by the U.S. and German governments, it remains in production with three configurations: Blocks 0, 1A, and 2, producing the RIM-116, RIM-116B, and RIM-116C respectively. Blocks 0 and 1A have completed production, while Block 2 remains in full-rate production.

The Aster 15 missile is engineered to counter threats launched from aircraft and surface vessels in all weather, altitudes, and directions. It can intercept incoming threats traveling up to Mach 2.5 and maneuvering up to 15 g. Capable of Mach 3 in 2.5 seconds, the missile ignites its booster at launch and can fire successive missiles as needed.

((a)) Barak 8 [16]

((b)) Tamir interceptor [17]

Fig. 2.1.2 Barak 8 and Tamir interceptor missiles.

The Barak 8 missile is an enhanced version of Barak 1 featuring an active radar seeker, improved agility, longer range, dual-pulse motor, and two-way data link. It utilizes two sets of unclipped delta-planform folding control fins located near the nose and base. The missile is integrated with Israel Aerospace Industries'

Combat Management System.

The Israeli Tamir interceptor, part of the Iron Dome system, is designed to destroy low-cost threats such as artillery rockets and shells. Costing roughly $50,000 to $100,000 per missile, it is significantly cheaper than comparable systems. It employs command guidance initially before switching to active radar tracking. Reliable details on specifications are limited.

((a)) SA-15 Gauntlet (9K330 Tor) [18]

((b)) AIM-9X Sidewinder [7]

Fig. 2.1.3 SA-15 Gauntlet and AIM-9X missiles.

The 9K330 Tor (NATO SA-15 Gauntlet) is a short-range surface-to-air missile using command link guidance, primarily targeting aircraft and missile threats. It has served extensively in Soviet and Russian forces and abroad.

The AIM-9X Sidewinder is the latest in the AIM-9 series featuring an imaging infrared seeker, thrust vector control, and significant off-boresight targeting capabilities. While primarily air-to-air, it has also been adapted for surface-to-air applications.

((a)) 2K12 Kub (SA-6 Gainful) [19]

((b)) French MICA [20]

Fig. 2.1.4 2K12 Kub and French MICA missiles.

The Soviet-era 2K12 Kub is a mobile, medium-range surface-to-air missile developed in the 1960s. Notable for its success in conflicts like the Yom Kippur and Gulf Wars, it reaches speeds up to Mach 2.8 and employs a semi-active radar seeker with a two-stage solid-propellant system to engage targets up to 24 km away.

The French MICA is a multi-role missile originally developed to replace the Matra Super 530 and later adapted for vertical launch. It achieves speeds up to Mach 3 with 360-degree coverage and is available in two seeker variants: active radar (MICA RF) and passive infrared (MICA IR).

The FIM-92 Stinger is a shoulder-fired, man-portable surface-to-air missile developed by General Dynamics (now Raytheon) for short-range, low-altitude defense. It uses a passive infrared seeker, with some variants adding ultraviolet detection. The Stinger has served effectively since 1981.

((a)) FIM-92 Stinger [21] ((b)) Umkhonto missile system

Fig. 2.1.5 FIM-92 Stinger and Umkhonto missile systems.

The South African Umkhonto missile system, developed by Denel Dynamics, is a vertically launched surface-to-air missile designed for naval and land-based missions. First produced in 2000, it counters modern threats with speeds up to Mach 2 despite its smaller diameter.

((a)) SPYDER missile system [22] ((b)) French Crotale [23]

Fig. 2.1.6 SPYDER and Crotale missile systems.

Developed by Israel's Rafael and Israel Aerospace Industries, the SPYDER system combines Python-5 infrared and Derby active radar-guided missiles for rapid border defense. Ground launch from vehicles enhances its versatility and has been widely adopted.

The French Crotale missile system, developed by Thales around 65 years ago, protects key military sites and convoys. Initially called "Cactus" in South Africa, it evolved through iterations improving range, speed, and capability to counter high-speed threats.

2.2. Competition in the Market

There is significant need for a low-cost anti-missile missile as seen in the Russo-Ukrainian war and the current conflicts between Israel and various non-state actors, and potentially in the future, a conflict with the People's Republic of China (PRC) and the United States (US). Very few systems currently fit this niche, the primary of which being the Tamir interceptor used in Israel's Iron Dome missile defense system. Missile alternatives are also being researched and implemented, such as directed energy weapons. Achieving a cost

of $10,000 per interceptor is difficult as the Tamir, the lowest-cost analog to the request for proposal (RFP) is approximately $40,000-$100,000 per interceptor.

The Tamir, designed jointly by Israeli and American defense firms, is a low-cost anti-missile missile that has had a very high success rate. It has the ability to intercept threats at an approximate 90% success rate which has been proven since its introduction 20 years ago [24]. It is primarily used to shoot down non-maneuvering rockets and artillery shells that travel relatively slowly in the subsonic or transonic regime. Very little information other than its cost, minimum range, and effectiveness is officially published by the Israel Defense Forces (IDF).

Directed Energy Weapons (DEWs) are currently entering service to engage Unmanned Aerial Vehicles (UAVs), Unmanned Surface Vehicles (USVs) and other low-cost systems. Systems such as the High Energy Laser with Integrated Optical-dazzler and Surveillance (HELIOS) and the Iron Beam are notable examples. They function by emitting high-power electromagnetic radiation (typically either visible, infrared, millimeter-wave, or microwave) at a target to dazzle or destroy them outright. As it stands in 2025, however, DEWs have not matured enough to destroy incoming missiles [25].

3. Threat Assessment

This section will cover the potential threats that the missile will encounter in operation. This helps ensure that the missile is tailored to handle a majority of potential threats, ensuring that the missile is designed more specifically as opposed to a generalization of threat attributes. Russian systems are of particular interest to the authors as more information is publicly available than from other nations.

3.1. Artillery Rockets

Fig. 3.1.1 Example Artillery Rocket [1]

Due to the prevalence of rocket artillery and the close match they have with the RFP threat description, they have been determined as the primary threat the anti-missile missile will intercept. An example artillery rocket is shown in Figure 3.1.1. The BM-21 Grad, also referred to as the M-1964, is a Multiple Launch Rocket System which can deliver 122 mm unguided rockets up to a distance of 20 kilometers. Each of these rockets contains 23 kg of incendiary or chemical munitions. The launch system is positioned on a 6x6 all terrain truck. In general, the system contains 40 rocket tubes, though various models can contain anywhere from 12 to 50. The Sakr-18 is a version of the BM-21 and was produced by Egypt. North Korea uses a 30-tube variant known as the BM-11.

Table 3.1.1 BM-21 Specifications [26]

Specification	Value
Artillery Tubes	40
Crew	5
Wheels/Drive	6
Caliber	122 mm
Height	3.1 m
Length	7.4 m
Width	2.4 m

Specification	Value
Weight	13,700 kg
Max Range	450 km
Weapon Range	20,000 m
Power	180 shp
Top Speed	20.9 mps
Setup Time	3 min
Full Load Fire Time	30 sec

The 9K58 Smerch, also referred to as the BM-30, is a rocket launcher artillery system that was made to engage various targets which range from 20 to 70 km. It is able to engage rocket launchers, motors, howitzers, troops, strongholds, both armored and unarmored vehicles, SAM sites as well as other targets in operation. It is mobile on all terrains and is able to operate in a temperature range of -50 to 50 degrees C. The vehicle associated with the Smerch is known as the 9A52-2, it contains 12 300mm rocket tubes which are mounted on its 8x8 wheeled diesel-powered chassis. The Smerch's artillery system is able to fire a total salvo of 12 rounds in 38 seconds. This launch engages an area of 672,000 square meters. The rockets employed on the Smerch are the 9M55 which cover a range of 20 to 90 km.

Table 3.1.2 Smerch Specifications [27]

Specification	Value
Artillery Tubes	12
Crew	4
Wheels/Drive	8
Caliber	300 mm
Height	3 m
Length	12 m
Width	3 m

Specification	Value
Weight	43,700 kg
Max Range	850 km
Weapon Range	70,000 m
Power	518 shp
Cross Country Speed	35 kph
Top Speed	60 kph
Setup Time	3 min

3.2. Glide Bombs

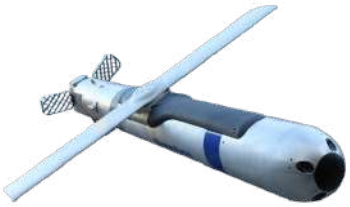

Fig. 3.2.1 Example Glide Bomb [2]

An example glide bomb is shown in Figure 3.2.1. The FAB-500 is a general purpose bomb employed by Russian Air Force tactical fighter aircraft which carries a 500 kg high explosive warhead. The bomb has a single nose fuse with a streamlined, low drag design. A spin off of this is the FAB-500M62 which is a 500 kg aerial bomb that was modified to perform precision strike attack at longer distances by using a glide modification kit. It is intended to be used during the Special Military Operation in Ukraine. The winged bomb was designed to be released by tactical aircraft. The bomb wing kit may feature GLONASS satellite navigation to have enhanced accuracy. It has a range between 70 and 100 km. This is a secondary candidate for interception, as they have low thermal signatures, making them much more difficult to intercept.

Table 3.2.1 FAB-500 and FAB-500M62 Specifications [28]

FAB-500	
Diameter	0.40 m
Length	2.5 m
Weight	500 kg
Explosive Weight	500 kg

FAB-500M62	
Diameter	0.40 m
Length	2.5 m
Weight	500 kg
Explosive Weight	300 kg
Max Range	70 km

3.3. Cruise Missiles

Fig. 3.3.1 Example Cruise Missile [3]

An example cruise missile is shown in Figure 3.3.1. Cruise missiles fit within the size and maneuverability characteristics given by the AIAA RFP, but do not fit within the threat range. They are being included, nonetheless, because the authors believe that little to no changes in the design of the interceptor would have to be made to intercept them. A cruise missile emblematic of what may be encountered by the interceptor is the 3M-14 Kalibr (NATO reporting name SS-N-30 ”Club”, also under the Russian numerical designation 3M-52 in its anti ship version). With a maximum range of at least 1,500 kilometers, it is of a much longer range than

the RFP designates. First entering service in 2015, it is one of the most modern cruise missiles in Russia's inventory. It is a turbojet powered system able to be launched from land, sea, and air. Flying at an altitude 10 to 50 meters and a speed of 180 to 240 meters per second, it makes for a difficult target to intercept. It also accelerates when nearing its target up to Mach 2.8, further complicating interception. Its circular error probable (CEP) is speculated to be 10 meters, making its 200-450 kilogram warhead more than enough to destroy soft and hard targets. Cruise missiles are another high-priority target, as they also closely match the RFP threat description.

Table 3.3.1 Kalibr Specifications [29][30]

Specification	Value
Origin	Russia
Basing	Land, Sea, and Air-Launched
Diameter	0.534–0.645 m
Payload	200–450 kg
Propulsion	Solid propellant

Specification	Value
Class	Cruise Missile
Length	6.2–8.2 m
Launch Weight	1,920 kg
Warhead	High-explosive, submunition
Range	220–2,500 km

The 3M14 Kalibr is a land attack cruise missile (LACM) that originated from Russia as an improvement of the Club. It is a prevalent piece of weaponry in the Russian Navy's ground-strike capabilities. In October of 2015, Russia launched these missiles from naval vessels in the Caspian Sea. They were reported to have flown 1,800 km before reaching their targets.

Table 3.3.2 Kalibr Specifications [31]

Specification	Value
Origin	Russia
Basing	Ship/submarine-based
Payload	450 kg warhead: High explosive, possibly nuclear capable

Specification	Value
Range	1,500 to 2,500 km
Class	Sea-launched Land Attack Cruise Missile
Length	6.2 m
Propulsion	Turbojet

Fig. 3.4.1 Example Tactical Ballistic Missile [4]

An example tactical ballistic missile is shown in Figure 3.4.1. The 9K720 Iskander is a road-mobile short-range ballistic missile that has a range of up to 500 km. It utilizes a common transporter-erector-launcher and support vehicles, the system is able to fire cruise missiles such as the 9M728 and the 9M729. The Iskander flies on a depressed trajectory and is capable of maneuvering up to 30g in flight, it is also accurate to 200 meters CEP with inertial guidance at 300 km range. This lowers to 50 meters with GLONASS satellite guicance and 10 to 20 meters with an optional optical seeker. The optional seeker-equipped warheads can detach in flight and use a digital scene matching area correlation terminal guidance system to detect targets. Iskander's launcher is placed on a MZKT 7930 truck which weighs 43 tons when equipped with two of these missiles. While its characteristics are well beyond the scope of the RFP, the authors have decided that designing the anti-missile missile to intercept TBMs is not of high priority.

Table 3.4.1 Iskander Specifications [32]

Specification	Value
Origin	Russia
Basing	Road-mobile
Diameter	0.92 m
Payload	480–700 kg
Propulsion	Solid propellant

Specification	Value
Class	Short-Range Ballistic Missile (SRBM)
Length	7.3 m
Launch Weight	3,800–4,020 kg
Warhead	High-explosive, submunition, earth-penetrator, thermobaric
Range	400–500 km, 280 km (Export variant)

3.5. Drones

Fig. 3.5.1 Example Drone [5]

An example drone is shown in Figure 3.5.1. The Shahed-136 is a loitering munitions, kamikaze-suicide drone from Iran. It is based on a delta-wing shape design which incorporates a rear-facing pusher-prop arrangement. The nose contains a high explosive fragmentation warhead made of unknown composition and has optics for precision attacks. Its navigation system is simple and inertial with a consumer grade GPS system for tracking. It is available in three models which are anti-personnel and armored vehicle, anti-fortification, and radar seeker versions. It is able to be launched in salvo mode and from a truck and used as a swarm drone, where several drones are launched at the same time and fly in formation controlled from the same station and carry out various tasks. Similarly to glide bombs, they have low thermal signatures, and do not match the RFP description well. Therefore, designing the anti-missile missile to intercept drones is not of a high priority.

Table 3.5.1 Shahed-136 Specifications [33]

Spec	Value
Origin	Iran, Russia
Optics	Photo and video equipment
Warhead	30 to 50 kg high explosive fragmentation
Wingspan	2.5 m

Spec	Value
Weight	200 kg
Speed	185 km/h
Range	1,000 to 2,500 km
Guidance System	Inertial navigation system with GPS

3.6. Artillery Shells

Fig. 3.6.1 Example Artillery Shell [6]

An example artillery shell is shown in Figure 3.6.1. One potential threat the missile could face are large caliber artillery shells. Guns in 152 mm calibers can be found in most of the current and recent conflicts involving at least one regular army. The Soviet-designed M1955 gun-howitzer is well known as a 152 mm artillery piece, it remains in use in most of the current and recent conflicts. The 2S3 Akatsiya is a Soviet-designed self-propelled gun that is currently in service with 18 countries. [34]. Artillery shells are vulnerable to the fuse on the nose, as well as to being destabilized by powerful blasts in flight. However, both of these methods of destruction require a powerful warhead, which may not be feasible to design for. Additionally, they do not fit the RFP threat description well, so they are not given much weight when designing the anti-missile missile.

4. Abbreviated Operating Statement, Design Philosophy, and Configuration Constraints

This section will cover the abbreviated operating statement, design philosophy and configuration constraints. The abbreviated operating statement for this design is Massed Air Defense (MAD), which covers the essential purpose of the missile, to defend against massed threats. The design of our missile system is driven by the principle of affordability without compromising quality or performance. The goal is to produce an extremely cost-effective, reliable, and high-performance missile by leveraging established components wherever possible. While focusing on cost reduction, the team is committed to quality. As such, rigorous testing and adherence to industry standards is required. Innovation is encouraged, promoting original design ideas that enhance performance without increasing cost. We also emphasize sustainability by not only reusing components already in use by the US military, but also with designs that allow easy update and maintenance, ensuring long-term value.

The team will focus on making a missile that can achieve the target unit cost by leveraging mature technologies and utilizing as many commercial off-the-shelf (COTS) or components from existing systems as possible. This will allow the system to be produced in mass quantities in relatively short notice at low cost. However, these parts cannot come with significant risk of failing at a critical time. For example, if the missile would use a component that comes from a potential adversarial nation or if a seeker using civilian components could be easily jammed by electronic warfare (EW) capabilities, it shall be excluded as an option.

Additionally, the dimensions must be limited to fit within a standard cell of a vertical launch system (VLS) or, preferably, to fit within a SeaRAM launch tube to enable its use on a naval vessel. Seen in Figure 4.0.1 below, the design constrains given the SeaRAM application are displayed [35].

Fig. 4.0.1 Sidewinder with SeaRAM Design Constraints

5. Objectives, Requirements, and Design Optimization Function

This section outlines the objective function for the anti-missile missile. The objective function is essential in design engineering as it defines the primary goal of the optimization. It provides a clear metric for evaluating design alternatives, guiding engineers toward solutions that meet project requirements and constraints. The authors have outlined all requirements and objectives and ancillary objectives in the following subsections.

5.1. Requirements

This subsection reviews the requirements, denoted by R, of the mission and their corresponding values.

Requirement Number	Requirement	Values
R_1	Cost $<$ \$10k per missile	$R_1 = \begin{cases} 0 & \text{if cost} > \$10\text{k} \\ 1 & \text{if cost} < \$10\text{k} \end{cases}$
R_2	Horizontal Defense Radius of 5 mi (8 km)	$R_2 = \begin{cases} 0 & \text{if radius} < 5 \text{ mi} \\ 1 & \text{if radius} \geq 5 \text{ mi} \end{cases}$
R_3	360° Azimuthal Coverage	$R_3 = \begin{cases} 0 & \text{if azimuth coverage} < 360\ ^\circ \\ 1 & \text{if azimuth coverage} = 360\ ^\circ \end{cases}$
R_4	Launch in 1 Second or Less	$R_4 = \begin{cases} 0 & \text{if launch time} > 1 \text{ sec} \\ 1 & \text{if launch time} < 1 \text{ sec} \end{cases}$

Requirement Number	Requirement	Values
R_5	Fixed, Ground-Based Launcher Installation	$R_5 = \begin{cases} 0 & \text{if not fixed ground based launcher} \\ 1 & \text{if fixed ground based launcher} \end{cases}$
R_6	Maximum Engagement Altitude of 30,000 ft	$R_6 = \begin{cases} 0 & \text{if altitude} > 30{,}000 \text{ ft} \\ 1 & \text{if altitude} \leq 30{,}000 \text{ ft} \end{cases}$
R_7	System Initial Operational Capacity Occurs in December 2030	$R_7 = \begin{cases} 0 & \text{if ready after Dec. 2030} \\ 1 & \text{if ready by Dec. 2030} \end{cases}$

5.2. Objectives

This subsection reviews the objectives (denoted by O) of the mission and their corresponding values.

Objective Number	Objective	Values
O_1	Mobile, Ground-Based Launchers	$O_1 = \begin{cases} 0 & \text{if not included in design} \\ 1 & \text{if included in design} \end{cases}$
O_2	Ship-Based Launchers	$O_2 = \begin{cases} 0 & \text{if not included in design} \\ 1 & \text{if included in design} \end{cases}$
O_3	Compatibility with Existing Launch Systems	$O_3 = \begin{cases} 0 & \text{if not compatible} \\ 1 & \text{if compatible} \end{cases}$
O_4	Able to Intercept Target at Maximum Altitude and Minimum Range	$O_4 = \begin{cases} 0 & \text{if misses target} \\ 1 & \text{if impacts target within } \pm 5\% \end{cases}$

5.3. Ancillary Objectives

This subsection reviews the ancillary objectives (denoted by AO) of the mission and their corresponding values.

Ancillary Obj. Number	Ancillary Objective	Values
AO_1	Aesthetically Pleasing	$AO_1 = \begin{cases} 0 & \text{if not aesthetically pleasing} \\ 1 & \text{if aesthetically pleasing} \end{cases}$
AO_2	Portable Design	$AO_2 = \begin{cases} 0 & \text{if not portable} \\ 1 & \text{if portable} \end{cases}$
AO_3	Established Components Used to Reduce Cost	$AO_3 = \begin{cases} 0 & \text{if established components} < 50\ \%\ \text{mass} \\ 1 & \text{if established components} > 50\ \%\ \text{mass} \end{cases}$
AO_4	Minimal Maintenance	$AO_4 = \begin{cases} 0 & \text{if high maintenance} \\ 1 & \text{if low maintenance} \end{cases}$
AO_5	Data Links or In-Flight Updates	$AO_5 = \begin{cases} 0 & \text{if no data links/in-flight updates} \\ 1 & \text{if data links/in-flight updates} \end{cases}$
AO_6	Average 90% Probability of Kill	$AO_6 = \begin{cases} 0 & \text{if not capable of achieving a 90\% } P_K \\ 1 & \text{if capable of achieving a 90\% } P_K \end{cases}$

5.4. Function

Equation 6.4.1 shows the objective function used for analysis of designs. The authors weighed the ancillary objectives as the authors felt priority. The weighted values for the ancillary objectives are shown in Equation 6.4.2 which also serves as the expanded version of the objective function.

$$OF = \Pi R_i \Sigma O_j \Sigma AO_k * Weight \tag{6.4.1}$$

$$OF = \left(\sum_{i=1}^{7} R_i\right)\left(\sum_{j=1}^{5} O_j\right) 1AO_1\ 1AO_2\ 0.5AO_3\ 1.5AO_4 \tag{6.4.2}$$

6. Compliance Matrix

The following section shows the compliance matrix demonstrating where the reader can locate the RFP requirements throughout the report. Table 6.0.1 also shows how each requirement is demonstrated in the

report.

Table 6.0.1 RFP Specification Compliance Matrix

RFP Requirement	Demonstrated	Page No.
Technical Requirements		
Missile Cost < $10,000	Cost Analysis and Component Selection	18
Defense Radius 5 mi (8 km)	Trajectory and Performance Calculations	20
360° Azimuth Coverage	Configuration and Control Design	20
Max Engagement Altitude 30,000 ft	Flight Performance Simulation	20
Threat Characteristics (Mach 3, 3g maneuver, Size Range)	Threat Assessment Section	7-10
Launch Readiness in <1 second	Launch System Description	Appendix J.1
Platform Compatibility	Launch System Description	Appendix J.1
Safe Storage for 10+ Years	Manufacturing, Handling and Deployment	Section 19
Data Requirements		
Graphical Representation of Missile	Three-View Drawing	38-39
Analysis of Performance	Figures, Calculations, Trajectory Data	21, 35-36
Aerodynamic Characteristics	Drag Polar Analysis	Appendix H
Guidance and Control Design	Flight Control Systems Section	Appendix J.2
Structural Layout	Structural Layout Section	Appendix K
Weight and Balance	Weight Analysis Section	Appendix G
Development Plan	Development Timeline, Lifecycle Cost Analysis	Section 20

7. STAMPED Analysis

Table 7.0.1 Missile Data Table (Set 1) [36] [37] [38] [39] [40] [41] [42]

Missile	Tamir	SA-15	SeaRAM	AIM-9X
Range	>4 km (>2.5 mi)	12 km (7.5 mi)	9.6 km (6.0 mi)	10 km (6.2 mi)
Seeker Type	SACLOS, active radar	Command guidance	Passive radar homing, IR	IR
g Capability	Unknown	30	20	>9
W_{TO}	90 kg (198 lbs)	165 kg (363 lbs)	73.5 kg (162 lbs)	310 kg (683 lbs)
Max. Mach	Unknown, est. 1-2	2.5	2.5	2+
Diameter	160 mm (6.3 in)	230 mm (9.1 in)	159 mm (6.3 in)	127 mm (5 in)
Length	3 m	2.90 m (9 ft 6 in)	2.82 m (9 ft 3 in)	3.02 m (9 ft 11 in)
Control Type	Unknown	Canards and/or fins	Canards	Canards and TVC
Warhead Weight	11 kg (24 lbs)	14.5 kg (32 lbs)	10 kg (22 lbs)	9.43 kg (21 lbs)
Cost per Missile	$50k-$100k	$202,000	$444,000	$500,000-$750,000

Table 7.0.2 Missile Data Table (Set 2) [42] [43] [44] [45] [46] [47] [48]

Missile	Aster 15	Barak 8	Umkhonto	SPYDER
Range	29.6 km (18.4 mi)	70 km (43.5 mi)	20 km (12 mi)	50 km (31 mi)
Seeker Type	INS active radar	INS active radar	IR	IR and TV or active radar
g Capability	60	Unknown	40	Unknown
W_{TO}	310 kg (683 lbs)	275 kg (606 lbs)	135 kg (298 lbs)	105-118 kg (231-260 lbs)
Max. Mach	3	2	2	4
Diameter	360 mm (14.2 in)	260 mm (10.2 in)	180 mm (7.1 in)	160 mm (6.3 in)
Length	4.2 m (13’ 9.25”)	4.55 m (14’ 11.25”)	3.32 m (10 ft 11 in)	3.1-3.62 m (10 ft 2 in - 11 ft 11 in)
Control Type	Canards	Canards	Canards	Two sets of canards
Warhead Weight	Unknown	60 kg (132 lbs)	23 kg (51 lbs)	11-23 kg (24-51 lbs)
Cost per Missile	Unknown	$1.65M	Unknown	Unknown

Table 7.0.3 Missile Data Table (Set 3) [42] [49] [50] [51] [52] [53] [54] [55] [56]

Missile	Crotale	MICA	SA-6	FIM-92
Range	11 km (6.8 mi)	60 km (37 mi)	24 km (14 mi)	4.8 km (3 mi)
Seeker Type	Command guidance	Passive IR/Active RF	Semi-active radar	Passive IR/UV
g Capability	35	50	Unknown	>4
W_{TO}	76 kg (168 lbs)	112 kg (247 lbs)	59 kg (131 lbs)	10.1 kg (22 lbs)
Max. Mach	3.5	3+	2.8	2.2+
Diameter	165 mm (6.5 in)	160 mm (6.3 in)	335 mm (13.2 in)	70 mm (2.75 in)
Length	2.35 m (7 ft 9 in)	3.1 m (3 ft 3.4 in)	7.4 m (24 ft 3.6 in)	1.5 m (5 ft)
Control Type	Fins	Fins	Canards, Fins	Fins
Warhead Weight	13 kg (28.7 lbs)	12 kg (26.5 lbs)	56 kg (123 lbs)	3 kg (6.6 lbs)
Cost per Missile	Unknown	Unknown	Unknown	$120,000

Figure 7.0.1 plots the range against the unit cost of these systems. Note that cost data for the Umkhonto, SPYDER, MICA, and SA-6 was not able to be found in open source data. Additionally, the range of the Tamir was conservatively approximated as 5 kilometers due to the range of the Iron Dome system being listed as 4-70 kilometers. Across the missiles examined, a clear relationship between cost and range is found.

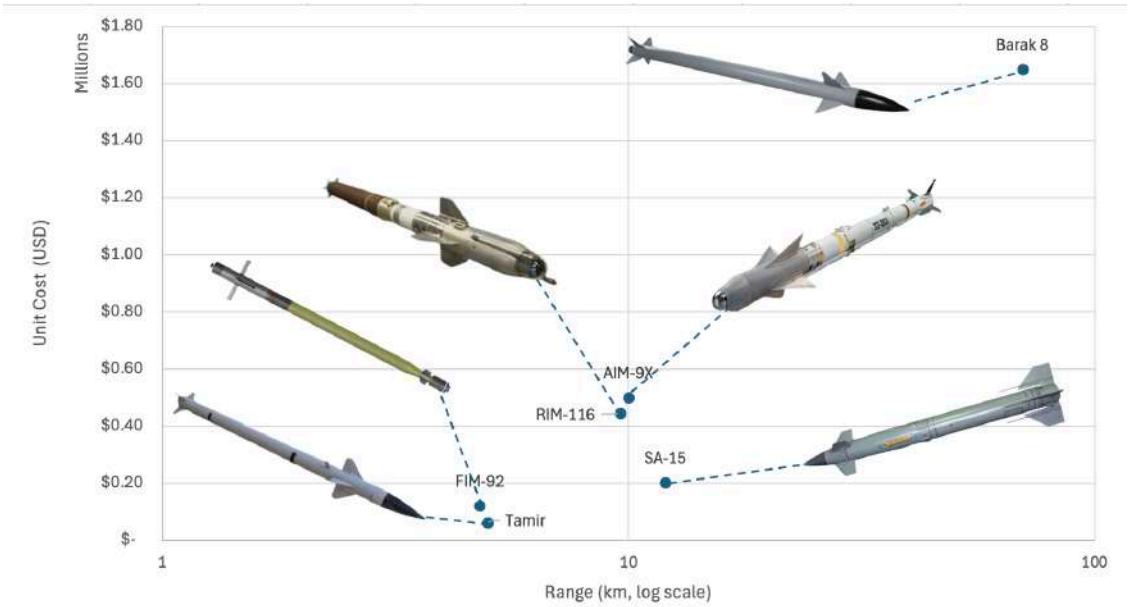

Fig. 7.0.1 Cost Plotted Against Range. [7]

8. Candidate Configuration Matrix Establishment

This section displays the missile configurations considered by the authors. Configurations with thrust vector control, reaction jets, as well as hard-launched configurations were immediately eliminated due to significantly high costs and lack of common or commercially available parts.

Fig. 8.0.1 Fins Only Configuration

Fig. 8.0.2 Canard and Fins Configuration

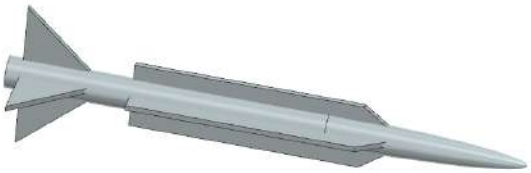

Fig. 8.0.3 Strakes and Fins Configuration

Fig. 8.0.4 Canard Only Configuration

Fig. 8.0.5 Strakes Only Configuration

9. Application of Optimization Function and Requirements Flow Charts to Configurations and Down-selections

The purpose of this section is to select three configurations that are most compatible with the objective function. The tables below display the scoring for each variable in the objective function for all fifteen

missile configurations. This will be used to determine which configuration will be best for the missile design selection.

Table 9.0.1 Objective Function Scoring for Configurations 1-4

	Fins	Canard and Fins	Strakes and Fins	Canard	Strakes
R_1: Cost < \$10k per missile	1	1	0	1	0
R_2: Horizontal Defense Radius of 5 mi (8 km)	1	1	1	1	1
R_3: 360° Azimuthal Coverage	1	1	1	1	1
R_4: Launch within < 1 second	1	1	1	1	1
R_5: Fixed, Ground-Based Launcher Installation	1	1	1	1	1
R_6: Maximum Engagement Altitude of 30,000 ft	1	1	1	1	1
R_7: System Initial Operational Capacity in December 2030	1	1	1	1	1
Weighted Sum (out of 7)	1	1	0.86	1	0.86
O_1: Mobile, Ground-Based Launchers	1	1	0	1	0
O_2: Ship-Based Launchers	0	1	0	1	0
O_3: Compatibility with Existing Launch Systems	1	1	1	1	1
O_4: Able to Intercept Target at Maximum Altitude and Minimum Range	1	1	1	0	1
Weighted Sum (out of 5)	0.75	1	0.50	0.63	0.50
AO_1: Aesthetically Pleasing	1	1	1	1	0
AO_2: Portable Design	1	1	1	1	1
AO_3: Established Components Used to Reduce Cost	1	1	0	1	1
AO_4: Minimal Maintenance	0	0	0	0	0

	Fins	Canard and Fins	Strakes and Fins	Canard	Strakes
AO_5: Data Links or In-Flight Updates	1	1	1	1	1
AO_6: One interceptor needed per threat	1	1	1	1	1
Weighted Sum (out of 6)	0.83	0.83	0.67	0.83	0.67

With this comparison, it is clear that the canards only design will be most suitable.

10. Weight Sizing

The weight sizing, based on information collected from STAMPED analysis, seeks to determine the approximate take-off weight, empty weight, and fuel weight. This is performed by using methods listed in Dr. Roskam's Airpane Design Part 1 [57]. However, the methods were slightly modified via STAMPED analysis to be applicable to missile weight sizing. A notable assumption of these estimations is the conservative observation of the lift-to-drag ratio to be negligible. Due to the configuration of the missile being so simple, this is a valid assumption.

An initial design weight estimate can be determined from the data collected in Appendix B. The summarized results are shown in Table 10.0.1 below.

Table 10.0.1 Initial Class I Weight Sizing Estimates

W_{to} (lbs)	W_e (lbs)	$\frac{W_e}{W_{to}}$ (-)	W_{oe} (lbs)
200	0.45	90	110

The first step taken to create weight sizing estimates was to define an initial estimate for takeoff weight. This was done by considering the takeoff weights of similar missiles (Tamir, SeaRAM, AIM-9X) from the STAMPED analysis. The missiles have takeoff weights between 90 lbs and 683 lbs. To stay within the mission specification of low-cost, lightweight construction, a reasonable estimate of 200 lbs was made for the takeoff weight.

To create an empty weight estimation, an assumption was made that the empty weight fraction would be between 0.3-0.6, based on information gathered in Appendix B. Thus, for the lightweight missile system, a realistic assumption of the empty weight fraction is 0.45. The empty weight of the missile could then be determined by reverse solving the fraction, as performed below.

$$\left(\frac{W_e}{W_{TO}}\right) = 0.45 \tag{1}$$

$$W_e = \left(\frac{W_e}{W_{to}}\right) \cdot W_{to} \tag{2}$$

$$W_e = 0.45 \times 200 \tag{3}$$

$$W_e = 90 \text{ lbs} \tag{4}$$

Finally, estimating the fuel weight of the missile was done under the assumption that the missile will be fully expended upon impact, meaning all the fuel will be burned in flight. This allows an estimation to be gathered from the following expression.

To meet the mission specifications and ensure the missile will reach 30,000 feet, the Aerotech 29mm G sized motor was selected [58]. The total weight of this rocket motor is 0.28 lbs. This will be incorporated into the fuel weight calculations.

$$W_f = W_{TO} - W_e \tag{5}$$

Substituting the known values, the estimate is presented as follows.

$$W_f = 200 - 90 \tag{6}$$

$$W_f = 110\ W_{motor}\ \text{(lbs)} \tag{7}$$

$$W_f = 110\ 0.28 \tag{8}$$

$$W_f = 110\text{lbs} \tag{9}$$

These estimates were verified and assumptions validated by checking numerical consistency with similar missile configurations. The total weight estimate of 200 lbs falls within the reasonable range of short-range interceptor missiles with the same canard configuration, such as the AIM-9X. The same can be said for the fuel fraction shown below.

$$\left(\frac{W_f}{W_{to}}\right) = \left(\frac{110}{200}\right) \tag{10}$$

$$\left(\frac{W_f}{W_{to}}\right) = 0.55 \tag{11}$$

11. Powerplant Sizing

To size the rocket motor, the open source amateur rocket simulation software OpenRocket [8] was used. It allowed for rapid simulation of many configurations with other design decisions made, thus quickly determining what rocket(s) would be needed. The first configurations tested were exclusively single-stage, with N or O size rockets. None were capable of reaching 30,000 feet, let alone with enough speed to maneuver. Additionally, many of the more powerful O rockets became too large or expensive to fit within the mission specifications. Thus, a two stage solution was explored. The authors determined that an AeroTech M1419W for the first stage and a larger Cesaroni N5800 for the primary booster worked very well, reaching 30,000 feet in altitude at Mach 2 which is plentiful for maneuvering in the terminal phase. 11.0.1 displays the flight

profile of the missile straight up, with no lift to assist in increasing range. At a total cost of approximately $2,200 in motors, this fits well within the cost profile necessary for the mission.

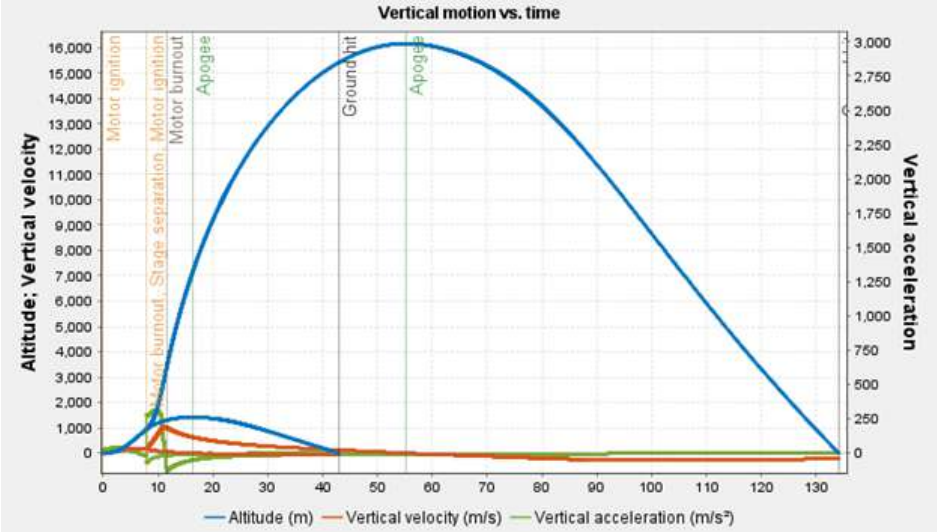

Fig. 11.0.1 Two-Stage Flight Simulation Generated by OpenRocket [8].

12. Seeker Selection and Design

To select a seeker that functions to track the threat with enough fidelity to track a small 4 inch diameter target in a nose or tail chase scenario, the authors explored many possible solutions. The two primary wavelengths of light the authors considered are IR and radar. Wien's law was used to determine a wavelength to sense based on the threat's temperature. Wien's law is as follows:

$$\lambda_{max} = \frac{2898\mu K}{T_{threat}} \tag{12}$$

Where λ_{max} is the wavelength at which spectral radiance peaks, and T_{threat} is the temperature of the threat missile. From this, and assuming that the temperature of the threat would be approximately 830 Kelvin due to the primary threat being artillery rockets traveling at a minimum of Mach 2, the maximum wavelength was determined to be 5.22 micrometers. This is in the range of mid-wave IR. From spectral radiance curves generated with Wien's law, it was also found that the threat would not emit a significant enough amount of ultraviolet light to be able to sense with a low-cost seeker. Additionally, if in a tail-chase scenario, the exhaust of the threat missile would be even higher, bringing the minimum wavelength needed to sense down further.

To find the required aperture diameter to obtain the proper resolution is found using the following equation:

$$R = \frac{1.22SR\lambda}{d} \tag{13}$$

Where R is the resolution needed, SR is the slant range, λ is the maximum wavelength as found previously,

and d is the aperture diameter. From this equation, it is clear that resolution and aperture size are inversely related. For this equation, it is assumed the resolution needs to be 4 inches, since that is the diameter of the smallest threat outlined in the RFP. The slant range is found using Pythagorean theorem, knowing the other two sides of the right triangle (altitude and range outlined in the RFP) are 30,000 feet and 5 miles. This led to a slant range of 39,962 feet (12,180 meters). This is a "worst-case," very conservative assumption since most likely the seeker will not need to enter terminal guidance at this range. Using this slant range, an aperture diameter of approximately 44 inches was required. This is clearly too large for this design. As such, the next variable that was manipulated was the slant range, assuming that the aperture diameter could not exceed 4 inches. Again, equation 13 was used, resulting in a slant range of approximately 5000 feet (1524 meters). A secondary method of increasing aperture diameter is with the use of a synthetic aperture. Single-pixel analog IR sensors can be placed on the tips of the canards, effectively acting as a much larger aperture. Using equation 13, with a canard span of 0.229 meters (9 inches), 5 micrometer IR sensors, and tracking a 4 inch diameter threat, it can resolve a target at 3.8 kilometers, providing a long time to view the target.

Clouds, fog, and dust are concerns as they obstruct the view of the seeker. From Teledyne FLIR, there is an atmospheric window for 3-5 micrometer infrared light in clear conditions [9]. In category I fog, mid-wave IR actually can be sensed from a greater distance than visible light. However, in thicker fog from category II through IIIc mid-wave IR performs marginally worse than visible light. Figure 12.0.1 shows the atmospheric transmissivity of infrared light.

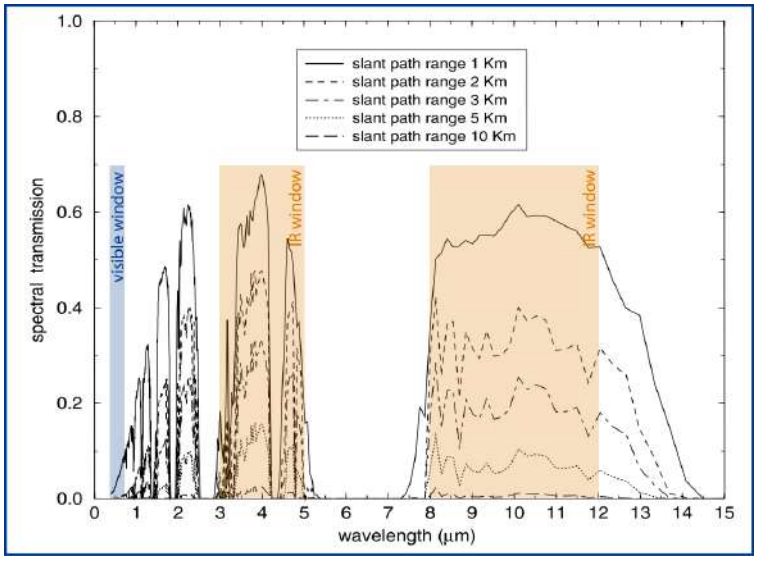

Fig. 12.0.1 Atmospheric Transmissivity of Infrared Light [9]

Radar guidance was also considered in both active and semi-active forms. Significant issues with deter-

mining a threat's precise position through a radar beam were raised, as well as the possibility of "notching", where a threat passing perpendicular to a radar is effectively invisible. An additional issue is that the use of an external synthetic aperture radar system is required to function. Additional issues include clouds, fog, and dust interfering with tracking radar beams, and poor resolution as shown with equation 13. Figure 12.0.2 shows a diagram of a threat missile, denoted with dashed arrows, entering a ground radar's detection area (the area enclosed by the round black line). The red lines denote radar returns that have been Doppler shifted by the vertical velocity of the threat, V_r. The upper dashed line is a missile "notching" the radar by flying perpendicular to it, thus generating no observable Doppler shift.

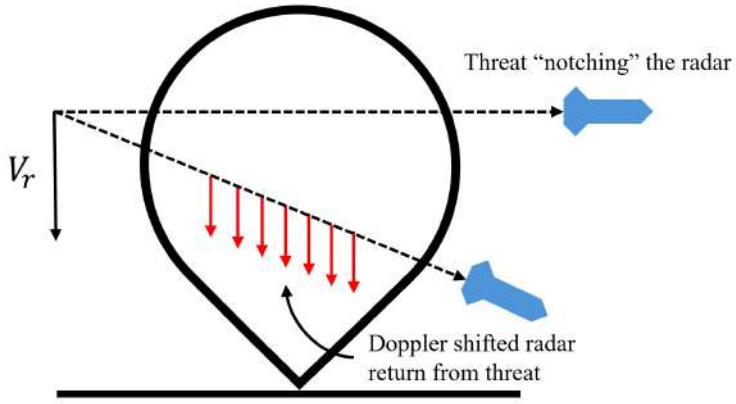

Fig. 12.0.2 Diagram of a Threat Entering a Radar Detection Area

Therefore, the seeker was designed to incorporate several single-pixel IR sensors on the tips of the canards and on the nosecone. An analog sensor from Boston electronics was found to suit these needs, and they also provide very low rise times of 15 nanoseconds[59]. It provides the highest response at 5 micrometers while being sensitive to 2-5.5 micrometer wavelengths. To maximize the effectiveness of the synthetic aperture and allow the missile to periodically look down for targets, the missile shall roll at 10 Hz. Additionally, adding custom lenses to narrow the field of view allows for more granular targeting. Figure 12.0.3 displays the layout of forward-looking sensors. An additional suite of four down-looking sensors are incorporated for the overflight mission profile to detect low-flying threats, making use of the rolling airframe. It should also be noted that it would be trivial to add additional sensors for improved resolution, and the number of sensors was made to be minimal to lower the cost as much as possible while still feasibly functioning.

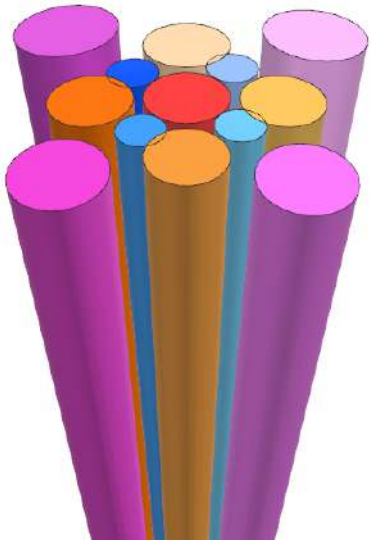

Fig. 12.0.3 Arrangement of Forward-Looking Sensors

Positional data is found by tracking which sensor detects the threat, and due to the very high response rate and sensitivity of the sensors, can be sampled quickly enough to determine when the threat is on the boundary of a cone of vision. Additionally, the threat's velocity can be found when comparing the expected versus actual time in a single vision cone as the Adder rolls. This provides even further position fidelity. Range data must be found from a ground command intercept link periodically communicating it to the missile, which can then extrapolate the data with an onboard computer to calculate approximate range. At a roll rate of 10 Hz and a maximum closing velocity between the Adder and the threat would be Mach 6. With the above sensor arrangement, this means there is a maximum positional update rate of once every 34 meters.

13. Warhead Design

The warhead must be designed to work with the mission profiles specified above. As such, it must be able to destroy a four-inch or larger diameter threat missile in a nose-on or tail-chase scenario. Therefore, it has been designed to project fragments forward in a conical distribution. Additionally, 4 of the 6 kilograms of payload budget was allocated for the warhead. From this point, the number of fragments needed and the maximum effective range to achieve a probability of kill (P_K) of 90% must be found. This was done following the methods of Chapter 8 of Weaponeering by Dr. Morris Dreils [60]. To find the number of fragments needed, the following equation is used:

$$P_K = 1 - e^{\frac{A_E * - N}{A_S}} \tag{14}$$

Where P_K is the probability of kill, A_E is the vulnerable area of the threat missile, N is the number of fragments needed, and A_S is the fragmentation area. From this point, the angle of distribution of fragmentation must be determined. The half-cone angle was set to be the edge of the four small central sensors. This was to ensure that the fragmentation would cover the whole area covered by these sensors. Minimizing the half-angle to 6 degrees allowed for a balance between miss distance and number of fragments. First, solving for the vulnerable area of the threat missile (also called effective area):

$$A_E = \pi * r^2 \tag{15}$$

Figure 13.0.1 displays the minimum vulnerable area of the threat missile.

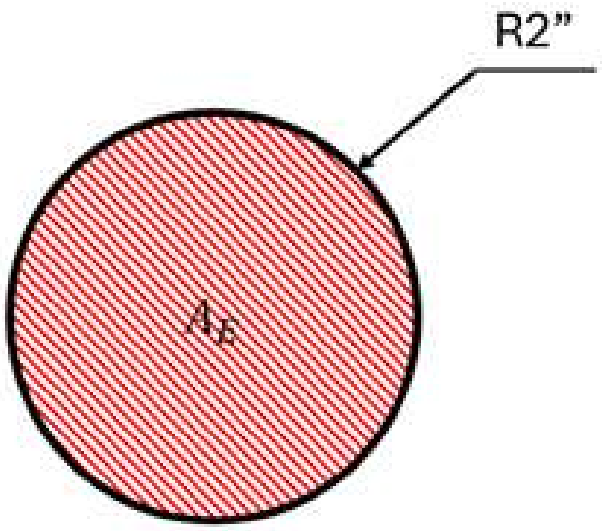

Fig. 13.0.1 Diagram of vulnerable area of threat missile.

To solve for the fragmentation area, the miss distance must be determined. Through plotting the relationship of the number of fragments and miss distance, the team found that a 6 degree half-angle spread required 1800 fragments to achieve a maximum miss distance of 44 feet and 6 inches (13.6 meters). This distance was selected from the update rate of the seeker being 34 meters, it would not have to interpolate more than twice for ranging data. As rapid accelerations or decelerations are not expected within this time from any of the possible threats, this was deemed acceptable. The following equation is used to find A_S:

$$A_S = \Omega * r^2 \tag{16}$$

Figure 13.0.2 demonstrates the physical representation of fragmentation area:

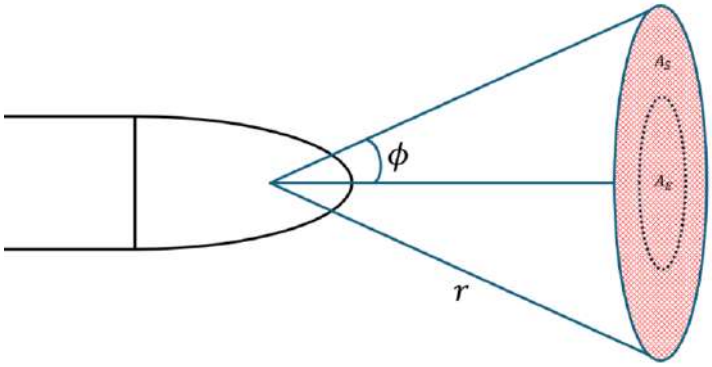

Fig. 13.0.2 Fragmentation area compared to vulnerable area.

Where Ω is found as follows using the half angle of the cone's spread, ϕ:

$$\Omega = 2\pi 1 - cos\phi \tag{17}$$

Solving for the number of fragments needed requires rearranging equation 14 and setting the values previously found or set. Solving for the number of fragments:

$$N = -\frac{A_S}{A_E} \ln 1 - P_K \tag{18}$$

The total mass of the metal fragments was found from the mass of the individual fragments to be used multiplied by the number of fragments. 5 grain steel shot was selected for the fragmentation for its balance between size, mass, and cost. Once the total mass of fragmentation was defined to be 0.58 kg, the rest of the warhead was divided between the explosives and the casing. Through trial and error, a balance between the mass of the explosives and the casing was conducted to achieve a minimum impact on the target of 1 kJ, an impact deemed sufficient to disable the target. This design required 1.4 kg of the warhead to be allocated to the casing to control the detonation and direct the fragmentation out the front of the Adder. The remaining 2 kg of the warhead is for the explosives. Using the mass ratio of explosives (m_c) and fragments (m_m), the initial fragment velocity can be found:

$$V_0 = \sqrt{2E} * \sqrt{\frac{m_c}{m_c \ \frac{1}{2} m_m}} \tag{19}$$

Where $\sqrt{2E}$ is the Gurney explosive constant, 2,800 for RDX.

Finally, the kinetic energy on impact is found from the velocity (V_0) and individual mass of a fragment

(m_0) as follows:

$$KE = \frac{1}{2} m_0 V_0^2 \tag{20}$$

Due to the involved nature of the calculations required, a MATLAB program was constructed to automate this process. The result is that for a 4 kilogram warhead distributing 1800 fragments in a 6 degree half-angle cone, a specified P_K of 90%, a fragment mass of 5 grains, and a maximum miss distance of 44 feet and 6 inches (13.6 meters), the minimum impact energy of an individual fragment is 1.11 kJ.

14. GCI and GNC Design

To determine the appropriate antenna for a ground control link, Ansys HFSS was used. The authors found that X-band guidance radars such as the AN/MPQ-64 Sentinel and the AN/SPY-3 are relatively common and have the capability for GCI guidance. Therefore, an X-band patch antenna was integrated into the first stage fins. A design for a high-bandwidth X-band patch antenna was sourced and modeled within Ansys HFSS within the fin to find the Friis transmission link budget[61]. Figure 14.0.1 shows the patch antenna modeled within HFSS.

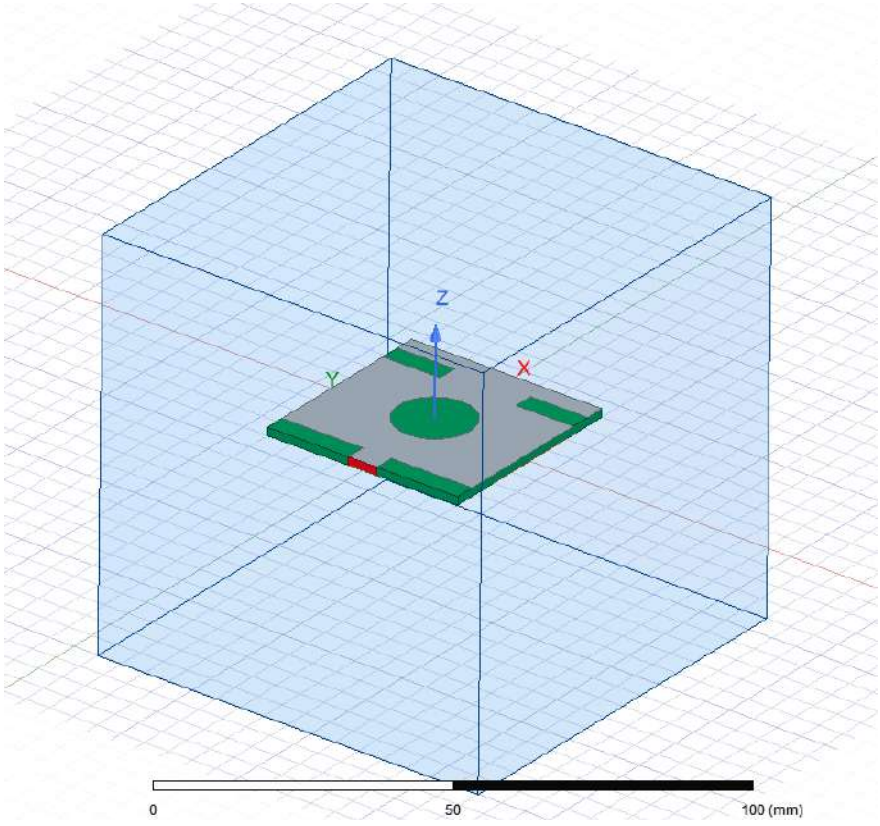

Fig. 14.0.1 HFSS Antenna Model

An analysis of the antenna's reflected power across the X-band was analyzed to determine the worst-case scenario. Figure 14.0.2 displays this graph, and it was found that a maximum reflected power at roughly 9 GHz was the worst-case scenario.

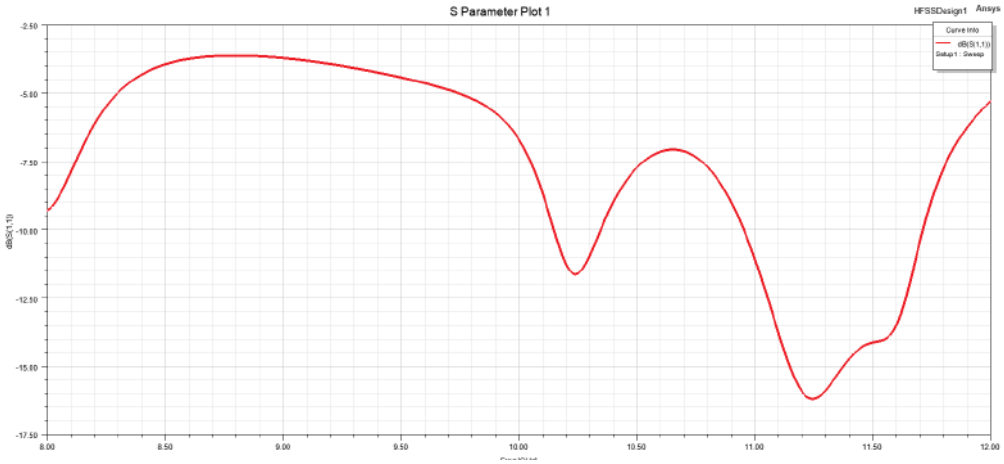

Fig. 14.0.2 Reflected Power Across X-Band

From the worst-case scenario, the gain as a function of incidence angle was also analyzed within HFSS at 9 GHz. Figure 14.0.3 contains the result of this analysis, where it was found that the maximum gain was approximately 1.32 dB while the minimum was -9.18 dB.

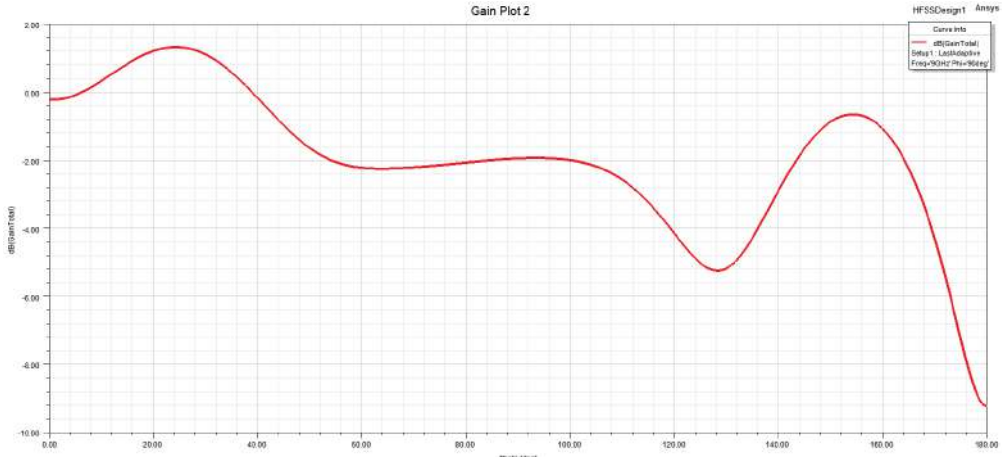

Fig. 14.0.3 Antenna Gain Plot at 9 GHz

With the receiver gain and bandwidth from the HFSS simulation, the Friis link budget can be calculated. The Friis transmission equation is:

$$P_r = P_t G_t G_r \left(\frac{\lambda}{4\pi d}\right)^2 * PLF \tag{21}$$

Where:

- P_r is the received power,
- $P_t = 10$ W is the transmitted power,
- G_t and G_r are the transmitting and receiving antenna gains,
- λ is the wavelength at $f = 9$ GHz,
- $d = 10{,}170$ m is the missile-to-ground station distance, accounting for seeker takeover.
- PLF is the polarization loss factor (0.5 for a linearly and circularly polarized case)

From the HFSS simulation:

- Transmit gain: $G_t = -9.2$ to 1.3 dB
- Receive gain: $G_r = 6$ dB

The resulting received power is:

$$P_r = -78 \text{ dBm (min)}, \quad -67.4 \text{ dBm (max)} \tag{22}$$

Assuming a receiver sensitivity of -100 dBm, the link margin becomes:

$$\text{Link Margin} = P_r - \text{RS} = 22 \text{ dB (min)}, \quad 32.6 \text{ dB (max)} \tag{23}$$

The signal-to-noise ratio (SNR) is calculated as:

$$\text{SNR (dB)} = P_r - P_N \tag{24}$$

Where the noise power is given by:

$$P_N = kT_0BF \tag{25}$$

Using:

- Bandwidth $B = 0.75$ GHz (from HFSS model),
- Noise figure $F = 3$ dB,
- Resulting in $P_N = -82.2$ dBm

The SNR values are then:

$$\text{SNR} = 4.2 \text{ dB (min)}, \quad 14.8 \text{ dB (max)} \tag{26}$$

The positive value for SNR shows that the signal is well above the noise floor and therefore is strong enough to be detected and separated from the noise power. Furthermore, the positive link margin suggests that the power received by the ground station is well above the sensitivity level and therefore meets the threshold for basic detection.

Four patch antennas have been integrated into the rocket-one on each second stage fin. This has been done to provide redundancy, as well as to prevent signal blanking from the rocket body while the missile rolls. Figure 14.0.4 displays this integration.

Fig. 14.0.4 Antenna Fin Integration

As all sensors and the antenna require relatively low processing power, the authors designed a flight computer from open-source and non-export restricted components. Additional benefits of this computer are that the owners have full software control, and flashing custom software by a nation importing the Adder is trivial. No operating system is technically necessary to interface with it, as it can merely load a lightweight program to execute. A triple-redundant gyro and accelerometer chip was also integrated on the computer to prevent faulty flight data. It is powered by a thermal battery to provide long shelf life, and is potted in epoxy to provide resistance to the high accelerations expected. Four servos with 20 Hz response rates and high torque were selected to actuate the canards.

15. Class 1 & 2 Stability Analysis

15.1. Class 1 Analysis

To determine the stability of the selected aircraft configuration, a longitudinal X-plot was created. This type of plot shows the aircraft center of gravity and aerodynamic center as a function of horizontal tail size (in the case of this missile, the largest, back-most set of fins were treated as a horizontal tail). When this plot is created, the size of the aerodynamic surfaces can be chosen such that the static margin can be designed based on a desired value. For this analysis, a +10% static margin is the goal. This value ensures inherent longitudinal stability of the aircraft. In order to create the plot, the center of gravity was determined using OpenRocket software, where a model of the proposed missile design was created. This allows the size of the aerodynamic surfaces to be changed and the effect on the aircraft center of gravity to be tracked accordingly. With the center of gravity determined, the aerodynamic center of the aircraft must be calculated. The aerodynamic center was calculated following techniques from part 6 of Roskam's aircraft design text. Since Roskam lays out the techniques for aircraft, the front most set of fins were treated as canards, the middle as the wings, and the back as the horizontal tail for this analysis. First, $C_L\alpha$ was determined for all three

flight surfaces using the following:

$$C_L\alpha = \frac{\pi A}{1\sqrt{\frac{A^2\pi^2}{C_{L\alpha}^2@M}\left(1\frac{\tan^2\Lambda_{c2}}{\beta^2}\right)}1} \tag{27}$$

Where A is the aspect ratio, Λ_{c2} is the semi-chord sweep angle, β is equal to $\sqrt{1-M^2}$, and $C_{L\alpha}^2@M$ is determined from Abbott and Von Doenhoff's Theory of Wing Sections.

To prove subsonic stability, Mach 0.2 was used. This calculation was performed for the canard, wings, and horizontal tail. Next, the contribution of the fuselage body lift was accounted for in $C_L\alpha_w$ using the equation:

$$C_L\alpha_{wf} = \left(1\,0.025\frac{d_f}{b} - 0.25\left(\frac{d_f}{b}\right)^2\right) * C_L\alpha_w \tag{28}$$

Where d_f is the fuselage diameter and b is the wingspan of the wings.

Next, the position of the aerodynamic center of each aerodynamic surface was determined. This was done using a scaled drawing of the proposed missile design to obtain values $\bar{X}_{AC,c}$, $\bar{X}_{AC,w}$, and $\bar{X}_{AC,h}$.

Next, the downwash coefficient was determined for both the effect of the downwash from the wing onto the horizontal tail, as well as the upwash from the wing onto the canard. The following equation was used:

$$\frac{\delta\varepsilon}{\delta\alpha} = 4.44\left(\frac{C_{L\alpha}^2@M}{C_{L\alpha}^2@M=0}\left(K_A K_\lambda K_h\sqrt{cos\Lambda_{c4}}\right)^{1.19}\right) \tag{29}$$

Where:

$$K_A = \frac{1}{A} - \frac{1}{1\,A^{1.7}} \tag{30}$$

and

$$K_\lambda = \frac{10-3\lambda}{7} \tag{31}$$

and

$$K_h = \frac{1-\frac{h_h}{b}}{\left(\frac{2l_h}{b}\right)^{13}} \tag{32}$$

Where λ is the taper ratio and h_h and l_h are determined from scale drawings of the aircraft.

Next, the location aerodynamic center of the wing-fuselage combination must be calculated accounting for Munk shift. In order to properly account for Munk shift, Multhopp integration was performed as outlined in Roskam part 6. The result of the Multhopp integration was a munk shift of -1.71. The aerodynamic center of the wing-fuselage combination is then calculated as:

$$\bar{X}_{AC,wf} = \bar{X}_{AC,w}\;\Delta\bar{X}_{AC,f} \tag{33}$$

Where $\bar{X}_{AC,w}$ is 0.25 (the aerodynamic center of the wing only) and $\Delta\bar{X}_{AC,f}$ is the munk shift, resulting in $\bar{X}_{AC,wf}$= -1.46.

Finally, all variables required to calculate the aerodynamic center of the aircraft as a whole are obtained.

The aerodynamic center is calculated using the following:

$$\bar{X}_{AC,A} = \frac{\bar{X}_{AC,wf} C_L\alpha_{wf}\, C_L\alpha_h \left(1 - \frac{\delta\varepsilon_h}{\delta\alpha}\right) \frac{S_h}{S} \bar{X}_{AC,h} - C_L\alpha_c \left(1\ \frac{\delta\varepsilon_c}{\delta\alpha}\right) \frac{S_c}{S} \bar{X}_{AC,c}}{C_L\alpha_{wf}\, C_L\alpha_h \left(1 - \frac{\delta\varepsilon_h}{\delta\alpha}\right) \frac{S_h}{S}\, C_L\alpha_c \left(1\ \frac{\delta\varepsilon_c}{\delta\alpha}\right) \frac{S_c}{S}} \tag{34}$$

The resulting aerodynamic center of the aircraft for the proposed design is:

$$\bar{X}_{AC,A} = -1.6703 \tag{35}$$

The negative value means that the aerodynamic center is forward of the leading edge of the wing at the mean geometric chord. This value of $\bar{X}_{AC,A}$ places the aerodynamic center of the entire aircraft aft of the center of gravity, indicating stability. However, the static margin still must be calculated. The static margin can be determined using:

$$SM = \bar{X}_{AC,A} - \bar{X}_{CG} * 100\% \tag{36}$$

In this case, this results in a static margin of approximately 24%, which is a bit higher than necessary. As such, a longitudinal X-plot was developed for different sizes of the horizontal tail to determine what tail size would result in a static margin closer to 10%. The plot developed is shown in Figure 15.1.1

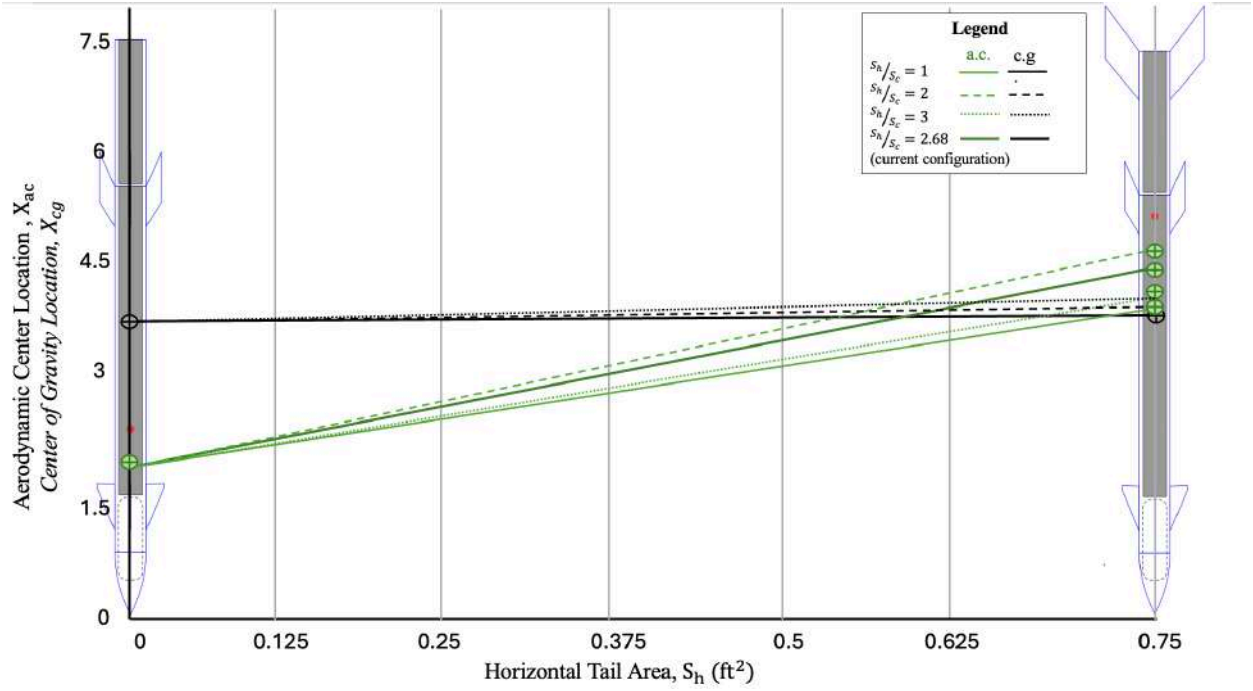

Fig. 15.1.1 Aerodynamic Center and Center of Gravity as a Function of Horizontal Tail Area

From the plot, it is clear that as the ratio between the area of the horizontal tail and the canards change, there is little effect on the center of gravity position. However, the aerodynamic center differs more. In all cases, the aerodynamic center is aft of the center of gravity, indicating longitudinal stability. To reach a more desirable static margin (closer to 10%), the horizontal tail should be sized down. When $\frac{S_h}{S_c}$ equals 1.15, the static margin is calculated as 10.6%. However, the effects on apogee, maximum flight speed, and other

flight characteristics will need to be investigated before proceeding with sizing down of the horizontal tail. Regardless, in all cases, longitudinal stability is achieved. Further analysis will include the same calculations being performed on the second stage, after the booster is dropped and the aircraft becomes a two-surface configuration, as well as investigating stability in the supersonic regime.

A directional X-Plot was then created to determine the area of the bottom two fins that will act as the vertical tail and affect the lateral stability of the missile system. This plots the vertical tail area against the yawing moment coefficient due to sideslip. The following equation is used to find $C_{n\beta}$:

$$C_{n\beta} = C_{n\beta_w f}\, C_L\alpha_V \frac{S_v}{S}\frac{X_v}{b} \tag{37}$$

Figure 15.1.2 shows how the horizontal distance from the center of gravity of the missile body to the center of gravity of the vertical tail was determined which gives the value of X_v:

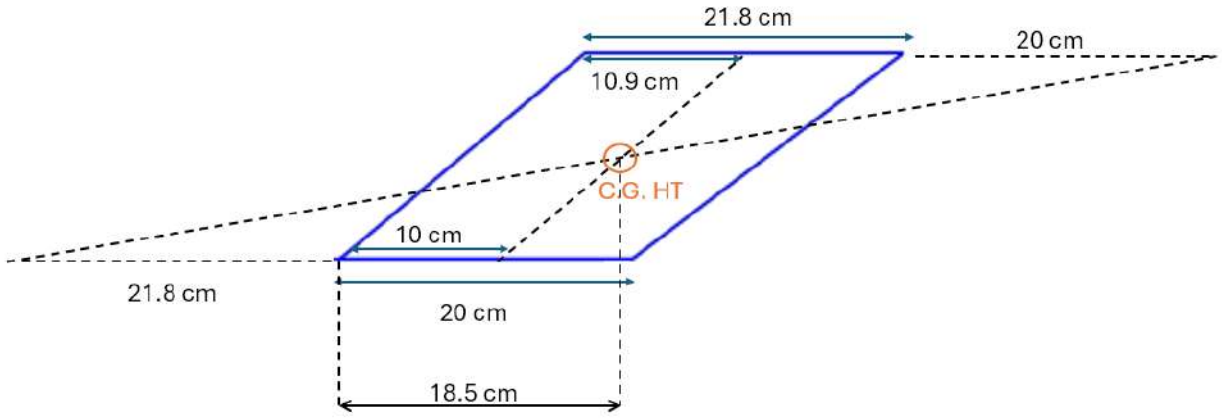

Fig. 15.1.2 C.G. of Vertical Tail Distance

The next aspect of the equation that needed to be determined was $C_L\alpha_V$, which was calculated using the equation below:

$$C_L\alpha_V = \frac{\pi A_V}{1\sqrt{\frac{A_v^2\pi^2}{C_{L\alpha}^2@M}\left(1\frac{\tan^2\Lambda_{c2}}{\beta^2}\right)}1} \tag{38}$$

The unknown variables in this equation were found using the following:

$$C_L\alpha_{@M=0.2} = \frac{C_{l\alpha}}{1-M^{212}} \tag{39}$$

$$\beta = \sqrt{1-M^2} \tag{40}$$

$$A_v = \frac{b_V^2}{S_v} \tag{41}$$

Using OpenRocket, the area of one vertical tail for the missile had already been determined, but to confirm the value a Directional X-Plot was created in MATLAB. Solving, $C_{n\beta} = 0.1876$ per degree and upon

plotting, the following figure gave that $S_v = 294.69cm^2$ as found through open rocket.

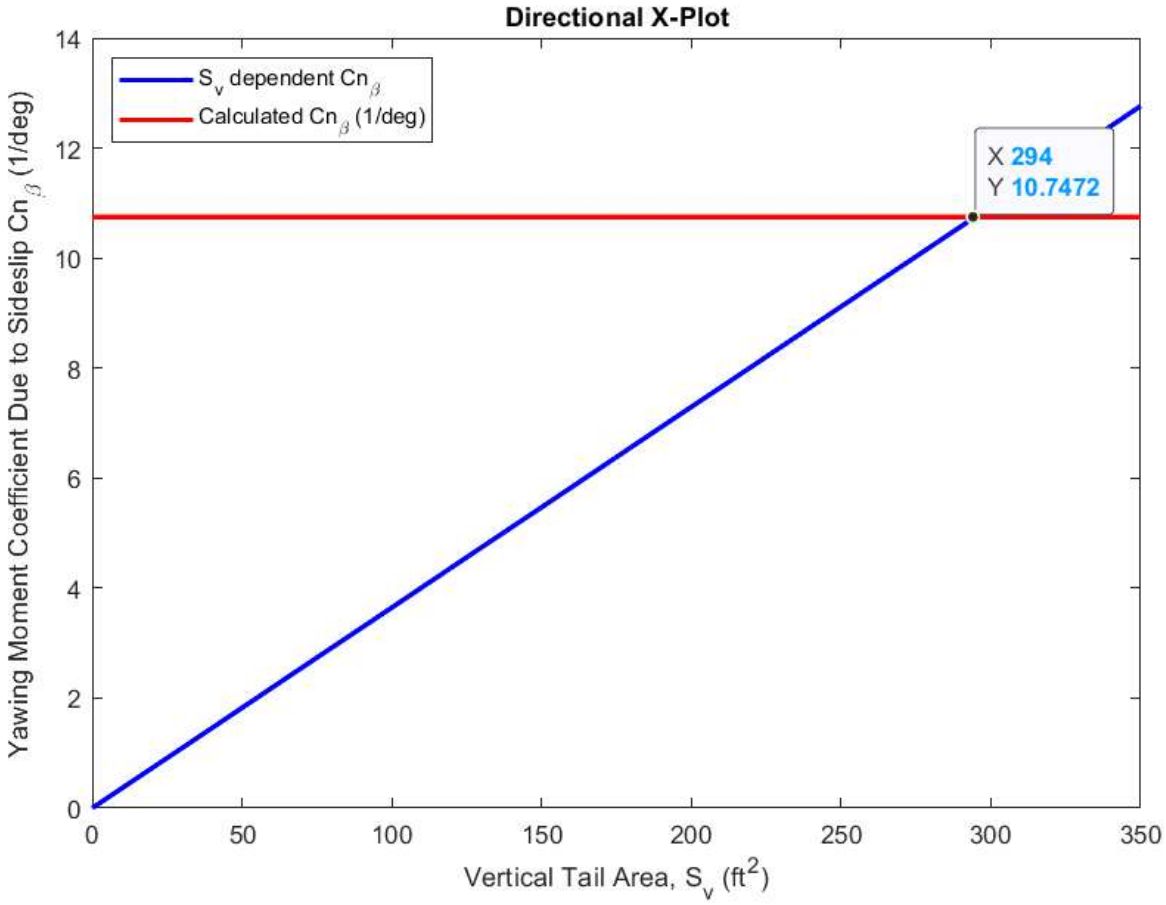

Fig. 15.1.3 Directional X-Plot

The stall speed V_s for +1g flight is given by:

$$V_s = \sqrt{\frac{2W_{oe}}{\rho S C_{L\max}}} \tag{42}$$

Substituting known values:

$$V_s = \sqrt{\frac{2.00 \times 109 \text{ lbf}}{1.50 \times 10^{-3} \frac{\text{lbf}}{\text{ft}^3} \times 0.24 \text{ ft}^2 \times 1.10}} \tag{43}$$

$$V_s = 748 \text{ ft/s} \tag{44}$$

The minimum control speed V_{mc} is estimated as:

$$V_{mc} = 1.2V_s = 1.2 \times 748 \text{ ft/s} = 897.6 \text{ ft/s} \tag{45}$$

15.2. Class 2 Analysis

The sized design was assessed using OpenRocket software and other performance techniques. It was found that the previous sizing no longer allowed the missile to reach the required altitude. As such, further refining and sizing of the canards and fins was performed. They middle set of fins was moved forward on the missile body and forward-swept trailing edges were added. After changing the sweep and location of the fins, the stability and control analysis was performed again in accordance with the design changes. The updated design is shown in Figure 15.2.1.

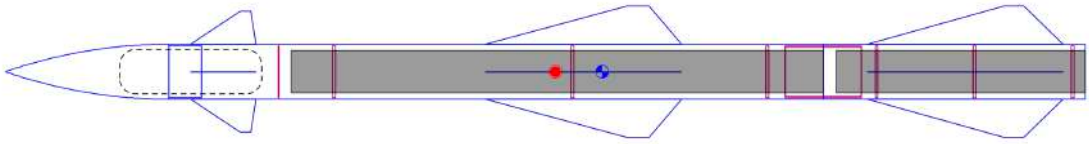

Fig. 15.2.1 Updated Missile Design

This time, the stability and control analysis was performed in two stages, once for the sustainer body only and once for the sustainer and stage configuration. The first stage analysis held the middle fin ("wing") size constant at 0.8333 ft^2 and sized the canards in order to obtain a static margin between -5 and 5%. Since fuel burn occurs rapidly, the aerodynamic center of the missile will shift aft within the first few seconds of flight, increasing the stability. The same process as shown in Appendix L was followed, with proper modifications made to exclude the back-most fins (referred to previously as the "horizontal tail") for the stage. The longitudinal X-plot generated for this configuration is shown in Figure 15.2.2

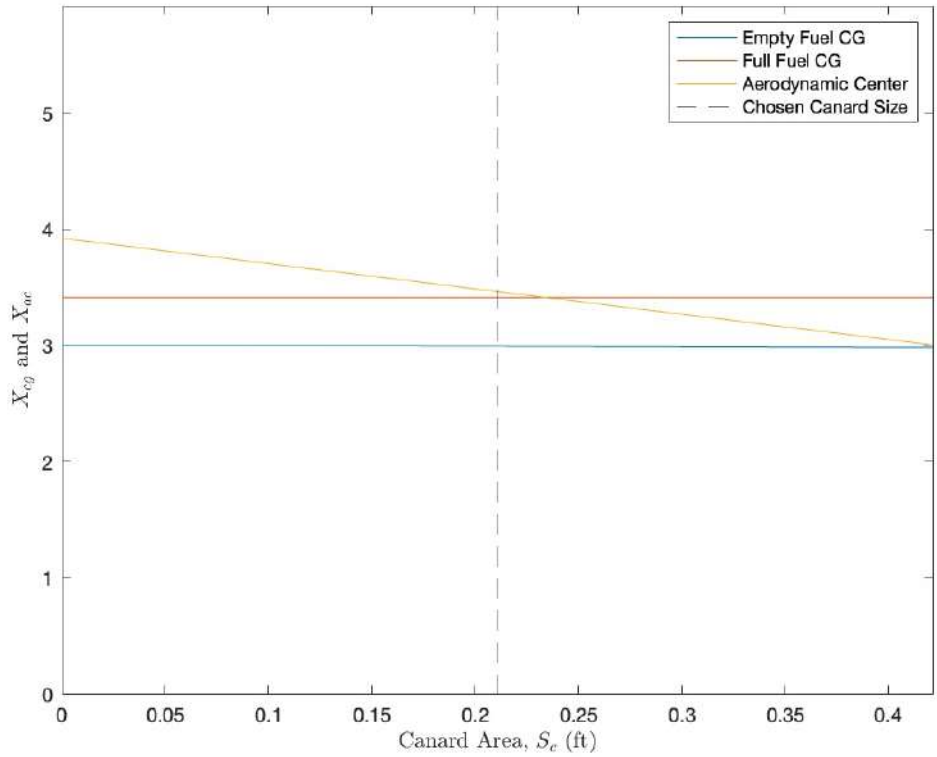

Fig. 15.2.2 Sustainer Only Longitudinal X-Plot

From this analysis, a canard size of 0.2108 ft^2 was decided upon. This results in a static margin of approximately -1.7%. This was deemed acceptable, as fuel burn will create stability nearly instantly.

Once the sustainer was stable, stability analysis was performed again for the sustainer and stage configuration. This time, the canard and wing size were both held constant, and the back-most fins were sized. Again, a static margin between -5 and 5% was desired. The resulting longitudinal X-plot for this configuration is shown in Figure 15.2.3.

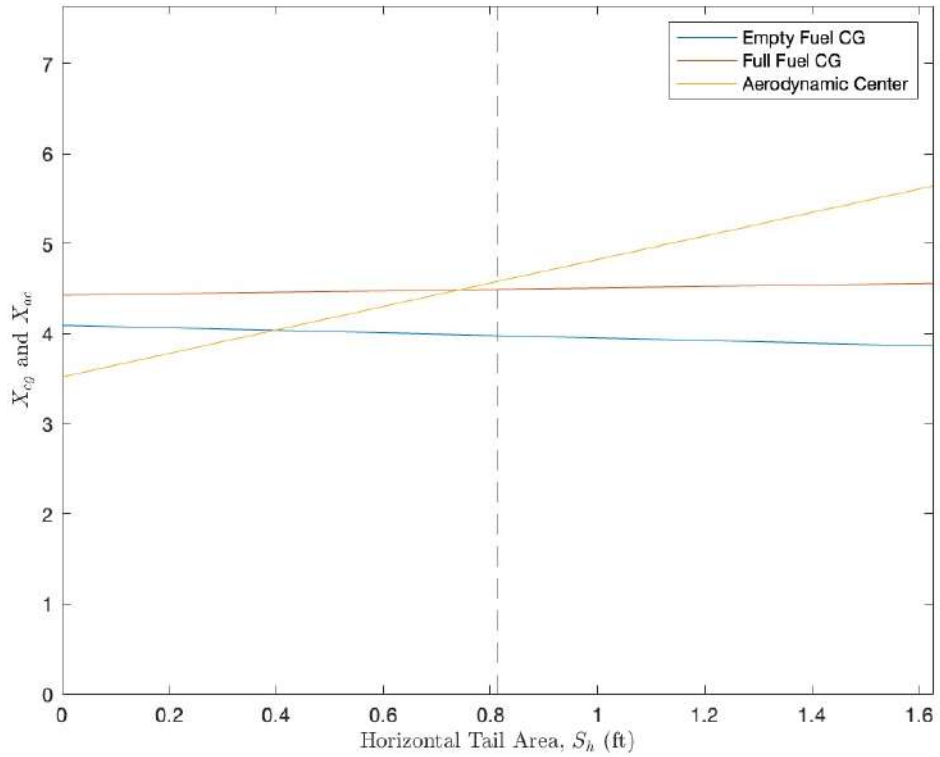

Fig. 15.2.3 Sustainer and Stage Longitudinal X-Plot

A fin area of 0.8132 ft^2 was decided upon for this configuration, resulting in a static margin of approximately -2.2%. Again, fuel burn initiates stability.

16. Class 2 Performance Analysis

To calculate the class 2 performance, the drag was found using Fleeman's drag buildup method [62]. It comprises of finding the friction, wave, and zero-velocity drag of the body and each surface. First, to find the total coefficient of drag of the body, the friction drag is calculated as follows:

$$C_{D_0 body,friction} = 0.053 \frac{l}{d} \frac{M}{ql}^{0.2} \tag{46}$$

Where l is the total missile length, d is the missile diameter, M is the Mach number, and q is the dynamic pressure. Then, to find the base drag:

$$C_{D_0 base} = \frac{0.25}{M} \tag{47}$$

Finally, to find the body wave drag:

$$C_{D_0 body,wave} = 1.59 \frac{1.83}{M^2} tan^{-1} \frac{0.5}{\frac{l_{nose}}{d}}^{1.69} \tag{48}$$

Where $\frac{l_{nose}}{d}$ is the nose fineness ratio. Summing these three components gives the body wave drag. The next step is to find the drag on each set of lifting surfaces. This comprises of the wave and friction drag for each. To find the wave drag, the following equation is used:

$$C_{D_0 surface_{wave}} = n_{surface}\left[\frac{2}{\gamma M_{\Lambda_{LE}}^2}\right]\{\{\frac{\gamma\, 1 M_{\Lambda_{LE}}^2}{2}\}\{\frac{\gamma\, 1}{2\gamma M_{\Lambda_{LE}}^2 - \gamma - 1}\}^{\frac{1}{\gamma-1}} - 1\} * \frac{sin^2\delta_{LE} cos\Lambda_{LE} t_{MAC} b}{S_{ref}} \tag{49}$$

Where $n_{surface}$ is the number of pairs of surfaces (two for all sets in this missile), the ratio of specific heats is assumed to be 1.4, and the equivalent Mach number accounting for leading edge sweep is found with the following equation:

$$M_{\Lambda_{LE}} = M cos\Lambda_{LE} \tag{50}$$

Then, to find the friction drag on the surface:

$$C_{D_0 surface,friction} = n_{surface}\{0.0133\left[\frac{M}{qc_{MAC}}\right]^{0.2}\}\left(\frac{2S_{surface}}{S_{ref}}\right) \tag{51}$$

Where the mean aerodynamic chord is found as follows:

$$c_{MAC} = \frac{x_{AC}}{\{\frac{ARM^2 - 1 - 0.67}{2ARM^2 - 1^{12} - 1}\}} \tag{52}$$

Where *AR* is the aspect ratio of the surface. Once the surface friction and wave drag has been summed, the total drag of the missile can be found. When at sea level, the missile's total drag is found to be 470 lbf at the first stage burnout and 419 lbf at the second stage's maximum velocity of Mach 3. The second stage drag falls significantly to 138 lbf at 30,0000 feet altitude.

17. Structural Analysis

To analyze the structure of the Adder, a finite element model (FEM) was created in MSC Patran. The entire Adder configuration was modeled at full fuel as this case will experience the highest maneuvering loads. This model was made using the CAD model presented previously. It was simplified through mid-surfacing to convert all solid bodies into sheet bodies. These sheets were meshed using shell elements to capture all relevant degrees of freedom. In addition to shell elements, point masses were used to model the mass of individual components to ensure accurate results. This model is shown in Figure 18.0.2.

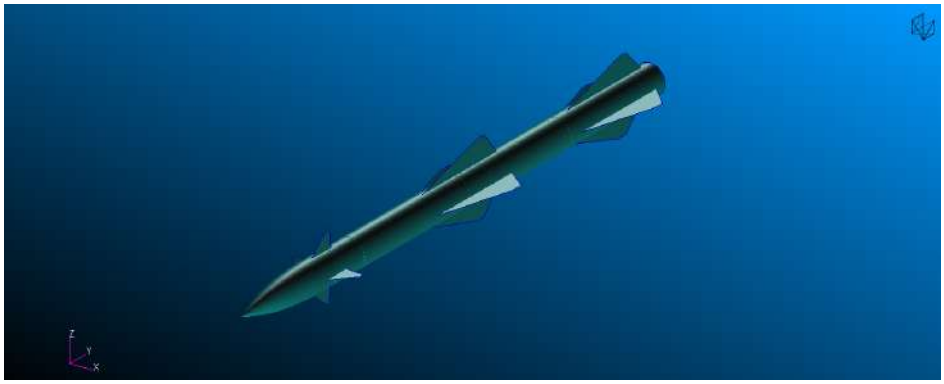

Fig. 17.0.1 Finite Element Model of Adder

Based on the Adder's intercept strategy and previous analyses, the following load cases were examined. A 40 G lateral maneuver, a 70 G forward acceleration, and aerodynamic loading at first stage burnout. From these load cases, it was determined that the lateral maneuver was the most critical load case, as it exhibits the highest stress values in the components with the lowest allowable stresses. From this load case, the following failure modes were considered: buckling, ultimate tensile failure, tensile yield failure, compressive yield failure, and ultimate shear failure. Margins of safety were computed for each of these failure loads and are shown in Table 17.0.1.

Table 17.0.1 Critical Margins of Safety for a 40 G Lateral Maneuver

Failure Mode	Critical Margin	Location of Failure
Ultimate Tensile Failure	0.457	Sustainer Fins
Tensile Yield Failure	0.0384	Sustainer Fins
Compressive Yield Failure	0.0384	Sustainer Fins
Ultimate Shear Failure	0.758	Sustainer Fins
Buckling Failure	0.569	Sustainer Fins

The fringe plots for the two most critical margins are shown below. The fringe plot for minimum principal stress is shown in Figure 17.0.2, while the fringe for maximum principal stress is shown in Figure 17.0.3.

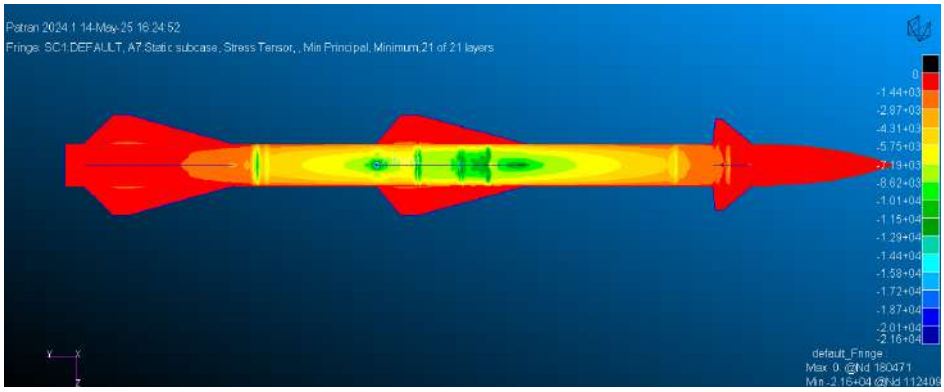

Fig. 17.0.2 Fringe Plot of Minimum Principal Stress

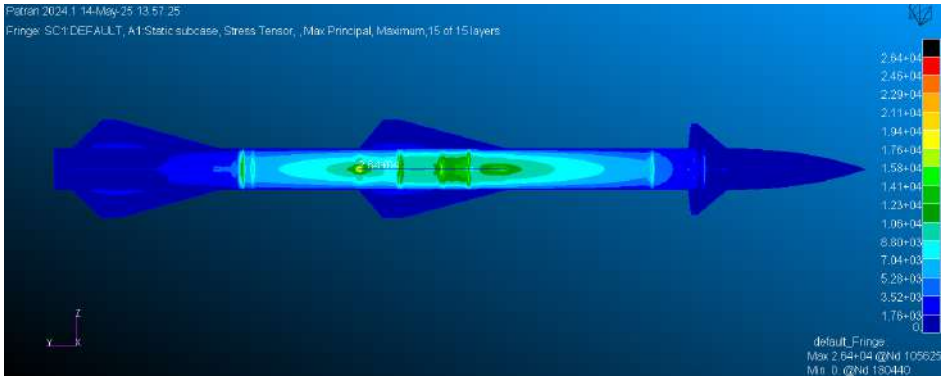

Fig. 17.0.3 Fringe Plot of Maximum Principal Stress

A summary of the final component thicknesses and materials determined from this model are shown below in Table 17.0.2.

Table 17.0.2 Component Materials and Thicknesses

Component	Material	Thickness
Control Surfaces	5005 Anodized Black Aluminum	0.0630 in
Main Body	Pultruded Graphite Composite	0.0832 in
Ring Frames	5005 Anodized Black Aluminum	0.250 in
Bulkheads	5005 Anodized Black Aluminum	0.150 in
Nose Cone	Graphite Composite	0.0832 in

18. 3-View, Advanced CAD, Situational Renderings, & Exploded Views

The updated 3-view of the Adder (sustainer and stage) is shown in Figures 18.0.1 and 18.0.2.

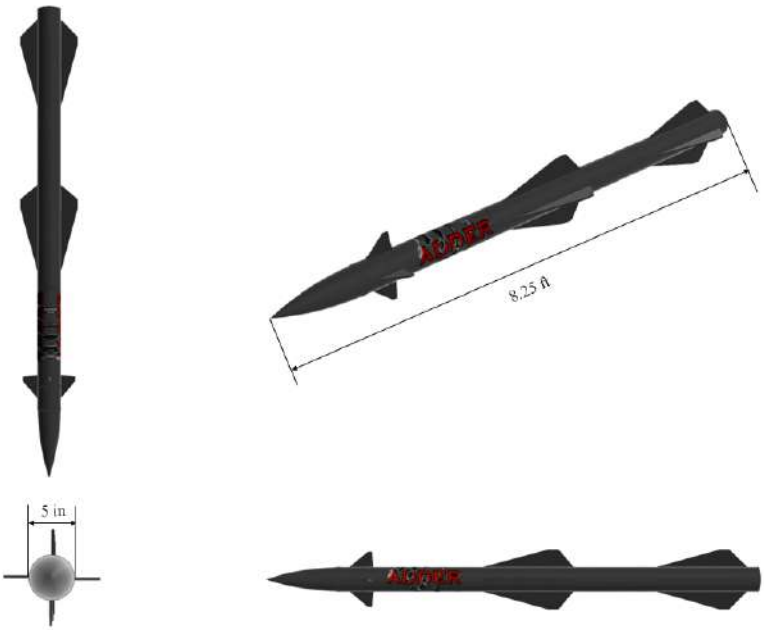

Fig. 18.0.1 Updated 3-View for Entire Adder Configuration

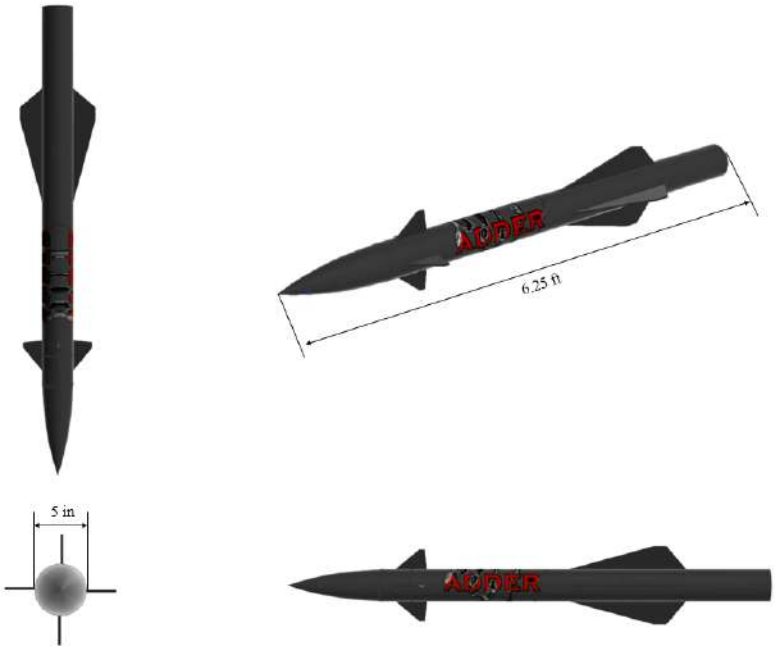

Fig. 18.0.2 Updated 3-View for Sustainer Only Adder Configuration

Table 18.0.1 outlines the salient characteristics of the design after all analyses had been performed.

Table 18.0.1 Salient Characteristics of the Updated Missile Design

Characteristic	Value
Overall Length (One Stage)	6.25 ft (1.91 m)
Overall Length (Both Stages)	8.25 ft (2.51 m)
Body Diameter	5.00 in (0.13 m)
Body Shape	Circular
Canards	
Number	4
Sweep Angle	50.37°
Root Chord	0.394 ft (0.120 m)
Tip Chord	0.066 ft (0.020 m)
Span	0.917 ft (0.280 m)
Aspect Ratio	3.985

Characteristic	Value
Wings	
Number	4
Sweep Angle	74.92°
Root Chord	1.499 ft (0.457 m)
Tip Chord	0.167 ft (0.051 m)
Span	1.00 ft (0.305 m)
Aspect Ratio	1.20
Horizontal Tail	
Number	4
Sweep Angle	74.92°
Root Chord	1.478 ft (0.450 m)
Tip Chord	0.148 ft (0.045 m)
Span	1.00 ft (0.305 m)
Aspect Ratio	1.20

The exploded view illustrating each of the components in the proposed design is shown in Figure 18.0.3. Figure 18.0.4 show more detailed views of the electronic system and all of its components. Note that in Figure 18.0.3, the actual sensors are too small to be visible, so the red stars indicate their position. While their locations are accurate (four sensors on the nose cone and two on each canard), they are not to scale.

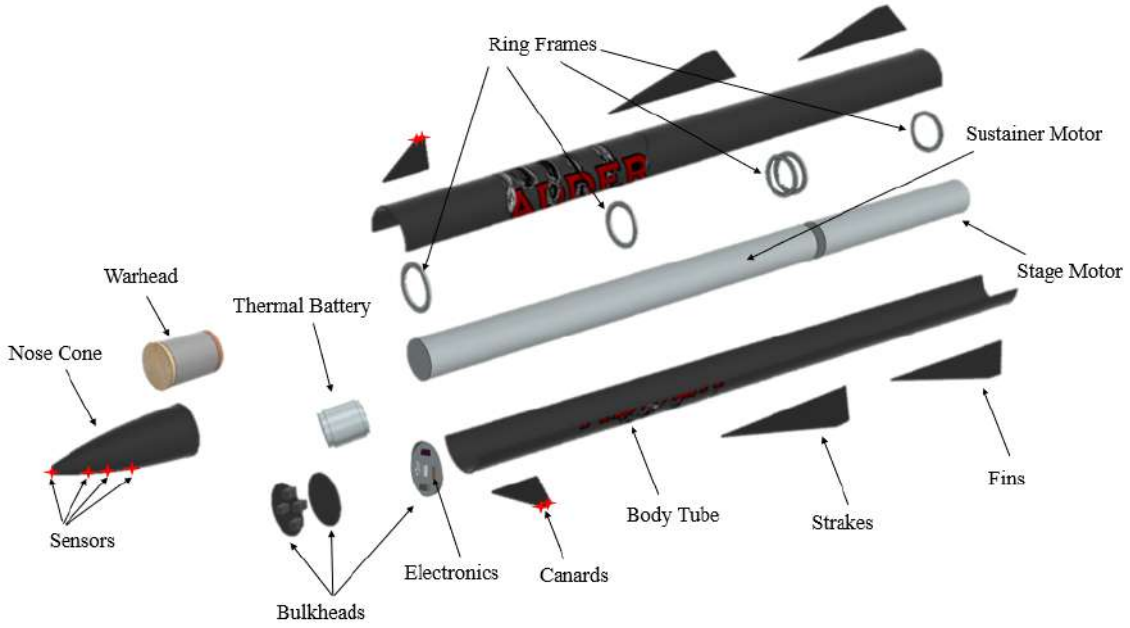

Fig. 18.0.3 Explosion View of the Adder

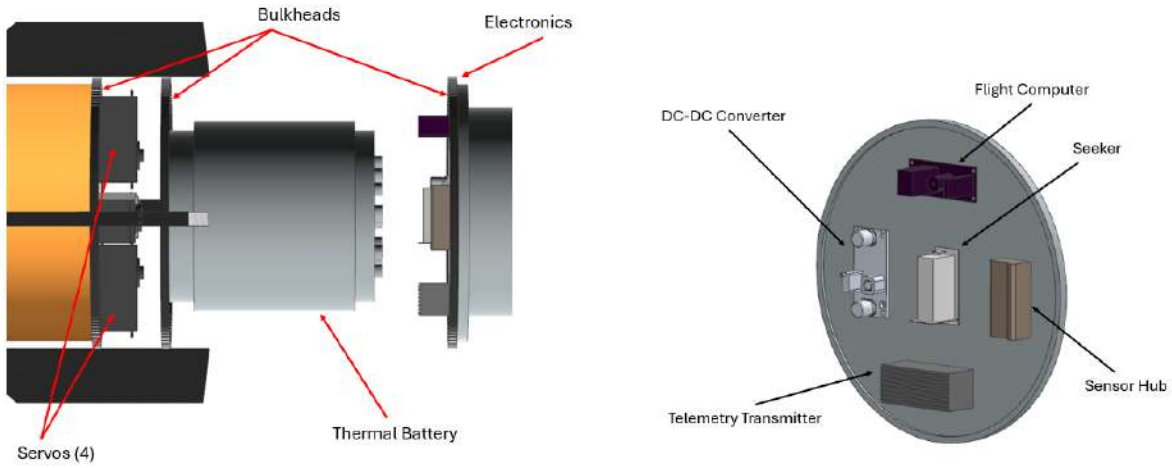

((a)) Detailed View of Electronics System ((b)) Electronics Bulkhead

Fig. 18.0.4 Electronics System and Bulkhead Views

Figure 18.0.5 shows the true size of the sensors represented by the red stars in Figure 18.0.3.

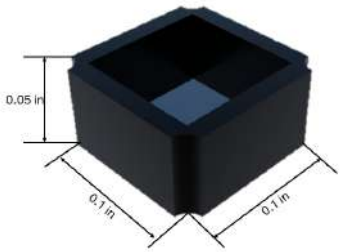

Fig. 18.0.5 Adder Sensors

Figures 18.0.6 through 18.0.9 show various situational renderings of the Adder in action.

Fig. 18.0.6 Adder Performing Tail Chase with Enemy Threat

Fig. 18.0.7 Adder Loaded in a Humvee

Fig. 18.0.8 Adder Launch

Fig. 18.0.9 Adder Upon Intercept with Enemy Target

19. Manufacturing, Fielding, Logistics, Handling, & Deployment

This section describes how the missile has been designed with achievable manufacturability, logistical deployment, and the ability field service as objectives. The main production zones were established based

on the various component groups and ordered to achieve material flow.

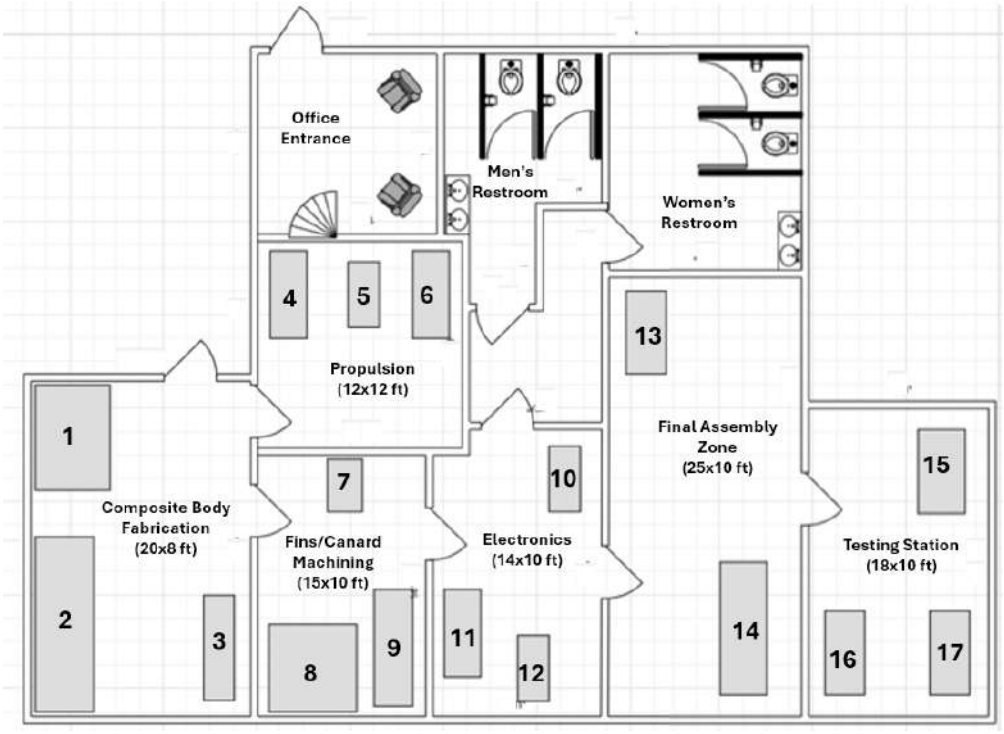

Fig. 19.0.1 Manufacturing Floor Plan Floor One

Table 19.0.1 below gives specifications for each numbered part on the manufacturing floor.

Table 19.0.1 Missile Production Equipment with Dimensions and Estimated Weights

Part No.	Name	Length (ft)	Width (ft)	Height (ft)	Weight (lbs)
1	Autoclave	6	5	7	3200
2	CNC Filament Winder	10	4	6	2400
3	Cleanroom Table	6	3	3	250
4	Motor Stands	6	3	3	300
5	Torque Area	4	2	3	200
6	Ring Frame Jig	6	3	3	280
7	Deburr	3	2	4	180
8	CNC Mill	6	6	7	3600
9	Precision Bench	6	2	3	220
10	Scope Table	4	2	3	180

Continued on next page

Table 19.0.1 – continued from previous page

Part No.	Name	Length (ft)	Width (ft)	Height (ft)	Weight (lbs)
11	ESD Bench	6	2	3	210
12	Reflow Oven	4	2	2.5	160
13	Alignment Lasers/Bench	6	2	4	200
14	Rotating Jig	8	3	3.5	420
15	CG Balance	6	3	3	400
16	Telemetry Bench	6	2	3	210
17	Electrical Harness Bench	6	2	3	230

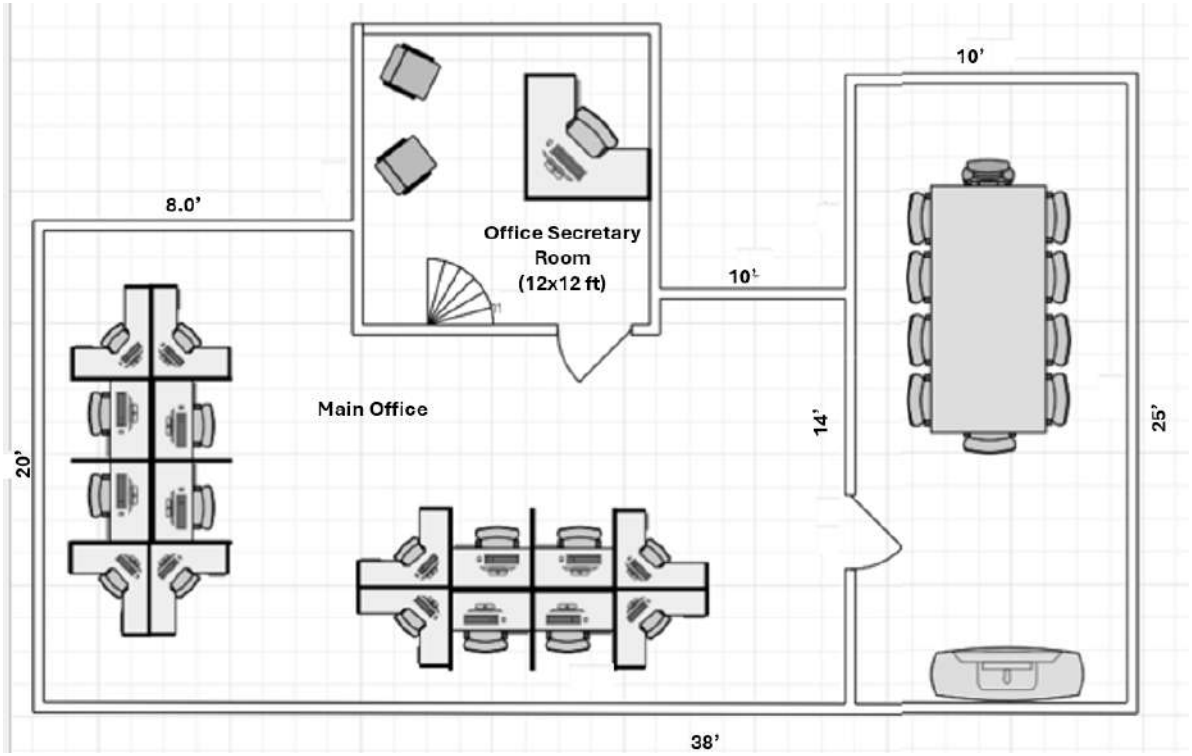

Fig. 19.0.2 Manufacturing Floor Plan Floor Two

The manufacturing strategy places an emphasis on modularity, affordability, safety, and rapid scalability. The production target is 1,000 missiles per year for 10 years, with an additional 100 units designated for developmental testing.

To meet manufacturing and safety specifications, a dual-zoned manufacturing facility layout is proposed. This will include a structural assembly zone, a explosive secure zone, composite layup area, and system integration zone. The layout of these areas are deliberately organized to optimize the flow of production,

while ensuring quality control and warhead manufacturing safety.

The overall process of manufacturing can be summarized by the following flowcharts, shown in Figures 19.0.3 and 19.0.4 below. In order to remain ITAR and EAR compliant, two separate manufacturing processes must be defined: one for domestic sales, and one for exported sales. The overall machining of the components remains the same, however the exported version will not include electronics and warhead assembly.

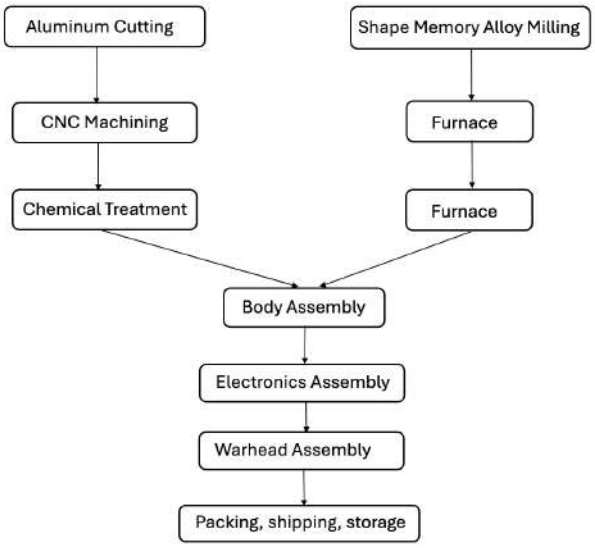

Fig. 19.0.3 Domestic Manufacturing Flow-chart

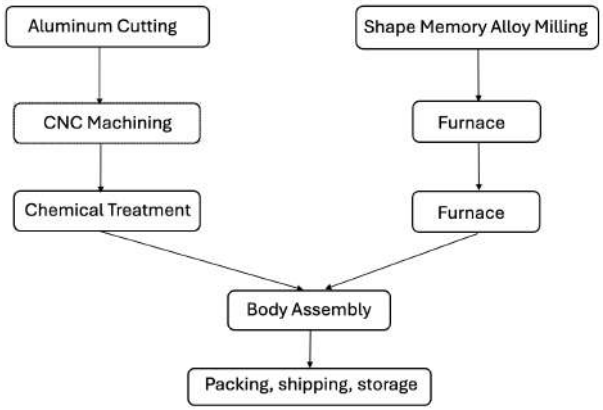

Fig. 19.0.4 Export Manufacturing Flow-chart

The production will begin in the structural assembly zone. Here, raw materials like aluminum and carbon fiber components are machined, joined, and inspected for quality assurance and material tolerances. This zone will house the CNC machines and drill presses necessary to create ring frames, fuselage sections, and support structures.

An exploded view of the materials used for each component for both the black aluminum surface version and the shape memory alloy surface version are shown in Figures 19.0.5 and 19.0.6.

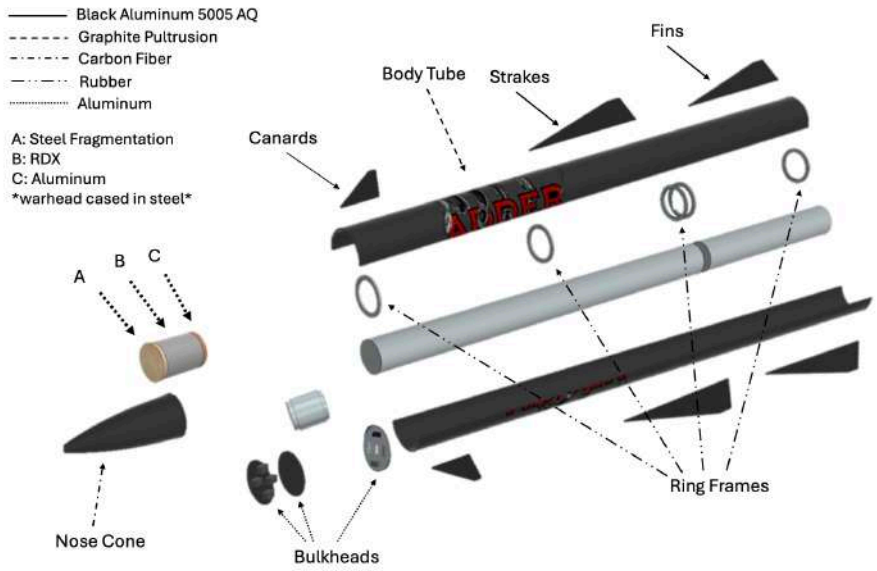

Fig. 19.0.5 Materials Breakout for Black Aluminum Version

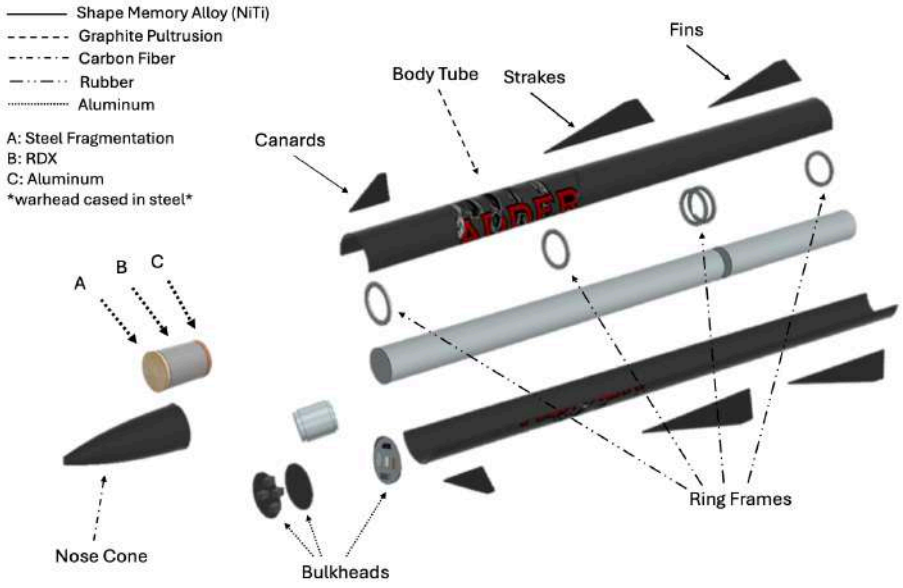

Fig. 19.0.6 Materials Breakout for Shape Memory Alloy Version

Manufacturing begins in the composite body fabrication area. Here the carbon fiber airframe sections are filament wound, cured in an autoclave, and prepped for structural combining. The fin and canard control surfaces are made from a 30mm aluminum plate using CNC milling, then finishing and deburr processes are completed on precision benches. Propulsion integration is done in a fireproof bay where the motor and ring frame assemblies are mounted using motor cradle jigs and torque fixtures. Electronics are assembled in a controlled ESD environment with benches for surface mount soldering, reflow oven operation, and signal

testing. All electronic modules undergo bench-level verification prior to integration into the main airframe, each employee utilizing a bench will be grounded using a grounding bracelet.

Final assembly is performed in an open area. Here, the completed subsystems are brought together using a rotating missile stand and aligned with laser fixtures. An overhead crane supports safe lifting and module alignment, this is not included in the image due to the 2D image constraints, but will be mounted above these stations in the final assembly room. Once the airframe, control fins, propulsion system, and electronics are fully integrated, the system is moved to the testing station. There, CG balancing and telemetry verification are performed to validate system readiness.

The warhead integration occurs in an isolated, access-restricted area of the facility as seen in Figure 19.0.7. Fragmentation material is packed and secured within the warhead casing, and the arming circuit is installed and locked out until field activation. This separation ensures that accidental ignition or mishandling does not compromise the main assembly line.

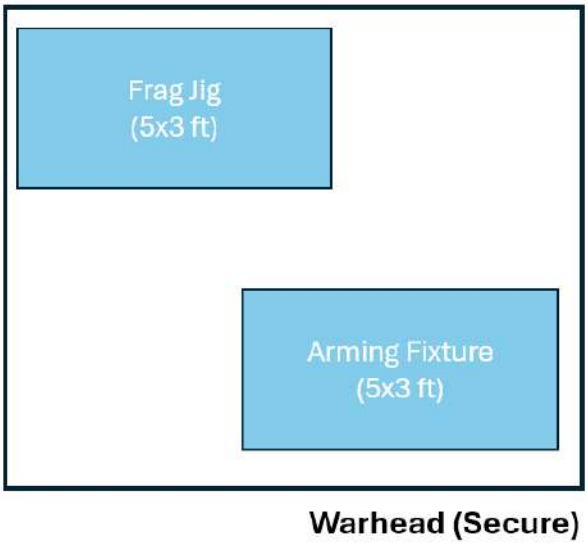

Fig. 19.0.7 Warhead Integration Floor Plan

19.1. Fielding and Logistics

The missile system is designed for streamlined fielding. Parts of assemblies are packaged in standard transport crates with provisions for shock isolation and climate control. All crates have serial identification numbers and digital documenting, which allows for traceable inventory during shipping and storage. The nature of the design supports distributed deployment strategies, including pre-staged kits at front operating bases or air deployed repairs. Logistics are simplified by minimizing custom components and leveraging COTS elements in the guidance and power systems. This reduces maintenance time and ensures availability of

replacement parts. Each crate includes QR-coded packing lists, torque specs, and environmental conditioning requirements for inventory and inspection at checkpoints.

19.2. Handling and Deployment

Handling procedures follow established safety protocols. All lifting of the missile is performed with rated fixtures and support stands. Connectors and modules are keyed to prevent incorrect mating, and assembly steps are guided by color coded and torque specified fasteners. Ground crews can assemble, test, and deploy a single unit using two personnel. Overall, the missile's architecture, ground support design, and packaging approach ensure an achievable deployment with smaller logistics burden.

19.3. Bill of Materials

To gain more insight on the specific costs of each component of the missile, a Bill of Materials was created. This listed every component, its material, its weight, and the cost. The amounts were then summed to find the total cost of the missile itself. The four versions of the missile (domestic with black aluminum surfaces, domestic with shape memory alloy surfaces, exported with black aluminum surfaces, and exported with shape memory alloy surfaces) were analyzed. Wherever possible, components were sourced from the United States or friendly nations. Note that most prices listed here are highly conservative, as the lower prices from economies of scale that would be leveraged when in serial production were not accounted for.

Table 19.3.1 Domestic Version Cost Analysis Including Black Aluminum Surfaces

Part Number	Component	Material	Quantity	Area (ft^2)	Thickness (in.)	Volume (in^3)	Density (lb/in^3)	Weight (lb.)	Unit Cost	Total Cost
1	Canards	Black Aluminum 5005 AQ [63]	4	0.2108	0.06	7.285	0.097	0.706	$10.00	$28.27
2	First Stage Fins	Black Aluminum 5005 AQ [64]	4	0.8132	0.06	28.10	0.097	1.817	$10.00	$109.04
3	Second Stage Fins	Black Aluminum 5005 AQ [65]	4	0.8333	0.06	28.79	0.097	1.862	$10.00	$111.74
4	Stage 1 Motor Reload Kit	AeroTech M1419	1	-	-	-	-	15.2	$1,000	$1,000
5	Stage 2 Motor Reload Kit	Cesaroni N5800	1	-	-	-	-	32.7	$1,200	$1,200
6	Stage 1 Motor Hardware	Cesaroni 98-6XL	1	-	-	-	-	-	$915.89	$915.89
7	Stage 2 Motor Hardware	AeroTech RMS-98/7680	1	-	-	-	-	-	$925.99	$ 925.99
8	EAP-12155B Thermal Battery	Steel [66]	1	-	-	-	-	1.3	$250.00	$250.00
9	Actuators	Apogee Metal Gear Servos [67]	6	-	-	-	-	1.5	$10	$60.00
10	Ring Frames	Apogee Bulkhead Mounts [68]	3	-	-	-	-	1.5	$20	$60.00
11	Graphite Pultrusion Body	Graphite Pultrusion [69]	1	23.565	0.125	206.78	0.06	12.407	$ 834.60	$834.60
12	Misc. Hardware	Fasteners, wiring, mounts	-	-	-	-	-	3	$75.00	$75.00
13	Deflagration Line	Nichrime wire-based separation line [70]	1	-	-	-	-	0.3	$45.00	$45.00
14	DC-DC Converters	Power Regulation Modules [71]	4	-	-	-	-	0.6	$25.00	$60.00
15	Arming Circuit	Isolated Trigger Electronics [72]	1	-	-	-	-	0.2	$ 40.00	$40.00
16	Universal Connector Port	Custom I/O Housing [73]	1	-	-	-	-	0.5	$25.00	$25.00
17	Charging interface	Wireless Charging Coil [74]	1	-	-	-	-	0.4	$35.00	$35.00
18	Power Management	Integrated Power Distribution Board [75]	1	-	-	-	-	0.3	$50.00	$50.00
19	IR Sensors	Plastic, sensor crystal [76]	14	-	-	-	-	-	$45.00	$630.00
20	Custom IR Sensor Lenses	Glass [77]	14	-	-	-	-	-	$60.00	$840.00
21	Qualcomm QCS6490 CPU	Silicon [78]	1	-	-	-	-	-	$87.14	$87.14
22	Crucial 16GB DDR4 Laptop Ram	Silicon [79]	1	-	-	-	-	-	$30.00	$30.00
23	High Speed Hard Drive	Silicon [80]	1	-	-	-	-	-	$33.00	$33.00
24	IMU	Silicon [81]	1	-	-	-	-	-	$106.67	$106.67
25	Custom PCB	Silicon, Copper [82]	1	-	-	-	-	-	$20.00	$20.00
26	Nose Cone	Carbon Fiber [83]	1	1.089	0.125	98.175	0.056	1	$326.70	$326.70
27	Servos	High Torque Waterproof Digital Servo [84]	4	-	-	-	-	0.582	$21.99	$87.96
TOTALS								77.71		$7,660.28

Table 19.3.2 Domestic Version Cost Analysis Including Shape Memory Alloy Surfaces

Part Number	Component	Material	Quantity	Area (ft^2)	Thickness (in.)	Volume (in^3)	Density (lb/in^3)	Weight (lb.)	Unit Cost	Total Cost
1	Canards	Shape Memory Alloy [85]	4	0.2108	0.06	7.285	0.276	2.01	$48.00	$192.00
2	First Stage Fins	Shape Memory Alloy [85]	4	0.8132	0.06	28.104	0.276	7.757	$72.00	$288.00
3	Second Stage Fins	Shape Memory Alloy [85]	4	0.8333	0.06	28.799	0.276	7.798	$66.00	$264.00
4	Stage 1 Motor Reload Kit	AeroTech M1419	1	-	-	-	-	15.2	$1,000	$1,000
5	Stage 2 Motor Reload Kit	Cesaroni N5800	1	-	-	-	-	32.7	$1,200	$1,200
6	Stage 1 Motor Hardware	Cesaroni 98-6XL	1	-	-	-	-	-	$915.89	$915.89
7	Stage 2 Motor Hardware	AeroTech RMS-98/7680	1	-	-	-	-	-	$925.99	$ 925.99
8	EAP-12155B Thermal Battery	Steel [66]	1	-	-	-	-	1.3	$250.00	$250.00
9	Actuators	Apogee Metal Gear Servos [67]	6	-	-	-	-	1.5	$10	$60.00
10	Ring Frames	Apogee Bulkhead Mounts [68]	3	-	-	-	-	1.5	$20	$60.00
11	Graphite Pultrusion Body	Graphite Pultrusion [69]	1	23.565	0.125	206.78	0.06	12.407	$ 834.60	$834.60
12	Misc. Hardware	Fasteners, wiring, mounts	-	-	-	-	-	3	$75.00	$75.00
13	Deflagration Line	Nichrime wire-based separation line [70]	1	-	-	-	-	0.3	$45.00	$45.00
14	DC-DC Converters	Power Regulation Modules [71]	4	-	-	-	-	0.6	$25.00	$60.00
15	Arming Circuit	Isolated Trigger Electronics [72]	1	-	-	-	-	0.2	$ 40.00	$40.00
16	Universal Connector Port	Custom I/O Housing [73]	1	-	-	-	-	0.5	$25.00	$25.00
17	Charging interface	Wireless Charging Coil [74]	1	-	-	-	-	0.4	$35.00	$35.00
18	Power Management	Integrated Power Distribution Board [75]	1	-	-	-	-	0.3	$50.00	$50.00
19	IR Sensors	Plastic, sensor crystal [76]	14	-	-	-	-	-	$45.00	$630.00
20	Custom IR Sensor Lenses	Glass [77]	14	-	-	-	-	-	$60.00	$840.00
21	Qualcomm QCS6490 CPU	Silicon [78]	1	-	-	-	-	-	$87.14	$87.14
22	Crucial 16GB DDR4 Laptop Ram	Silicon [79]	1	-	-	-	-	-	$30.00	$30.00
23	High Speed Hard Drive	Silicon [80]	1	-	-	-	-	-	$33.00	$33.00
24	IMU	Silicon [81]	1	-	-	-	-	-	$106.67	$106.67
25	Custom PCB	Silicon, Copper [82]	1	-	-	-	-	-	$20.00	$20.00
26	Nose Cone	Carbon Fiber [83]	1	1.089	0.125	98.175	0.056	1	$326.70	$326.70
27	Servos	High Torque Waterproof Digital Servo [84]	4	-	-	-	-	0.582	$21.99	$87.96
TOTALS								92.236		$8,481.95

Table 19.3.3 Export Version Cost Analysis Including Black Aluminum Surfaces

Part Number	Component	Material	Quantity	Area (ft^2)	Thickness (in.)	Volume (in^3)	Density (lb/in^3)	Weight (lb.)	Unit Cost	Total Cost
1	Canards	Black Aluminum 5005 AQ [63]	4	0.2108	0.06	7.285	0.097	0.706	$10.00	$28.27
2	First Stage Fins	Black Aluminum 5005 AQ [64]	4	0.8132	0.06	28.10	0.097	1.817	$10.00	$109.04
3	Second Stage Fins	Black Aluminum 5005 AQ [65]	4	0.8333	0.06	28.79	0.097	1.862	$10.00	$111.74
4	Actuators	Apogee Metal Gear Servos [67]	6	-	-	-	-	1.5	$10	$60.00
5	Ring Frames	Apogee Bulkhead Mounts [68]	3	-	-	-	-	1.5	$20	$60.00
6	Graphite Pultrusion Body	Graphite Pultrusion [69]	1	23.565	0.125	206.78	0.06	12.407	$ 834.60	$834.60
7	Misc. Hardware	Fasteners, wiring, mounts	-	-	-	-	-	3	$75.00	$75.00
8	Deflagration Line	Nichrime wire-based separation line [70]	1	-	-	-	-	0.3	$45.00	$45.00
9	DC-DC Converters	Power Regulation Modules [71]	4	-	-	-	-	0.6	$25.00	$60.00
10	Arming Circuit	Isolated Trigger Electronics [72]	1	-	-	-	-	0.2	$ 40.00	$40.00
11	Universal Connector Port	Custom I/O Housing [73]	1	-	-	-	-	0.5	$25.00	$25.00
12	Charging interface	Wireless Charging Coil [74]	1	-	-	-	-	0.4	$35.00	$35.00
13	Power Management	Integrated Power Distribution Board [75]	1	-	-	-	-	0.3	$50.00	$50.00
14	High Speed Hard Drive	Silicon [80]	1	-	-	-	-	-	$33.00	$33.00
15	Nose Cone	Carbon Fiber [83]	1	1.089	0.125	98.175	0.056	1	$326.70	$326.70
16	Servos	High Torque Waterproof Digital Servo [84]	4	-	-	-	-	0.582	$163.99	$87.96
TOTALS								31.542		$1,981.31

Table 19.3.4 Export Version Cost Analysis Including Shape Memory Alloy Surfaces

Part Number	Component	Material	Quantity	Area (ft^2)	Thickness (in.)	Volume (in^3)	Density (lb/in^3)	Weight (lb.)	Unit Cost	Total Cost
1	Canards	Shape Memory Alloy [85]	4	0.2108	0.06	7.285	0.276	2.01	$48.00	$192.00
2	First Stage Fins	Shape Memory Alloy [85]	4	0.8132	0.06	28.104	0.276	7.757	$72.00	$288.00
3	Second Stage Fins	Shape Memory Alloy [85]	4	0.8333	0.06	28.799	0.276	7.798	$66.00	$264.00
4	Actuators	Apogee Metal Gear Servos [67]	6	-	-	-	-	1.5	$10	$60.00
5	Ring Frames	Apogee Bulkhead Mounts [68]	3	-	-	-	-	1.5	$20	$60.00
6	Graphite Pultrusion Body	Graphite Pultrusion [69]	1	23.565	0.125	206.78	0.06	12.407	$ 834.60	$834.60
7	Misc. Hardware	Fasteners, wiring, mounts	-	-	-	-	-	3	$75.00	$75.00
8	Deflagration Line	Nichrime wire-based separation line [70]	1	-	-	-	-	0.3	$45.00	$45.00
9	DC-DC Converters	Power Regulation Modules [71]	4	-	-	-	-	0.6	$25.00	$60.00
10	Arming Circuit	Isolated Trigger Electronics [72]	1	-	-	-	-	0.2	$ 40.00	$40.00
11	Universal Connector Port	Custom I/O Housing [73]	1	-	-	-	-	0.5	$25.00	$25.00
12	Charging interface	Wireless Charging Coil [74]	1	-	-	-	-	0.4	$35.00	$35.00
13	Power Management	Integrated Power Distribution Board [75]	1	-	-	-	-	0.3	$50.00	$50.00
14	High Speed Hard Drive	Silicon [80]	1	-	-	-	-	-	$33.00	$33.00
15	Nose Cone	Carbon Fiber [83]	1	1.089	0.125	98.175	0.056	1	$326.70	$326.70
16	Servos	High Torque Waterproof Digital Servo [84]	4	-	-	-	-	0.582	$21.99	$87.96
TOTALS								43.036		$2,476.26

The cost of the components were either determined by getting a direct quote from the source, or by calculation, using the volume, density, quantity, unit cost, and weight of the material.

20. Class 2 Cost Analysis

To ensure the unit cost of the missile was below $10,000, a comprehensive life-cycle cost analysis was performed. Figure 20.0.1, below displays how decisions made in the design of the missile have influenced the overall life-cycle cost. The figure was created using an example model that allowed for estimations of the percentage of total life-cycle cost during each major phase of design and manufacturing.

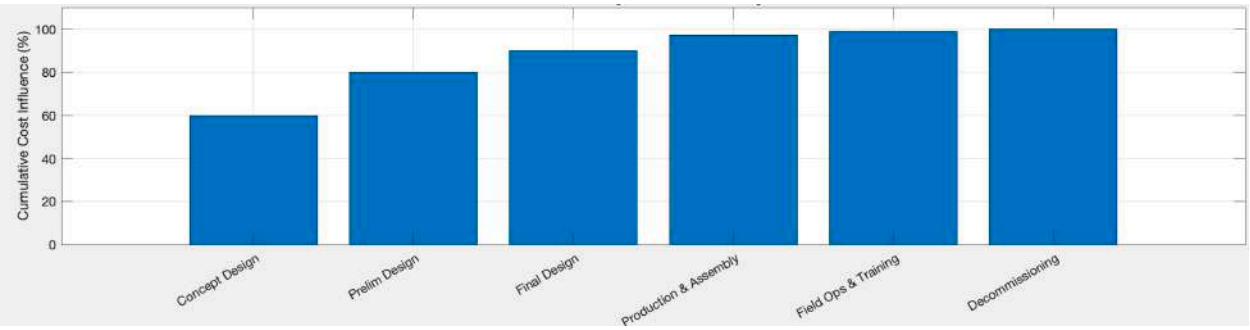

Fig. 20.0.1 Life-cycle Cost Influence by Phase

The six phases are defined below:

1) Concept Design (60%): Configuration layout, propulsion mode studies.
2) Preliminary Design (80%): Initial CAD, CG balancing, material tradeoffs.
3) Final Design (90%): BOM finalization, structural/electronic layout closure.

4) Production & Assembly (97%): Fabrication, QA, tooling.

5) Field Ops & Training (98%): Crating, documentation, launcher integration.

6) Decommissioning (100%): Safe disarmament, recycling, record-keeping.

The magnitude of the phase influence was determined from material cost estimates and design control selections:

$$I = 10,\ 20,\ 25,\ 30,\ 10,\ 5 \quad \text{where} \quad I_i = 100\% \tag{53}$$

The annual contribution to life-cycle costs is displayed in Figure 20.0.2. This shows the evolving cost profile over a 15-year interval.

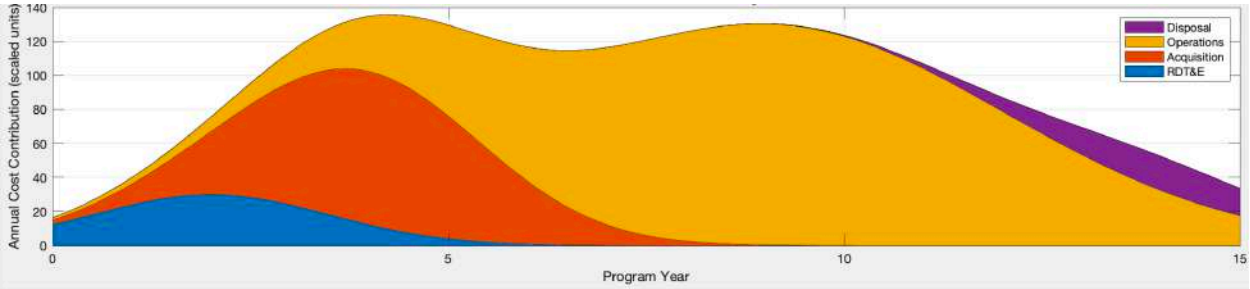

Fig. 20.0.2 Annual Life-cycle Cost Contribution

The life-cycle categories are modeled using a Gaussian distribution:

$$C_j t = A_j \cdot \exp\left(-\frac{1}{2} \cdot \left(\frac{t-\mu_j}{\sigma_j}\right)^2\right) \tag{54}$$

Table 20.0.1 Gaussian Parameters Used for Annual Life-cycle Cost Modeling

Category	A_j (arbitrary units)	μ_j (yrs)	σ_j (yrs)
RDT&E	30	2	1.5
Acquisition	90	4	1.5
Operations	130	9	3.0
Disposal	20	14	1.5

Where, A_j is the peak cost contribution, μ_j is the center of distribution, and σ_j is the standard deviation. The total cost function is:

$$C_{\text{total}} t = \sum_{j=1}^{4} C_j t \tag{55}$$

Finally, the life-cycle cost analysis concluded with analyzing the projected life-cycle costs by calendar year, shown by Figure 20.0.3, noting that the operations cost is projected to peak in the year 2030.

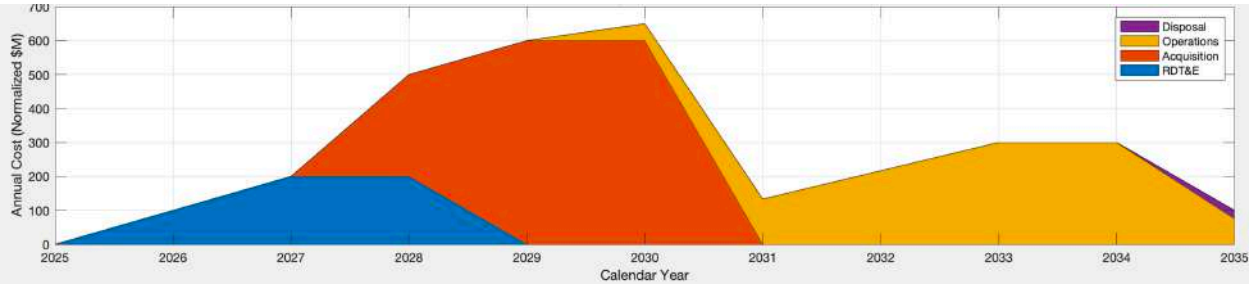

Fig. 20.0.3 Life-cycle Cost Projection by Calendar Year

The assigned influence percentages for each life-cycle phase are backed by data from the BOM (Table ??) and manufacturing plan. These values reflect when major financial and engineering decisions are made:

Table 20.0.2 Life-cycle Phase Influence Summary

Phase	Key Cost Drivers	% Influence
Concept Design	Airframe sizing, propulsion studies	10%
Preliminary Design	CG tradeoffs, material selection	20%
Final Design	CAD finalization, IR sensor count	25%
Production & Assembly	CNC, filament winding, QA	30%
Field Operations	Packaging, training kits, integration	10%
Decommissioning	Sensor recycling, disarmament protocols	5%

This life-cycle cost analysis combines analytical modeling and program-specific data to show how design choices dictate and influence the long-term affordability. The use of low-cost COTS components, modular design, and a streamlined factory layout allowed for maximum control over the life-cycle costs during the conceptual and design phases.

References

[1] Trevithick, J., "Turkish Laser-Guided Artillery Rockets Could Be Giving Ukraine A New Capability," , 2024. URL https://www.twz.com/turkish-laser-guided-artillery-rockets-could-be-giving-ukraine-new-capability, accessed: 2025-05-02.

[2] Kelly, F., "Dynetics awarded up to $470 million for small glide bombs for US special operations," , 2018. URL https://thedefensepost.com/2018/06/11/dynetics-small-glide-munition-socom-470-million-contract/, accessed: 2025-05-02.

[3] Wikipedia contributors, "Cruise missile," , 2025. URL https://en.wikipedia.org/wiki/Cruise_missile, accessed: 2025-05-02.

[4] Roblin, S., "Tactical Ballistic Missiles are Coming (Maybe)," , 2019. URL https://nationalinterest.org/blog/buzz/tactical-ballistic-missiles-are-coming-maybe-138317, accessed: 2025-05-02.

[5] Parrot, "Use Case: Military & Defense," , 2025. URL https://www.parrot.com/en/use-cases/military-and-defense, accessed: 2025-05-02.

[6] Inert Products LLC, "105mm M1 NATO HE Artillery Shell with Fuze – Inert Replica," , 2025. URL https://inertproducts.com/product/105mm-m1-he-artillery-shell-with-fuze-inert-replica-training-aid/, accessed: 2025-05-02.

[7] AeroContact, "AIM-9X Sidewinder," AeroContact, 2025. URL https://aerocontact.b-cdn.net/public/img/aviaexpo/produits/images/265/detail_AIM-9X-Sidewinder3-900x636.jpg, accessed: 2025-02-08.

[8] OpenRocket Team, "OpenRocket: An Open Source Model Rocket Simulation Software," https://openrocket.info, 2025. Accessed: 2025-05-14.

[9] FLIR, "Can Thermal Imaging See Through Fog and Rain?" , 2020. URL https://www.flir.com/discover/rd-science/can-thermal-imaging-see-through-fog-and-rain/.

[10] Darat, B. M., "Mengenal Canister Launcher System – Ujung Tombak Satuan Tembak Hanud NASAMS," , 2020. URL https://www.indomiliter.com/mengenal-canister-launcher-system-ujung-tombak-satuan-tembak-hanud-nasams/, accessed: April 6, 2025.

[11] Coker, J., "AeroTech M1419W," , 2025. URL https://www.thrustcurve.org/motors/AeroTech/M1419W/.

[12] Coker, J., "Cesaroni 20146N5800-P," , 2025. URL https://www.thrustcurve.org/motors/Cesaroni/20146N5800-P/.

[13] American Institute of Aeronautics and Astronautics (AIAA), "2024-2025 Missile Systems Technical Committee Missile Design Competition," , 2024. URL https://www.aiaa.org/docs/default-source/uploadedfiles/membership-and-communities/university-students/design-competitions/2024-25-mstc_missile_design_competition_2025.pdf, accessed: 2024-10-27.

[14] Army Recognition, "Raytheon's SeaRAM intercepts target for the first time with a RAM Block 2 missile," Online Article, 2016. URL https://www.armyrecognition.com/news/navy-news/2016/raytheons-searam-intercepts-target-for-the-first-time-with-a-ram-block-2-missile, accessed: 2025-02-09.

[15] Mer et Marine, "En images: Tir d'Aster 30 sur la frégate Forbin," Online Article, 2017. URL https://www.meretmarine.com/fr/defense/en-images-tir-d-aster-30-sur-la-fregate-forbin, accessed: 2025-02-09.

[16] Defense Industry Daily, "India Israel's Barak-8 SAM Development Project(s)," Online Article, 2021. URL https://www.defenseindustrydaily.com/india-israel-introducing-mr-sam-03461/, accessed: 2025-02-09.

[17] PD-Photos, "ILA Berlin 2012," Wikimedia Commons, 2012. URL https://commons.wikimedia.org/wiki/File:ILA_Berlin_2012_PD_036.JPG, accessed: 2025-02-08.

[18] CAT-UXO, "SA-15 Gauntlet (9M330 Tor) Missile," , 2025. URL https://cat-uxo.com/explosive-hazards/missiles/sa-15-gauntlet-9m330-tor-missile, accessed: 2025-02-08.

[19] TVD, "SA-6 Gainful (2K12 Kub) Surface-to-Air Missile (SAM) System," , 2024. URL https://tvd.im/land-systems/2884-sa-6-gainful-2k12-kub.html, accessed: February 9, 2025.

[20] Wikipedia contributors, "MICA (missile)," , 2024. URL https://en.wikipedia.org/wiki/MICA_(missile), accessed: February 9, 2025.

[21] Shutterstock Contributors, "FIM-92 Stinger Illustrations," , 2024. URL https://www.shutterstock.com/search/fim-92-stinger?image_type=illustration, accessed: February 9, 2025.

[22] DebkaFile Editorial Team, "Friction with Cairo Over the Israel Air Defense System for Ethiopia's Great Nile Dam," Online Article, 2025. URL https://www.debka.com/friction-with-cairo-over-the-israel-air-defense-system-for-ethiopias-great-nile-dam/, accessed: 2025-02-09.

[23] Missilery.info, "Crotale Surface-to-Air Missile System," Online Article, 2025. URL https://en.missilery.info/missile/crotale, accessed: 2025-02-09.

[24] News, B., "Syrian Military Blamed for Homs Bombing," , 2012. URL https://www.bbc.com/news/world-middle-east-20385306, accessed: 2025-02-08.

[25] Office, U. G. A., "Surface-to-Air Missiles: Assessment of Capabilities and Challenges," Tech. Rep. GAO-23-106717, U.S. Government Accountability Office, 2023. URL https://www.gao.gov/products/gao-23-106717, accessed: 2025-02-08.

[26] Deagel, "BM-21 Grad Multiple Launch Rocket System (MLRS)," , Feb 2025. URL https://www.deagel.com/Artillery/Grad/a0000032, accessed on February 27, 2025.

[27] Deagel, "9K58 Smerch Multiple Launch Rocket System (MLRS)," , Feb 2025. URL https://www.deagel.com/Artillery/Smerch/a0000033, accessed on February 27, 2025.

[28] Deagel, "FAB-500 General Purpose Bomb," , Feb 2025. URL https://www.deagel.com/Bombs/FAB-500/a0000034, accessed on February 27, 2025.

[29] for Strategic, C., and Studies, I., "3M-14 Kalibr (SS-N-30A)," , April 2024. URL https://missilethreat.csis.org/missile/ss-n-30a/, accessed on March 2, 2025.

[30] Tuzov, B., "Kalibr Cruise Missiles: How Does Ukraine Cope with Them?" , Nov 2023. URL https://www.kyivpost.com/post/24105, accessed on March 2, 2025.

[31] Missile Defense Project, "3M-14 Kalibr (SS-N-30A)," , Apr 2024. URL https://missilethreat.csis.org/missile/ss-n-30a/, last modified April 23, 2024. Accessed on February 27, 2025.

[32] Project, M. D., "9K720 Iskander (SS-26)," , Apr 2024. URL https://missilethreat.csis.org/missile/ss-26-2/, last modified April 23, 2024. Accessed on February 27, 2025.

[33] Army Recognition, "Shahed-136 Loitering Munition / Kamikaze-Suicide Drone - Iran," , Nov 2024. URL https://www.armyrecognition.com/Shahed-136_loitering_munition_suicide_kamikaze_drone_Iran, accessed on February 27, 2025.

[34] Geneva International Centre for Humanitarian Demining (GICHD), "Characterisation of Explosive Weapons, Annex B – 152 mm & 155 mm Artillery Guns," , Feb 2017. URL https://www.gichd.org/, accessed on February 27, 2025.

[35] Brickmania, "SEARAM Ship Defense System Specifications," Online Article, 2025. URL https://www.brickmania.com/searam-ship-defense-system/, accessed: 2025-02-09.

[36] Trevithick, J., "Intact Laser Fuse Section Of An Iron Dome Tamir Interceptor Fell Into Gaza," The War Zone, 2021. URL https://www.twz.com/31018/intact-laser-fuse-section-of-an-iron-dome-tamir-interceptor-fell-into-gaza, accessed: February 9, 2025.

[37] Technologies, R., "Iron Dome," , 2024. URL https://www.rtx.com/raytheon/what-we-do/integrated-air-and-missile-defense/irondome, accessed: February 9, 2025.

[38] IAS, N., "Iron Dome: Israel's Air Defense System," , 2024. URL https://www.nextias.com/blog/iron-dome/, accessed: February 9, 2025.

[39] Guy, J., and Valinsky, J., "What is Israel's Iron Dome and how does it work?" CNN, 2023. URL https://www.cnn.com/2023/10/09/world/iron-dome-israel-defense-explained-intl-dg/index.html, accessed: February 9, 2025.

[40] Jane's Weapons Systems: Naval 2015-2016, Jane's Information Group, 2015.

[41] Navy, U. S., "RIM-116 Rolling Airframe Missile (RAM)," , 2024. URL https://www.navy.mil/Resources/Fact-Files/Display-FactFiles/Article/2168961/rim-116-rolling-airframe-missile-ram/, accessed: February 9, 2025.

[42] Jane's Weapons Systems: Air-Launched 2015-2016, Jane's Information Group, 2015.

[43] GlobalSecurity.org, "Barak NG (Next Generation)," , 2024. URL https://www.globalsecurity.org/military/world/israel/barak-ng.htm, accessed: February 9, 2025.

[44] Army Technology, "Umkhonto Ground-Based Launcher System," Online Article, 2025. URL https://www.army-technology.com/projects/umkhonto-ground-based-launcher-system/, accessed: 2025-02-09.

[45] Naval Technology, "Umkhonto Surface-to-Air Missile," Online Article, 2025. URL https://www.naval-technology.com/projects/umkhonto-surface-to-air-missile/, accessed: 2025-02-09.

[46] DefenceWeb, "Denel Upgrading Umkhonto Missile," Online Article, 2025. URL https://www.defenceweb.co.za/industry/industry-industry/denel-upgrading-umkhonto-missile/, accessed: 2025-02-09.

[47] Wikipedia Contributors, "Umkhonto (missile)," Wikipedia, The Free Encyclopedia, 2025. URL https://en.wikipedia.org/wiki/Umkhonto_(missile), accessed: 2025-02-09.

[48] Wikipedia Contributors, "SPYDER (missile system)," Wikipedia, The Free Encyclopedia, 2025. URL https://en.wikipedia.org/wiki/SPYDER, accessed: 2025-02-09.

[49] Technology, A., "VL MICA," , 2024. URL https://www.army-technology.com/projects/vlmica/?cf-view&cf-closed, accessed: February 9, 2025.

[50] Astronautix, "Kub (SA-6 Gainful)," , 2024. URL http://www.astronautix.com/k/kub.html, accessed: February 9, 2025.

[51] Wikiwand, "2K12 Kub," , 2024. URL https://www.wikiwand.com/en/articles/2%D0%9A12_Kub, accessed: February 9, 2025.

[52] Designation-Systems.net, "FIM-92 Stinger," , 2024. URL https://www.designation-systems.net/dusrm/m-92.html, accessed: February 9, 2025.

[53] Online, W. H., "FIM-92 Stinger: The Infamous Man-Portable Surface-to-Air Missile," , 2024. URL https://www.warhistoryonline.com/instant-articles/fim-92-stinger.html, accessed: February 9, 2025.

[54] ThePricer.org, "How Much Does a Stinger Missile Cost?" , 2024. URL https://www.thepricer.org/stinger-missile-cost/, accessed: February 9, 2025.

[55] Army Recognition, "Crotale Missile System (France)," Online Article, 2025. URL https://armyrecognition.com/military-products/army/air-defense-systems/air-defense-vehicles/crotale-missile-france-uk, accessed: 2025-02-09.

[56] Army Technology, "Crotale Surface-to-Air Missile System," Online Article, 2025. URL https://www.army-technology.com/projects/crotale/, accessed: 2025-02-09.

[57] Roskam, J., Airplane Design Part I: Preliminary Sizing of Airplanes, Design, Analysis and Research Corporation (DARcorporation), Lawrence, Kansas, USA, 2018.

[58] Apogee Rockets, "Aerotech 29mm Motor G80T-10," , 2025. URL https://www.apogeerockets.com/Rocket_Motors/AeroTech_Motors/29mm_Motors_Single_Use/Aerotech_29mm_Motor_G80T-10, accessed: Feb. 14, 2025.

[59] Electronics, B., "Back-illuminated higher sensitivity , high-speed , mid-wave infrared detector," , 2025. URL https://shop.boselec.com/collections/ir-detectors-high-performance-high-speed/products/back-illuminated-higher-sensitivity-high-speed-mid-wave-infrared-detector.

[60] Dreils, M., Weaponeering, AIAA, 2020.

[61] M. M. Islam, M. F. W. H., M. T. Islam, "Design of an X-band microstrip patch antenna with enhanced bandwidth," International Conference on Advances in Electrical Engineering, 2013.

[62] Fleeman, E. L., Tactical Missile Design, AIAA Education Series, 2001.

[63] Online Metals, "0.04" Anodized Aluminum Sheet Black 5005 AQ (23890)," , 2025. URL https://www.onlinemetals.com/en/buy/aluminum/0-04-anodized-aluminum-sheet-black-5005-aq/pid/23890, accessed: 2025-05-12.

[64] Online Metals, "0.04" Anodized Aluminum Sheet Black 5005 AQ (23891)," , 2025. URL https://www.onlinemetals.com/en/buy/aluminum/0-04-anodized-aluminum-sheet-black-5005-aq/pid/23891, accessed: 2025-05-12.

[65] Online Metals, "0.04" Anodized Aluminum Sheet Black 5005 AQ (23892)," , 2025. URL https://www.onlinemetals.com/en/buy/aluminum/0-04-anodized-aluminum-sheet-black-5005-aq/pid/23892, accessed: 2025-05-12.

[66] EaglePicher, "Battery Technical Datasheet EAP-12155B," , 2025. URL https://www.eaglepicher.com/sites/default/files/EAP-12155B%200622.pdf, accessed: 2025-05-12.

[67] Rockets, A., "Metal Gear Servos," , 2025. URL https://www.apogeerockets.com/Electronics-Payloads/Servo-Motors/Metal-Gear-Servos, accessed: 2025-05-12.

[68] Rockets, A., "Centering Rings / Bulkheads," , 2025. URL https://www.apogeerockets.com/Body-Tubes/Centering-Rings/Bulkheads, accessed: 2025-05-12.

[69] Composites, R. W., "Carbon Fiber Sheet - Part 15074," , 2025. URL https://www.rockwestcomposites.com/15074, accessed: 2025-05-12.

[70] Parts, R. M., "Initiators," , 2025. URL https://www.rocketmotorparts.com/Initiators/cat2721006_2702954.aspx, accessed: 2025-05-12.

[71] Adafruit, "Product 1385," , 2025. URL https://www.adafruit.com/product/1385, accessed: 2025-05-12.

[72] Adafruit, "Product 2896," , 2025. URL https://www.adafruit.com/product/2896, accessed: 2025-05-12.

[73] Adafruit, "Product 4753," , 2025. URL https://www.adafruit.com/product/4753, accessed: 2025-05-12.

[74] Adafruit, "Product 2465," , 2025. URL https://www.adafruit.com/product/2465, accessed: 2025-05-12.

[75] Adafruit, "Product 2030," , 2025. URL https://www.adafruit.com/product/2030, accessed: 2025-05-12.

[76] Electronics, B., "Mid-Wave IR Detector - Back Illuminated," , 2025. URL https://shop.boselec.com/collections/ir-detectors-high-performance-high-speed/products/back-illuminated-higher-sensitivity-high-speed-mid-wave-infrared-detector, accessed: 2025-05-12.

[77] Design, O. L., "Price of a Custom Lens," , 2025. URL https://www.opticalensdesign.com/price-of-a-custom-lens, accessed: 2025-05-12.

[78] Electronics, A., "Qualcomm QCS-6490-1-PSP1287," , 2025. URL https://www.arrow.com/en/products/qcs-6490-1-psp1287-tr-00-0-aa/qualcomm, accessed: 2025-05-12.

[79] Crucial, "16GB DDR4 RAM 3200MT/s," , 2025. URL https://www.bhphotovideo.com/c/product/1576452-REG/crucial_ct16g4sfra32a_16gb_ddr4_3200_mt_s.html, accessed: 2025-05-12.

[80] Kingston, "DataTraveler Max 256GB USB Drive," , 2025. URL https://www.amazon.com/Kingston-DataTraveler-256GB-Performance-DTMAXA/dp/B0B57T5G5L/, accessed: 2025-05-12.

[81] Americas, W., "OpenIMU330BI," , 2025. URL https://eshop.wpgam.com/openimu330bi, accessed: 2025-05-12.

[82] Digi-Key, "PCB Builder," , 2025. URL https://www.digikey.com/en/pcb-builder/, accessed: 2025-05-12.

[83] DragonPlate, "0° Carbon Fiber Uni Sheet 18" x 24"," , 2025. URL https://dragonplate.com/0-degree-carbon-fiber-uni-sheet-18-x-24-x-24-copy, accessed: 2025-05-12.

[84] Hiwonder, "HPS-2027MG 20KG High Torque Waterproof Digital Servo," , 2024. URL https://www.hiwonder.com/products/hps-2027mg, accessed: 2025-05-14.

[85] Nanografi, "Nitinol Shape Memory Alloy Sheet 1mm Af 50-55°C," , 2025. URL https://nanografi.com/en/nitinol-shape-memory-alloy-sheet-1mm-af-50-55c/, accessed: 2025-05-12.

[86] Raymer, D. P., Aircraft Design: A Conceptual Approach, AIAA, 2018.

[87] Roskam, J., Airplane Design Part VI: Preliminary Calculation of Aerodynamic, Thrust and Power Characteristics, DARcorporation, 1987.

[88] GlobalSecurity.org, "AIM-9X Sidewinder," , 2025. URL https://www.globalsecurity.org/military/systems/munitions/aim-9x.htm, accessed: March 6, 2025.

[89] Nygaard, T. A., and Meakin, R. L., "An Aerodynamic Analysis of a Spinning Missile with Dithering Canards," , Jan 2001. URL https://ntrs.nasa.gov/api/citations/20030071145/downloads/20030071145.pdf, accessed on April 6, 2025.

[90] Larsen, W., "Fault Tree Analysis," Tech. rep., Picatinny Arsenal, 1974. URL https://apps.dtic.mil/sti/tr/pdf/AD0774843.pdf, fault tree construction methods, using the XM813 as an example.

Appendix A: Class I Engine Installations

Figure A.1 shows a general mock-up of the motor that will be used for this design. This is a size N model rocket motor with a diameter of 3.86 inches (98 mm) and a length of 41.2 inches (1046 mm). This motor is capable of producing up to 2,091 Newtons of thrust for 13.7 seconds. It should be noted that the final size may still be altered depending on final weight and size requirements.

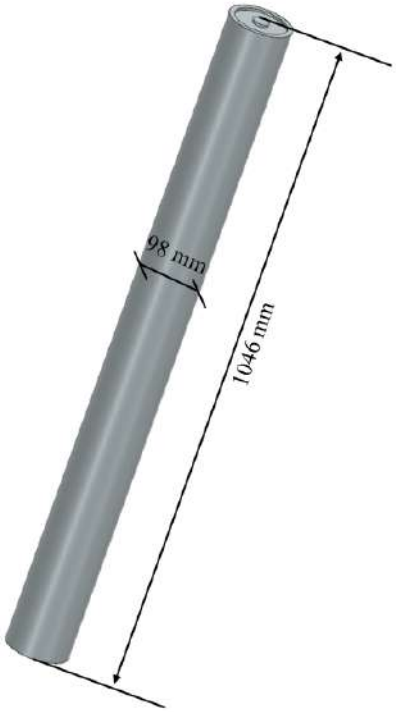

Fig. A.1 Proposed Model Rocket Motor

Appendix B: Class I Wing Layout Designs

Class I wing layout designs were done following the methods outlined in Fleeman's Tactical Missile Design, giving a start to wing, canard, and tail sizing. The sizing process takes into consideration the missile needing to achieve specified maneuverability and stability throughout its flight. The main focus is on maximizing aerodynamic efficiency while considering packaging and deployment constraints.

Per Fleeman's method, control surface areas were found in relation to missile reference dimensions. The following relations were used:

- Wing Area: $S_w \approx 0.1 \times S_{\text{ref}}$, where S_{ref} is based on missile length and diameter.

- Canard Area: $S_c \approx 0.03 \times S_{\text{ref}}$, adjusted upwards as needed for isoclinic design.
- Tail Fin Area: $S_f \approx 0.08 \times S_{\text{ref}}$, sized to ensure directional stability.

Based on a missile length of 9.15 ft and body diameter of 0.417 ft, the reference area is:

$$S_{\text{ref}} = \pi \times \left(\frac{0.417}{2}\right)^2 = 0.1365\,\text{ft}^2 \tag{56}$$

Using this value, initial estimates become:

$$S_w = 0.1 \times 0.1365 = 0.01365\,\text{ft}^2 \tag{57}$$

$$S_c = 0.03 \times 0.1365 = 0.004095\,\text{ft}^2 \tag{58}$$

$$S_f = 0.08 \times 0.1365 = 0.01092\,\text{ft}^2 \tag{59}$$

However, as noted below, these were adjusted for aerodynamic considerations. Given the high lift required for a rapid 180° turn and the use of isoclinic canards (which necessitate increased surface area for sufficient control authority), control surfaces were adjusted beyond Fleeman's minimums:

- Canard Area: Increased by 25% over initial estimate to accommodate isoclinic limitations:

$$S_c = 0.3135\,\text{ft}^2 \tag{60}$$

- Fin Area: Set to $0.8822\,\text{ft}^2$, consistent with stability requirements derived from AIM-9X scaling.
- Strake Area: Due to high maneuvering needs, strakes were added to augment lift and improve flow attachment. Area sized as 30% of fin area:

$$S_{\text{strake}} = 0.30 \times 0.8822 = 0.2647\,\text{ft}^2 \tag{61}$$

The final control surface dimensions for Class I design are presented in Table B.1.

Table B.1 Final Class I Control Surface Areas

Component	Area (ft^2)
Isoclinic Canard	0.3135
Tail Fin	0.8822
Strake (Each Side Total)	0.2647
Wing (Optional, if required)	0.01365 (initial estimate, subject to mission)

The wing area is dependent on mission-specific aerodynamic requirements.

Appendix C: Class I High Lift Device Sizing

This section outlines the aerodynamic modifications required for the proposed interceptor missile to achieve a high-g 180° turn for aft intercept of a low subsonic inbound target. The analysis includes calculations of the maximum required g-load, turn radius, and modifications to the control surfaces, including isoclinic canards, fins, and the addition of strakes.

The turn radius of the missile is determined by:

$$R = \frac{V^2}{g \cdot n} \tag{62}$$

where:

- $V = 2250$ ft/s (Mach 2),
- $g = 32.2$ ft/s^2 (gravitational acceleration),
- $n = 30$ (maximum load factor).

Substituting values:

$$R = \frac{2250^2}{30 \times 32.2} = \frac{5,062,500}{966} = 5240.68 \text{ ft} \tag{63}$$

The time required to complete the 180° turn is given by:

$$t = \frac{\pi R}{V} \tag{64}$$

$$t = \frac{\pi \times 5240.68}{2250} = 7.317 \text{ s} \tag{65}$$

Isoclinic canards rotate together which reduces control authority compared to traditional canards. To compensate, an additional 25% increase in canard area and span is applied.

The proposed missile has a length of:

$$L_{\text{proposed}} = 9.15 \text{ ft}, \quad L_{\text{orininal}} = 9.9 \text{ ft} \tag{66}$$

$$SF = \frac{L_{\text{proposed}}}{L_{\text{original}}} = \frac{9.15}{9.9} = 0.924 \tag{67}$$

A 15% increase for maneuverability is applied:

$$SF_{\text{adjusted}} = SF \times 1.15 \tag{68}$$

For isoclinic canards, a further 25% increase is included:

$$SF_{\text{isoclinic}} = SF_{\text{adjusted}} \times 1.25 \tag{69}$$

Isoclinic Canard Area:

$$A_{\text{canard,new}} = A_{\text{canard,original}} \times SF_{\text{isoclinic}} \tag{70}$$

$$A_{\text{canard,new}} = 0.236 \times 0.924 \times 1.15 \times 1.25 = 0.3135 \text{ ft}^2 \tag{71}$$

Isoclinic Canard Span:

$$S_{\text{canard,new}} = S_{\text{canard,original}} \times SF_{\text{isoclinic}} \tag{72}$$

$$S_{\text{canard,new}} = 1.98 \times 0.924 \times 1.15 \times 1.25 = 2.6306 \text{ ft} \tag{73}$$

Fin Area:

$$A_{\text{fin,new}} = A_{\text{fin,original}} \times SF_{\text{adjusted}} \tag{74}$$

$$A_{\text{fin,new}} = 0.830 \times 0.924 \times 1.15 = 0.8822 \text{ ft}^2 \tag{75}$$

Fin Span:

$$S_{\text{fin,new}} = S_{\text{fin,original}} \times SF_{\text{adjusted}} \tag{76}$$

$$S_{\text{fin,new}} = 1.44 \times 0.924 \times 1.15 = 1.530 \text{ ft} \tag{77}$$

Since isoclinic canards provide less lift contribution, strakes are added to enhance stability. The strake area is increased to 30% of the fin area:

$$A_{\text{strake}} = 0.30 \times A_{\text{fin,new}} \tag{78}$$

$$A_{\text{strake}} = 0.30 \times 0.8822 = 0.2647 \text{ ft}^2 \tag{79}$$

The updated control surface dimensions ensure that the missile can execute the required 180° turn while maintaining stability with isoclinic canards. The final adjusted values are summarized in Table C.1.

Table C.1 Final Adjusted Control Surface Sizing with Isoclinic Canards

Parameter	Updated Value
Turn Radius	5240.68 ft
Turn Time	7.317 s
New Isoclinic Canard Area	0.3135 ft^2
New Isoclinic Canard Span	2.6306 ft
New Fin Area	0.8822 ft^2
New Fin Span	1.530 ft
Added Strake Area	0.2647 ft^2

These modifications ensure optimal control authority and aerodynamic efficiency under the new configuration.

Appendix D: Class I Empennage Design

The empennage was designed to provide stability and full flight control. To ensure the design aligns mission specifications, the canard and tail volume coefficients were matched to those of the AIM-9X missile.

The canard volume coefficient, V_c, and tail volume coefficient, V_t, were computed using the geometric properties and positioning of the control surfaces, based on the following definitions [86] [87]:

$$V_c = \frac{S_c \cdot l_c}{S_{ref} \cdot c_{ref}} \tag{80}$$

$$V_t = \frac{S_t \cdot l_t}{S_{ref} \cdot c_{ref}} \tag{81}$$

Where:

- S_c = Canard planform area
- l_c = Distance from canard aerodynamic center to missile center of gravity
- S_t = Tail planform area
- l_t = Distance from tail aerodynamic center to missile center of gravity
- S_{ref} = Reference cross-sectional area of the missile body
- c_{ref} = Reference length (missile body length)

The values were then calculated as follows:

$$S_{ref} = \pi \left(\frac{5}{24} \right)^2 = 0.1365 \text{ ft}^2$$

$$l_c = 0.25 \cdot 9.15 \text{ ft} = 2.29 \text{ ft}$$

$$l_t = 0.85 \cdot 9.15 = 7.78 \text{ ft}$$

$$V_c = \frac{0.218 \cdot 2.29}{0.1365 \cdot 9.15} = 0.406$$

$$V_t = \frac{0.767 \cdot 7.78}{0.1365 \cdot 9.15} = 4.70$$

These values closely match the volume coefficients derived for the AIM-9X [88], thus, this design achieves similar stability margins and control authority. This ensures the missile is capable of predictable, stable flight dynamics within the flight envelope.

The final sizing of the empennage components were directly scaled from AIM-9X geometry. This method leverages the control performance, while highlighting compatibility with the constrained form factor associated with the SeaRAM launcher.

Table D.1 Empennage Layout and Sizing

Surface	Area (ft^2)	Span (ft)	Location (% length)
Canards	0.218	1.83	25%
Fins (Tail)	0.767	1.33	85%

The concept of the empennage design can be seen visually below, in figure D.1.

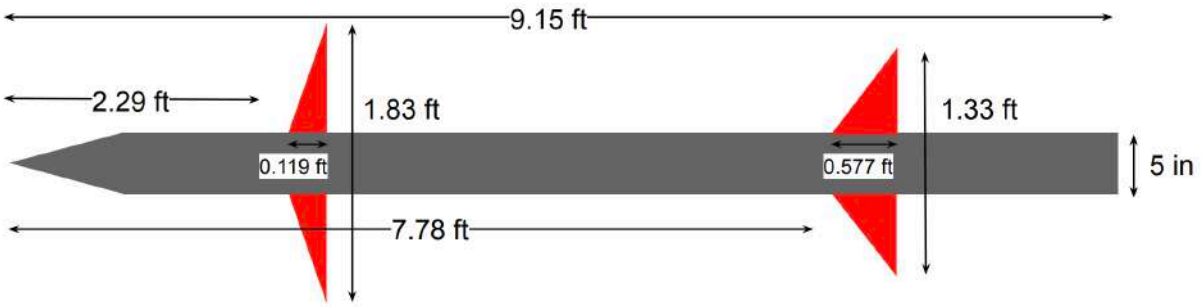

Fig. D.1 Class I Empennage Design Concept

Appendix E: Class I Launcher Layout

The launcher will use modular, hermetically sealed launch tubes that are able to be towed by a trailer. The use of launch tubes will allow for quick reload of expended missiles onto the launch platform. Additionally, it lessens environmental deterioration and will be able to charge the systems within the missile.

Appendix F: Weight and Balance Analysis

To find the weight and balance of the missile at both stages, the amateur rocket building software OpenRocket was used. This allowed for rapid determination of the center of gravity and aerodynamic center as the missile's design is iterated. With the first stage, the AeroTech M1419W motor is used to propel it, and a tertiary set of fins is necessary to stabilize this stage. All fins are comprised of 30 mm aluminum plate, while the body is made of 15 mm carbon fiber tubing. Figure F.1 displays the center of gravity (as a blue checkered circle) and pressure (as the red circle) at 0.3 Mach. Figure F.2 displays the the CG and AC at Mach 2. The location of the CG with the motor at full mass was 48 inches from the nose. The AC, in the subsonic state, is 47 inches from the nose, and 62 inches in supersonic flight. Also note that a payload of six kilograms was determined to be optimal for stability and maximum altitude.

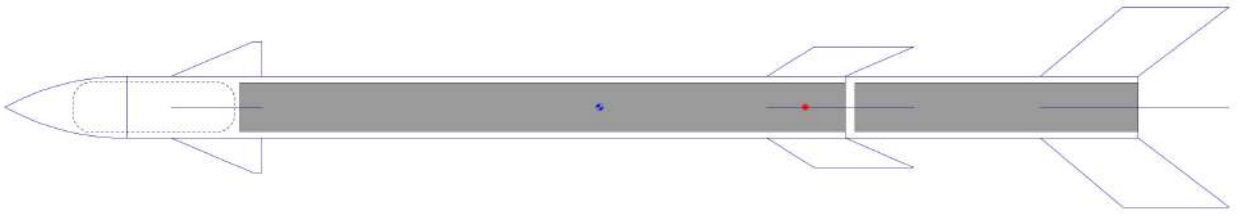

Fig. F.1 First Stage Subsonic Weight and Balance Analysis

Fig. F.2 First Stage Supersonic Weight and Balance Analysis

The second stage weight and balance followed the same process as the first stage. Figure F.3 shows the subsonic weight and balance of the second stage, while Figure F.4 shows it at Mach 2. The CG with the unfired rocket is 35 inches from the nose. The subsonic AC is 29 inches from the nose and 35 inches away in the supersonic flight regime.

Fig. F.3 Second Stage Subsonic Weight and Balance Analysis

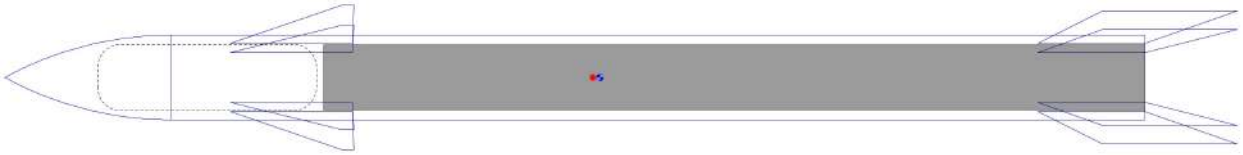

Fig. F.4 Second Stage Supersonic Weight and Balance Analysis

With this data and the calculated empty weights of the missile's stages, the weight-CG excursion diagram shown below in Figure F.5 was generated.

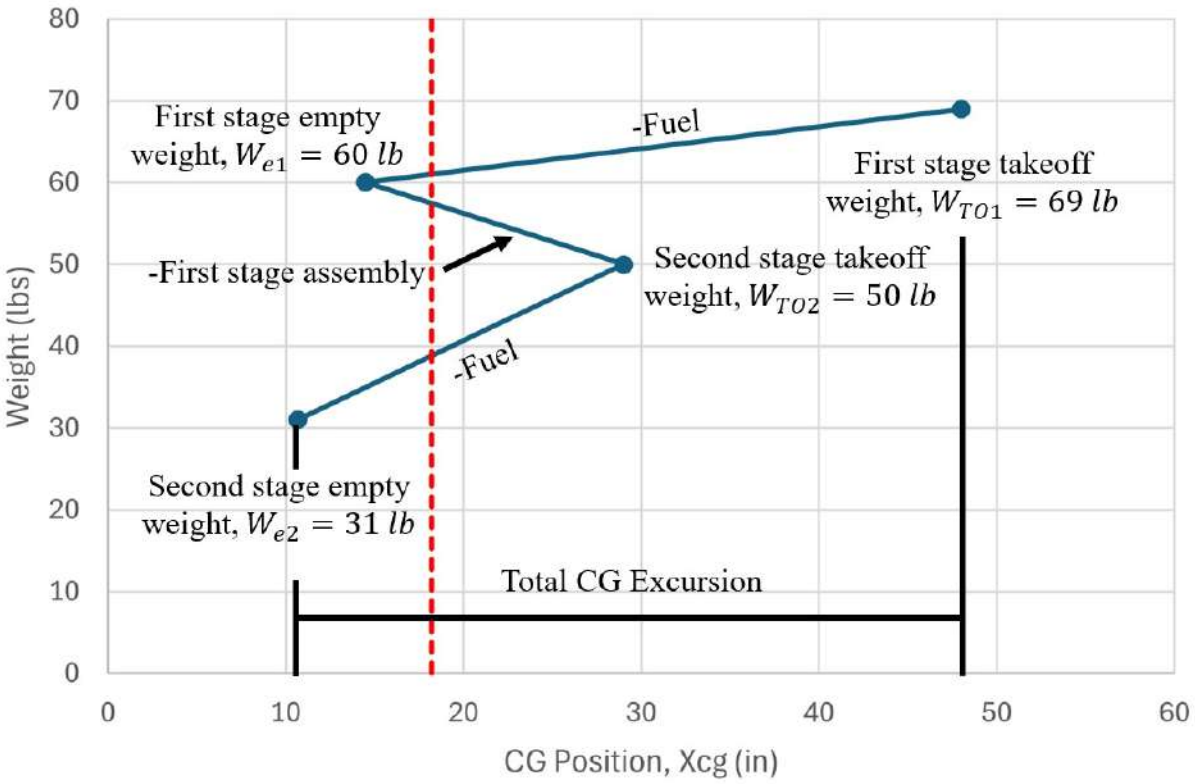

Fig. F.5 Weight-CG Excursion Diagram

Appendix G: Class 1 Drag Polar and Performance Analysis

Supersonic Flight Conditions

The class I drag polar analysis began by finding the wetted area of each component of the missile as well as the total wetted area. The following equations were used to determine wetted area.

- Fuselage wetted area: $A_{\text{fuselage}} = 2\pi rL = 10.734\,\text{ft}^2$
- Ogive nose wetted area: $A_{\text{nose}} \approx \pi r L_n \left(1 \frac{0.35r}{L_n}\right) = 6.039\,\text{ft}^2$
- Canards wetted area: $A_{\text{canards}} = NC_r\, C_t b = 1.233\,\text{ft}^2$
- Wing wetted area: $A_{\text{wings}} = NC_r\, C_t b = 1.874\,\text{ft}^2$
- Tail wetted area: $A_{\text{tail}} = NC_r\, C_t b = 5.089\,\text{ft}^2$
- Total wetted area: $A_{\text{wet}} = A_f\, A_n\, A_c\, A_w\, A_t = 24.97\,\text{ft}^2$

By determining these values, a bigger picture of the fuselage shape can be drawn. This is represented in the fuselage perimeter graph shown in G.1 below.

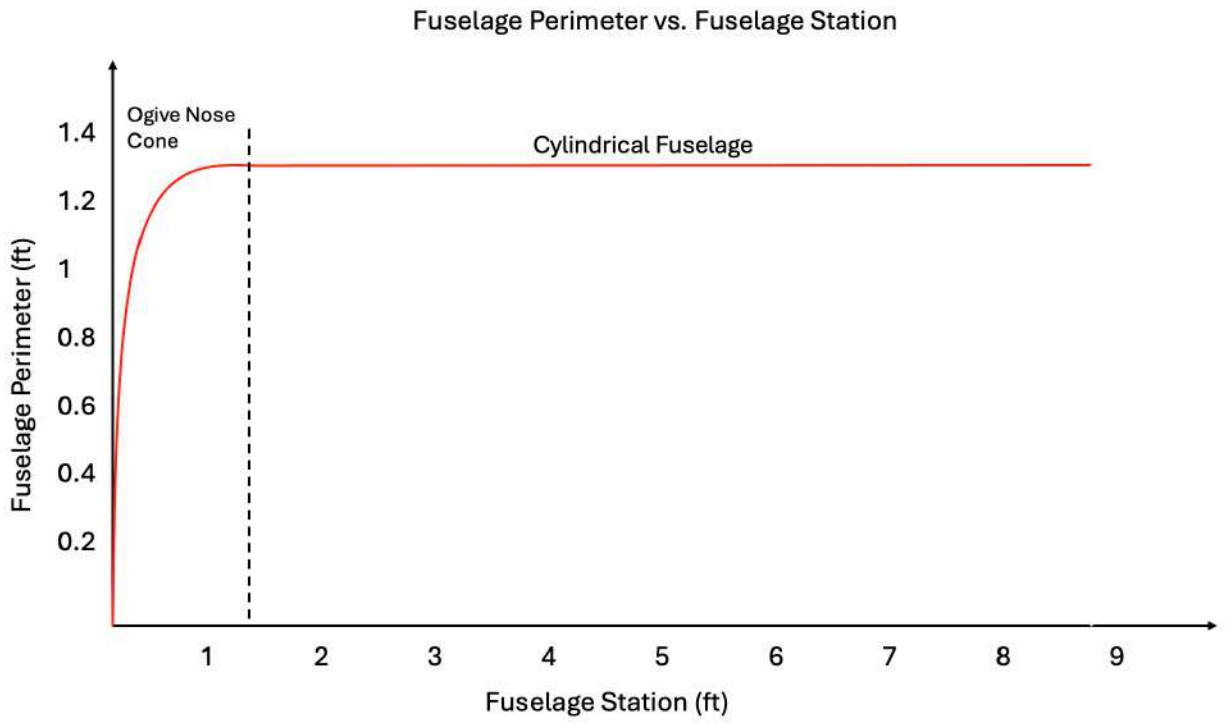

Fig. G.1 Perimeter Plot of Fuselage Cross Sections

Given the simple geometry of the missile, the fuselage perimeter plot is constant after the ogive nose cone section.

The next step was to determine the parasite area. This was performed by analyzing figure 3.21 of [57]. Due to this logarithmic graph being centered around planforms with larger wetted areas than the MachHawks missile, extrapolation was needed. This extrapolation was performed in MATLAB and can be found in figure G.2 below.

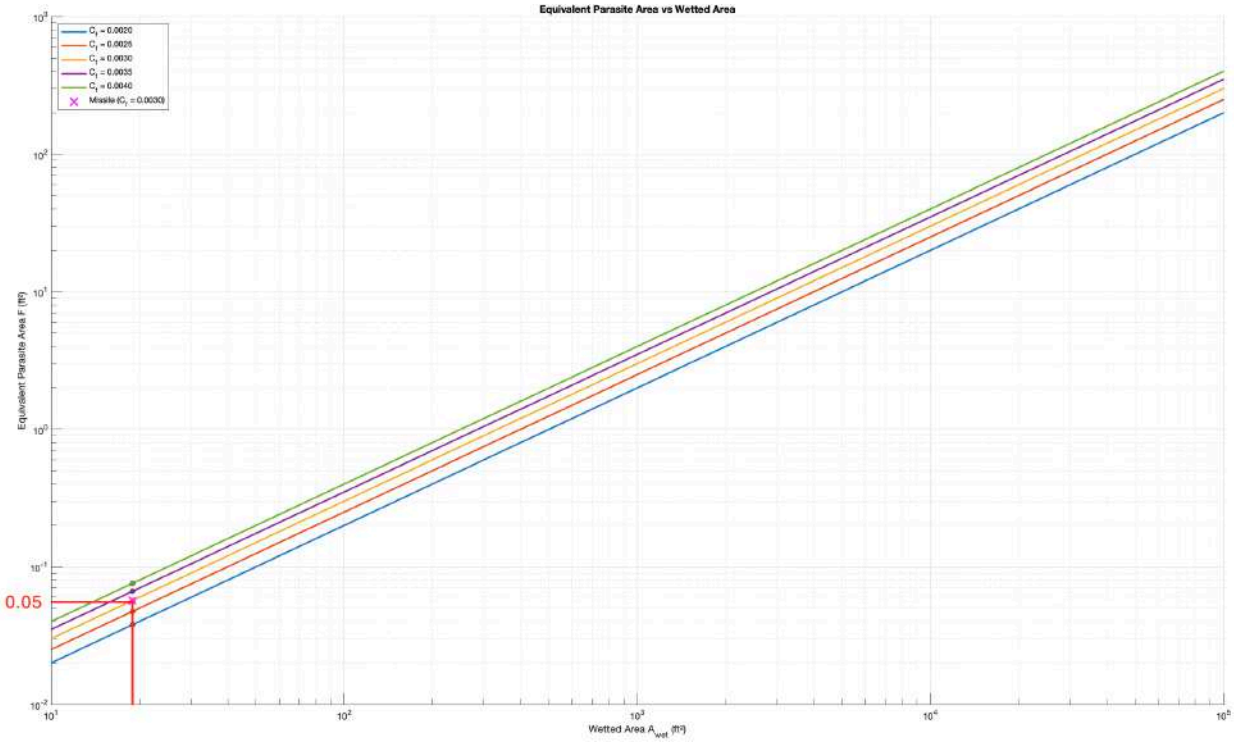

Fig. G.2 Parasite Area Extrapolation

- Parasite area: $f = 0.05\,\text{ft}^2$
- Reference area (missile cross-section): $S = \frac{\pi D^2}{4} = 0.1364\,\text{ft}^2$
- Clean zero-lift drag coefficient: $C_{D_0} = \frac{f}{S} = \frac{0.0749}{0.1364} = 0.5493$

The compressibility drag rise was then determined.

- Compressibility drag increment at Mach 2: $\Delta C_{D_0} = 0.0710$
- Total zero-lift drag coefficient: $C_{D_0,\text{total}} = C_{D_0}\ \Delta C_{D_0} = 0.5493\ 0.0710 = 0.6203$

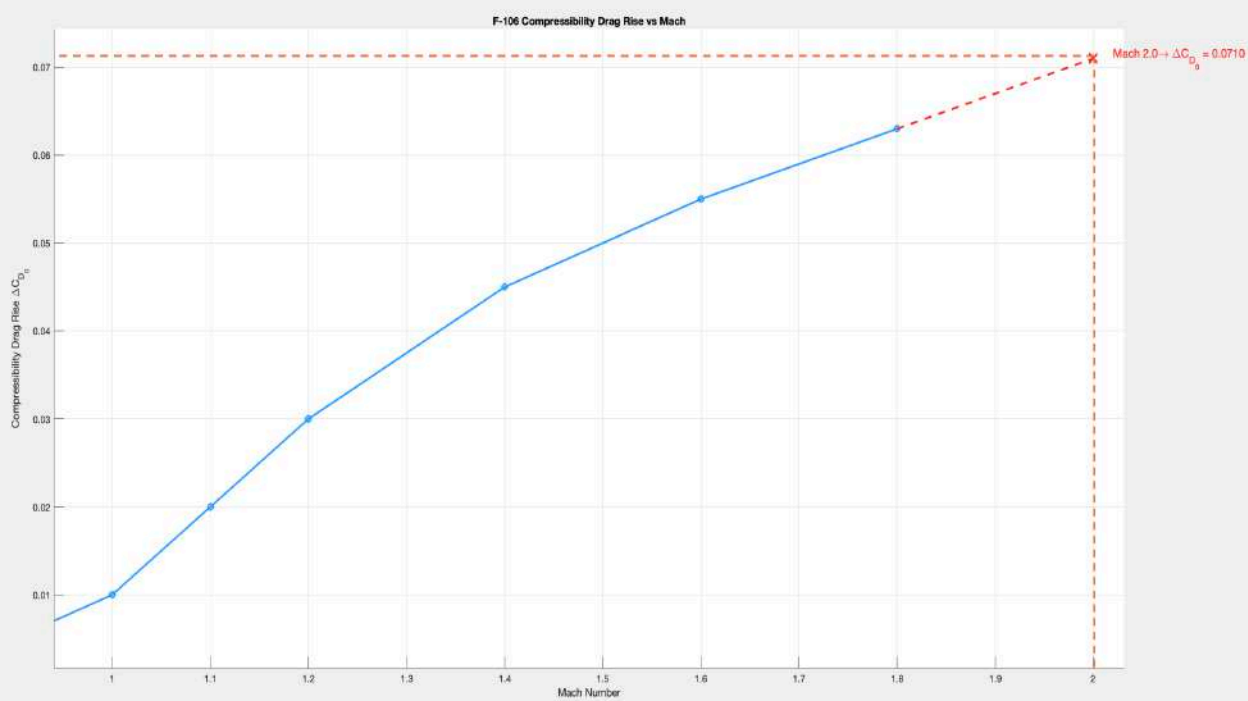

Fig. G.3 Supersonic Compressibility Drag Rise

The missile's drag polar is modeled using the standard parabolic form:

$$C_D = C_{D_0}\ kC_L^2 \tag{G.1}$$

where C_D is the total drag coefficient, C_{D_0} is the zero-lift drag coefficient, k is the induced drag factor, and C_L is the lift coefficient.

Since the missile operates at Mach 2, a compressibility drag rise is added to the clean zero-lift drag coefficient:

$$C_{D_0,\text{clean}} = C_{D_0,\text{basic}}\ \Delta C_{D_0,\text{compressibility}} = 0.5493\ 0.071 = 0.6203 \tag{G.2}$$

The induced drag factor k is computed using the standard subsonic formula:

$$k = \frac{1}{\pi e AR} \tag{G.3}$$

Using the missile wing geometry, the span and planform area give:

$$AR = \frac{b^2}{S} = \frac{0.392^2}{0.233} = 0.659 \tag{G.4}$$

The Oswald efficiency factor e varies by configuration:

- Clean: $e = 0.82$
- Takeoff: $e = 0.77$
- Landing: $e = 0.72$

For the clean configuration:

$$k = \frac{1}{\pi \cdot 0.82 \cdot 0.659} = 0.588$$

$$C_D = 0.6203\ 0.588 C_L^2$$

For the takeoff configuration, we assume $\Delta C_{D_0} = 0.035$:

$$C_{D_0,\text{takeoff}} = 0.6203\ 0.035 = 0.6553$$

$$k = \frac{1}{\pi \cdot 0.77 \cdot 0.659} = 0.627$$

$$C_D = 0.6553\ 0.627 C_L^2$$

For the landing configuration, we assume $\Delta C_{D_0} = 0.085$:

$$C_{D_0,\text{landing}} = 0.6203\ 0.085 = 0.7053$$

$$k = \frac{1}{\pi \cdot 0.72 \cdot 0.659} = 0.669$$

$$C_D = 0.7053\ 0.669 C_L^2$$

The standard induced drag model assumes subsonic flow. At Mach 2, this approximation becomes less accurate due to compressibility and wave drag effects. However, it is retained here to maintain consistency with the Class I drag estimation method.

The maximum lift-to-drag ratio for each configuration is computed using:

$$\left(\frac{L}{D}\right)_{\max} = \frac{1}{2\sqrt{C_{D_0} \cdot k}} \tag{G.5}$$

For the clean configuration:

$$\left(\frac{L}{D}\right)_{\max} = \frac{1}{2\sqrt{0.6203 \cdot 0.588}} = 0.827$$

For the takeoff configuration:

$$\left(\frac{L}{D}\right)_{\max} = \frac{1}{2\sqrt{0.6553 \cdot 0.627}} = 0.787$$

For the landing configuration:

$$\left(\frac{L}{D}\right)_{\max} = \frac{1}{2\sqrt{0.7053 \cdot 0.669}} = 0.750$$

Table G.1 Drag Polar Parameters and Maximum Lift-to-Drag Ratios at Mach 2

Configuration	C_{D_0}	k	Drag Polar Equation	$LD_{\max}$
Clean	0.6203	0.588	$C_D = 0.6203\ 0.588 C_L^2$	0.827
Takeoff	0.6553	0.627	$C_D = 0.6553\ 0.627 C_L^2$	0.787
Landing	0.7053	0.669	$C_D = 0.7053\ 0.669 C_L^2$	0.750

Subsonic Flight Conditions

The differences in drag behavior between subsonic and supersonic conditions are primarily due to compressibility effects, shock wave formation, and flow separation. In the subsonic condition, airflow is incompressible or weakly compressible, and the drag rise due to compressibility is small. Due to this, C_{D_0} remains low and the drag polar is mainly effected by skin friction and form drag. The induced drag factor k, remains consistent across both conditions but has more of an effect at lower speeds because lift generation requires higher angles of attack. At supersonic speeds, wave drag and strong compressibility effects C_{D_0}. This is seen by ΔC_{D_0} which shows the added drag due to shock formation on the body and control surfaces. For example, at Mach 2, the compressibility increment is estimated at 0.071, but it is only 0.0028 at Mach 0.2. The total drag at zero lift is higher in the supersonic condition. Also, $LD_{\max}$ is lower at supersonic speeds, which shows the effects of wave drag and lower lift.

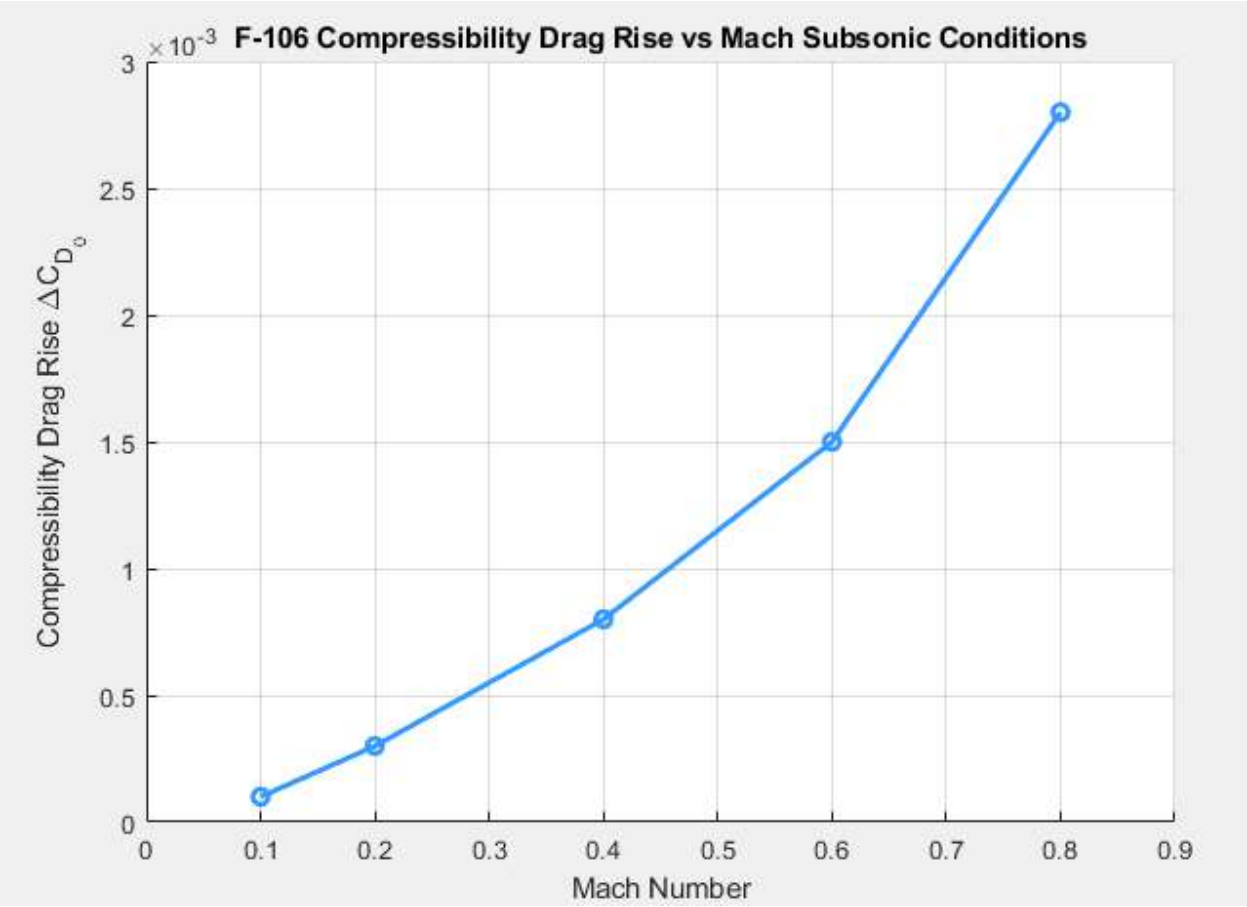

Fig. G.4 Subsonic Compressibility Drag Rise

The missile's drag polar is modeled using the standard parabolic form:

$$C_D = C_{D_0}\ kC_L^2 \tag{G.6}$$

where C_D is the total drag coefficient, C_{D_0} is the zero-lift drag coefficient, k is the induced drag factor, and C_L is the lift coefficient.

At subsonic speeds, a small compressibility drag rise is added to the basic zero-lift drag coefficient. For Mach 0.8, this increment is estimated as:

$$C_{D_0,\text{clean}} = C_{D_0,\text{basic}}\ \Delta C_{D_0,\text{compressibility}} = 0.5493\ 0.0028 = 0.5521 \tag{G.7}$$

The induced drag factor k is computed using the standard subsonic expression:

$$k = \frac{1}{\pi e AR} \tag{G.8}$$

Using the missile's wing geometry, the aspect ratio is calculated as:

$$AR = \frac{b^2}{S} = \frac{0.392^2}{0.233} = 0.659$$

The Oswald efficiency factor e depends on configuration:

- Clean: $e = 0.82$
- Takeoff: $e = 0.77$
- Landing: $e = 0.72$

For the clean configuration:

$$k = \frac{1}{\pi \cdot 0.82 \cdot 0.659} = 0.588, \quad C_D = 0.5521\ 0.588C_L^2$$

For the takeoff configuration, with $\Delta C_{D_0} = 0.035$:

$$C_{D_0,\text{takeoff}} = 0.5521\ 0.035 = 0.5871, \quad k = \frac{1}{\pi \cdot 0.77 \cdot 0.659} = 0.627$$

$$C_D = 0.5871\ 0.627C_L^2$$

For the landing configuration, with $\Delta C_{D_0} = 0.085$:

$$C_{D_0,\text{landing}} = 0.5521\ 0.085 = 0.6371, \quad k = \frac{1}{\pi \cdot 0.72 \cdot 0.659} = 0.669$$

$$C_D = 0.6371\ 0.669C_L^2$$

The maximum lift-to-drag ratio for each configuration is given by:

$$\left(\frac{L}{D}\right)_{\max} = \frac{1}{2\sqrt{C_{D_0} \cdot k}} \tag{G.9}$$

For the clean configuration:

$$\left(\frac{L}{D}\right)_{\max} = \frac{1}{2\sqrt{0.5521 \cdot 0.588}} = 0.468$$

For the takeoff configuration:

$$\left(\frac{L}{D}\right)_{\max} = \frac{1}{2\sqrt{0.5871 \cdot 0.627}} = 0.446$$

For the landing configuration:

$$\left(\frac{L}{D}\right)_{\max} = \frac{1}{2\sqrt{0.6371 \cdot 0.669}} = 0.438$$

Table G.2 Drag Polar Parameters and Maximum Lift-to-Drag Ratios at Mach 0.8

Configuration	C_{D_0}	k	Drag Polar Equation	$LD_{\max}$
Clean	0.5521	0.588	$C_D = 0.5521\ 0.588C_L^2$	0.468
Takeoff	0.5871	0.627	$C_D = 0.5871\ 0.627C_L^2$	0.446
Landing	0.6371	0.669	$C_D = 0.6371\ 0.669C_L^2$	0.438

Appendix H: Analysis of Weight and Balance, Stability and Control and L/D Results and Iterations

The objective of this section is to analyze the values determined of the stability of the missile. Below, a list was created to guide the analysis of different characteristics previously calculated.

i. Examine and List Levels of Directional and Longitudinal Static Margin Available in Current Aircraft Design.

The static margin of the missile was determined by an aerodynamic center and center of gravity analysis. The calculated value was 24 percent. This indicates the missile has a very stable configuration. However, the goal was to obtain a static margin of around 10 percent. In order to reduce the calculated value, a longitudinal x-plot was used to vary horizontal tail area. This showed that a horizontal-wing area ratio of 1.15 obtains a static margin of 10.6 percent, which balances both stability and maneuverability.

ii. Examine and List Amount of Directional Control Authority and Rudder Deflections Required during Most Adverse Engine-Out Occurrences.

This missile is symmetric with no asymmetrically mounted engines. Thus, there are no engine-out conditions. However, if thrust vectoring is included in the configuration, vertical tail sizing and rudder control would require that further analysis needs to be performed to to ensure the deflection doesn't exceed the 25 degree limit.

iii. Examine and List Levels of CG Excursion and Effects on Static Margin and Trim Drag.

The OpenRocket software was used to determine the center of gravity in both subsonic and supersonic flight conditions. It was necessary to calculate it in both flight conditions due to the munk shift effect which moves the aerodynamic center aft from the original position when supersonic speeds are reached. The center of gravity for the first stage shifts from 46 inches to further aft as fuel burns. Despite these excursions, the

static margin remains positive throughout, ensuring stability. The aerodynamic center's movement from 58.3 inches (subsonic) to 48.4 inches (supersonic) also supports stability during the full flight envelope. Trim drag effects were minimal due to this balanced configuration.

iv. Examine and List Old and New L/D Conditions for Aircraft, noting Any Changes in Aircraft Sizing WRT Original Estimates.

Table H.1 Updated Lift-to-Drag Ratio for Various Flight Configurations

Configuration	Maximum LD
Clean	0.468
Takeoff	0.446
Landing	0.438

There was no secondary sizing analysis required due to the above values being consistent with the initial values. All of the updated lift-to-drag ratios remained in a 5 percent margin of the initial values.

v. Determine whether or not heavy, permanent items can be moved and/or the wing can be repositioned or swept to accommodate static margin and CG excursion needs, then do it if possible. Otherwise, start over again with a new configuration.

After evaluating, it was found that shifting major components, such as the payload or battery modules, would not offer significant advantages over the current layout. Additionally, wing repositioning was not necessary due to the achievable tail sizing adjustment that brought the static margin within acceptable range without excess trim drag.

vi. Determine whether or not the vertical tail or other counter-yawing moment device is sufficient to handle engine-out conditions with less than 25°of rudder deflection. If not, resize vertical tail or other devices.

The vertical tail, acting through the bottom fins, was determined to offer sufficient counter-yawing moment. With the aircraft's symmetry and lack of asymmetrical thrust events, rudder deflection is kept under 25° by design. If a future iteration introduces thrust offset, the vertical tail will need reevaluation using Equation L.11 for C_{n_β} calculations.

vii. Determine whether or not the changes in L/D and corresponding increases or decreases in fuel burn lead to a greater than 5 percent change in Wto estimate. If less than, keep design, resize items incrementally.

If greater, and design changes are impossible, start over with new configuration and/or initial assumptions.

With changes in L/D below the 5 percent threshold, fuel burn remained within predicted margins. The takeoff weight estimate of 200 lbs and fuel mass of 110.28 lbs are retained, as verified through consistency with the AIM-9X and SeaRAM analogs. No redesign or re-estimation was necessary.

Appendix I: Class 1 Layout of Major Systems

Launch System

The launch system will need two configurations for land-based and naval use. The former will closely resemble a National Advanced Surface-to-Air Missile Systems (NASAMS) launcher. Each canister will have a rolling sled with launch rail (similar to that shown in Fig.J.1 that the missile will connect to, and an integral system to power the missile's batteries with an inductive charging unit. This will allow for a better sealed missile that will be more resistant to deterioration and speed up reload time. Each canister will be able to be loaded ahead of time and mounted to the launcher system with an array of six missiles. It will also be able to slew to the bearing of a threat to fire the missile and have an outlet for external power from an external source. The launcher system will be light enough to be towed by a Humvee, which has a towing weight of approximately 4,000 lbs. To deploy the system, it will be detached from the Humvee or other vehicle, plant stabilizing legs, and be connected to an external power source such as a generator. Once a missile has been expended, the old canister will simply be removed from the frame by two or more soldiers, and a fresh canister slid into place. Additional canisters would be carried by other vehicles.

Fig. J.1 View of missile "sleds" on NASAMS canisters [10]

The naval variant of the missile will utilize the existing Phalanx Block II launchers or VLS cells, being approximately the same form factor as a SeaRAM. This will allow for the use of existing launcher systems, only taking valuable VLS cell space if the mission necessitates many interceptors.

Flight Control Systems

The missile utilizes a canard-controlled rolling airframe configuration, inspired by aerodynamic analysis and control methodologies demonstrated in rolling missile systems like the FM-3. This missile design was chosen based on capability for using infrared guidance, agility, and compatibility with synthetic aperture IR sensing, which relies on predictable missile rotation.

The control system is built around the canards combined with a passive roll induced by tail fins. The FM-3 analysis describes that "directional control is actuated via canard dithering," where "the canard pitch position follows an actuator signal with constant pitch rate" [89] as the missile rolls. This approach allows three-dimensional directional control using only two canards by exploiting roll-induced symmetry. The flight control system maintains missile orientation and applies maneuver commands via a control actuation loop. The actuation sequence aligns with the FM-3's, where the actuator signal "flip-flops between +/- 1 according to the sign of the sum of two sine-waves called the command and dither signals"[89].

Our missile system will use electromechanical actuators (EMAs) for both the canards and fins. These were chosen for their low power requirements and COTS availability which will aid in meeting the cost target. The actuators are placed entirely within the second stage, which remains after booster separation. This makes sure there is full control authority during terminal homing. The simulation results for the FM-3 missile showed that canard effectiveness changes with roll angle, and that "the direct contribution of the canards to instantaneous normal force dominate all other sources"[89]. These results emphasize the validity our choice of a rolling airframe configuration and the focus on canard induced maneuvering.

The flight control computer uses a simplified PID controller optimized for real time with little lag control. The system operates autonomously after launching and has no dependence on uplink updates unless specified. All critical flight control logic, sensors, and actuators are placed in the second stage, forward of place of the stage separation. This makes sure there us uninterrupted operation throughout flight.

Rocket Motor Performance and Characteristics

The two motors selected are the AeroTech M1419 for the first stage, and the Cesaroni N5800 for the second stage. Both motors have published thrust curves from their manufacturers, which are shown below in Figures J.2 and J.3, respectively. Both have extremely high impulses, with the M1419 firing for about 7 seconds, while the N800 fires for under 4 seconds.

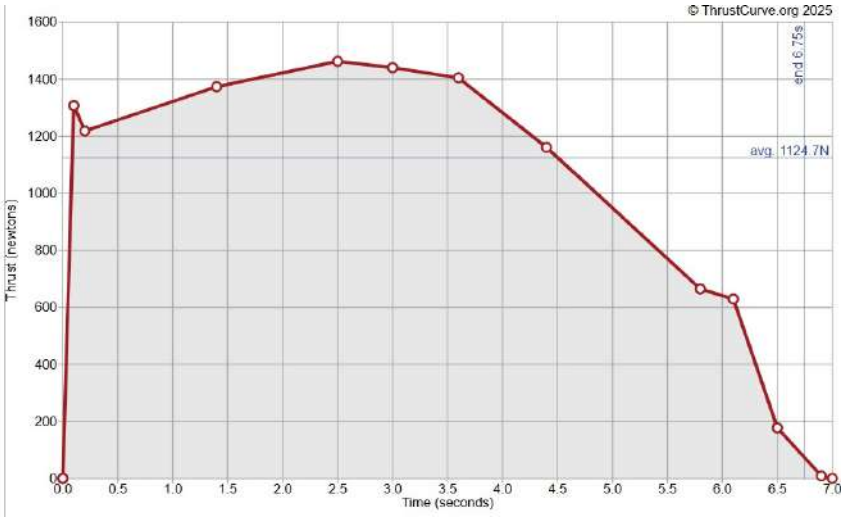

Fig. J.2 AeroTech M1419 rocket thrust curve [11]

Fig. J.3 Cesaroni N5800 rocket thrust curve [12]

Additional characteristics of the M1419 and N5800 are shown below in tables J.1 and J.2, respectively.

Table J.1 M1419 Rocket Characteristics[11]

Parameter	Value
Length	579 mm (22.8 in)
Diameter	98 mm (3.86 in)
Propellant Weight	6920 g (15.2 lbs)
Burn Time	7.1 s
Total Impulse	7760 N-s (1740 lbf-s)

Table J.2 N5800 Rocket Characteristics [12]

Parameter	Value
Length	1239 mm (48.8 in)
Diameter	98 mm (3.86 in)
Propellant Weight	14826 g (32.7 lbs)
Burn Time	3.5 s
Total Impulse	7760 N-s (4522 lbf-s)

Electrical System

The electrical system of the missile has been designed to support low-cost, high-reliability operation while still meeting mission specifications. The power is supplied by a thermal battery, which is activated at launch. These batteries are compact and they are often used in missiles because of their long life expectancy and instant-on capability. The battery will power all onboard subsystems, such as the flight computer, seeker sensors, actuators, and telemetry hardware.

A central flight computer manages signal processing and control logic. This unit links with the synthetic aperture IR seeker, actuator control loops, and external command data links. Due to the compact size and cost requirements of the missile, a single-board computer with embedded digital signal processing (DSP) is employed. Signal integrity is maintained through protected wiring and adherence to military standard electrical and EMI standards.

The missile's sensors, infrared cameras mounted on the canards, need stable quiet power, which is met through onboard DC-DC converters. Power managing circuitry makes sure that aspects like control actuators and guidance, which prove to be a high priority, keep powered even under partial system failure. The electrical system includes an arming circuit for the warhead which is away from from the main control logic and only enabled post-launch when flight conditions are met. This makes operational safety higher and lowers the chance of early detonation. Figure J.4 shows the side view and Figure J.5 shows the front view layout of the electrical system as will be integrated to the missile design.

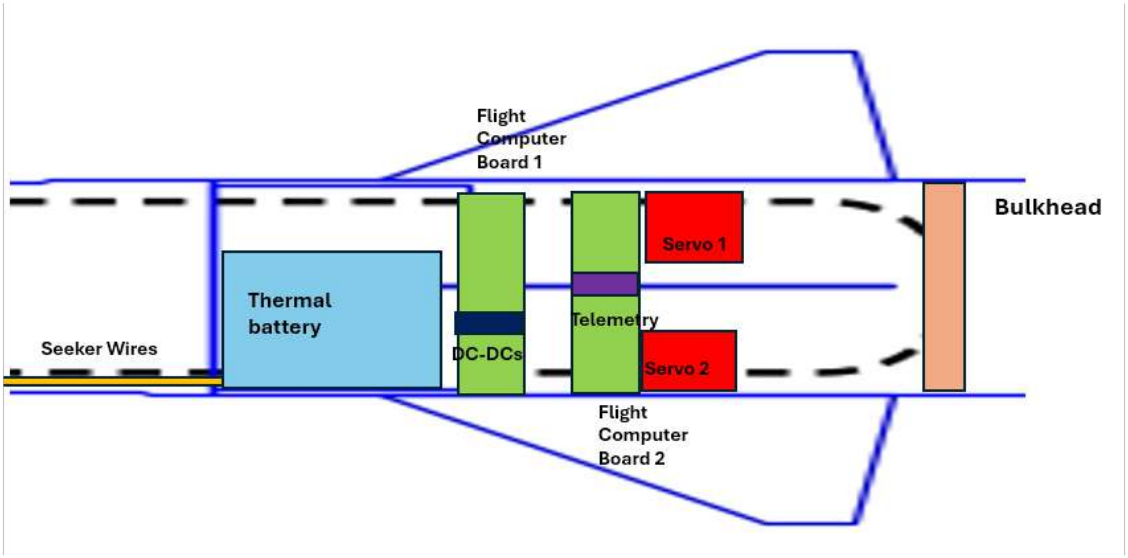

Fig. J.4 Electronic System Sizing Side View

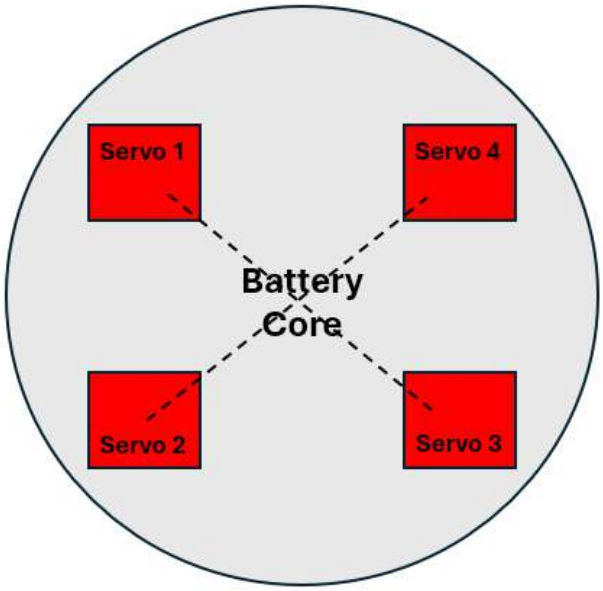

Fig. J.5 Electronic System Sizing Front View

To support interoperability with existing launcher infrastructure, the electrical interface includes a universal connector port compatible with SeaRAM and fixed ground launchers. The allows for future upgrades to the guidance package or data links without major redesign.

The wiring diagram in Figure J.6 shows how each component in the above system should be wired to work in conjunction with each other. The DC-DC units sit between the battery and each power bus for stable voltage regulation. All wires should use shielded cables to meet EMI standards. There should be four

data lines from the flight computer to correspond with each of the servos getting their own power input. The location and wire specifications are as following: the seeker will be require internal cabling routed through sealed conduit, the sensors will use twisted-pair shielded cables through wing struts. In addition to what is listed, the team tentatively has planned to use five cushion sensors mounted around the missile body to detect launch. If the team proceeds with this, they will receive power from Bus D and their signal output to the flight computer will require a digital pulse per sensor indicating the trigger state, they can be polled at 10 ms intervals for redundancy.

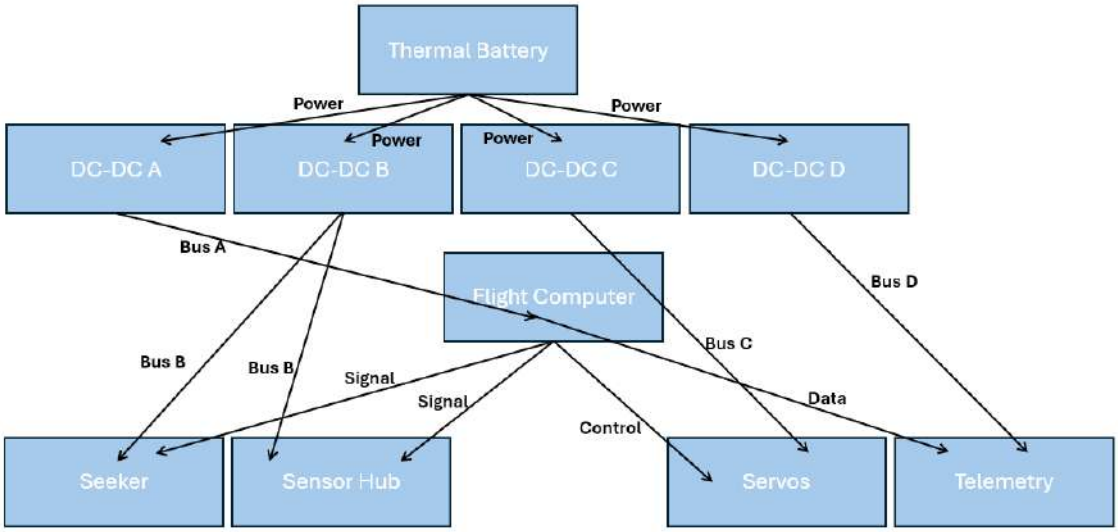

Fig. J.6 Wiring Diagram for Internal Electronic System

Appendix J: Class 1 Structural Layout

This section outlines the substructure of the proposed missile design. Ring frames were placed according to the location of the two motors in the sustainer and in the stage. A ring frame holds the motor in place at the front and back end of the motor. The sustainer motor is also held in place by an additional ring frame in the middle due to its length. A deflagration line is placed on the body between the two stages to initiate staging. Figure J.1 shows the structural components of the proposed design.

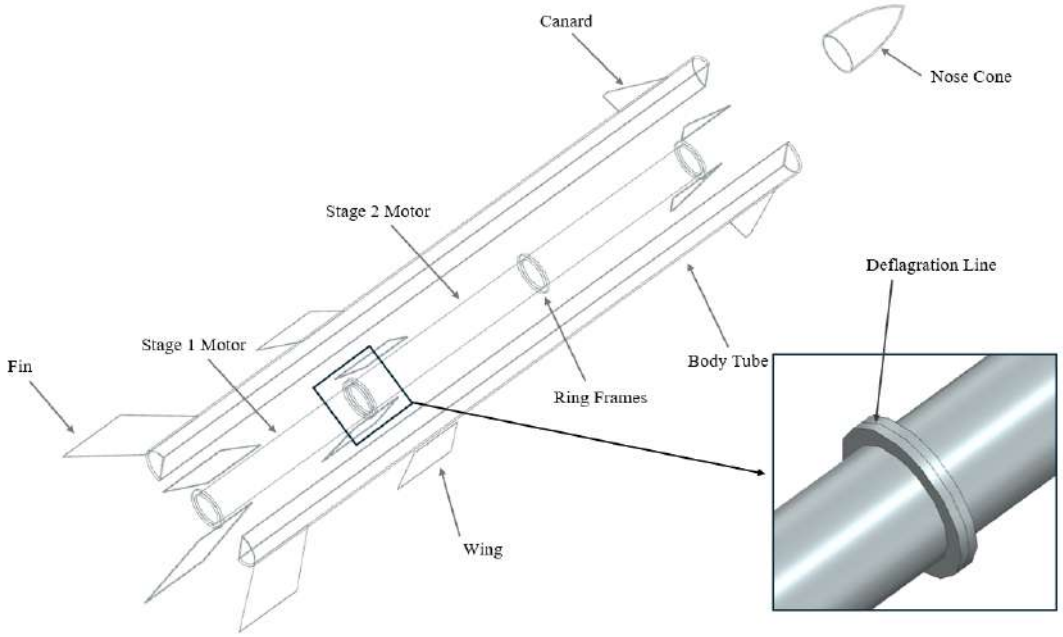

Fig. J.1 Explosion View of Structural Components

Appendix K: Fault Tree Analysis

To construct the fault tree, the authors found the ways in which individual components could cause a failure of the entire missile. To provide values for component failure rates, the technical report "Fault Tree Analysis" was used[90]. Figure K.1 displays the top level fault tree, along with the probabilities of failure.

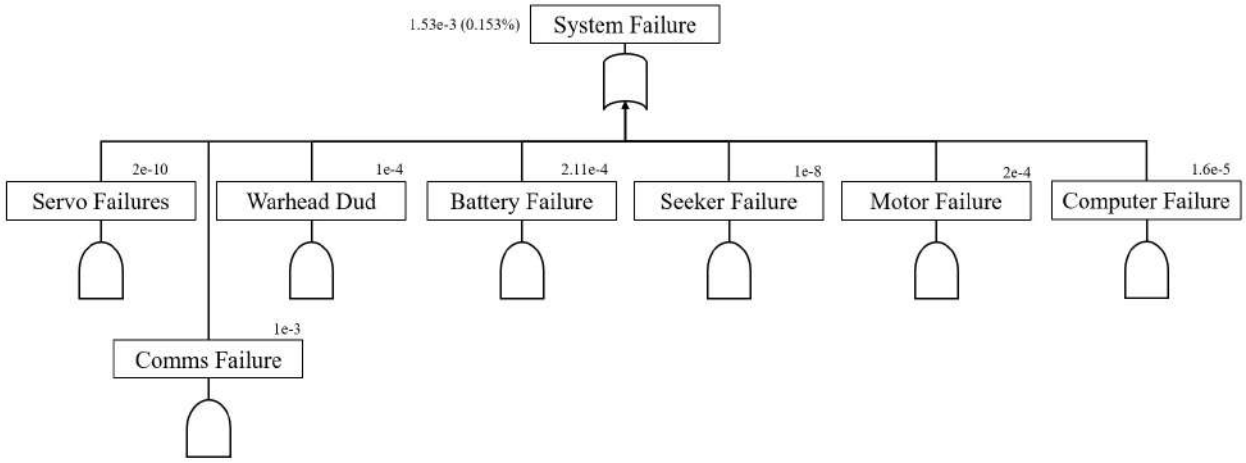

Fig. K.1 Top-Level Missile Fault Tree

Figures K.1, K.3, K.4, K.5, K.6, and K.7 show the subsystem fault trees for the servos, battery, seeker, motors, computer, and radio communications. From various online sources the dud rate of munitions is

approximately 1%, which has been used instead of exploring fault rates of munition components.

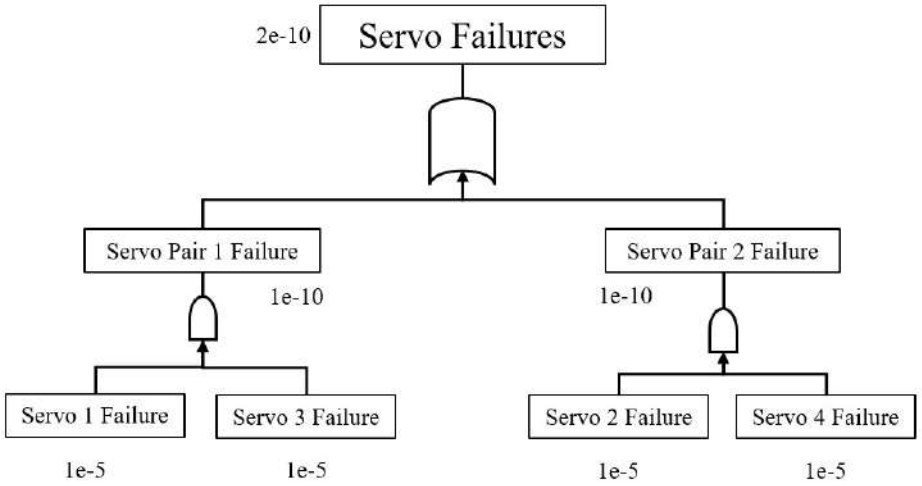

Fig. K.2 Servo Actuator Fault Tree

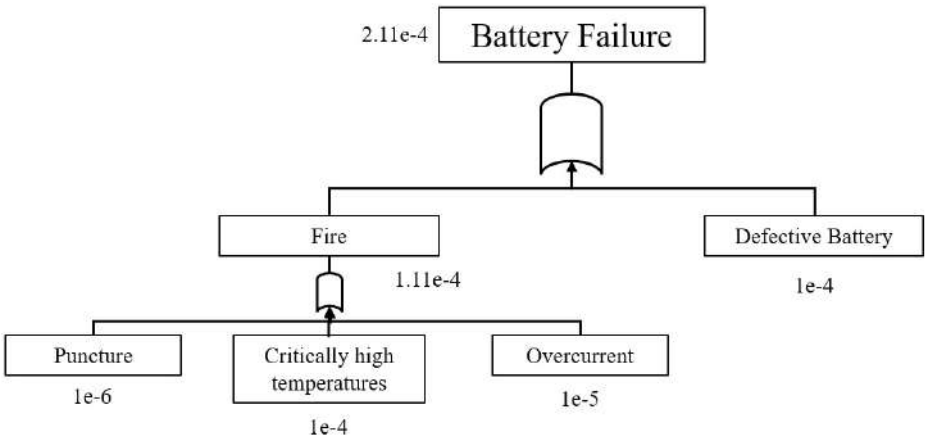

Fig. K.3 Battery Fault Tree

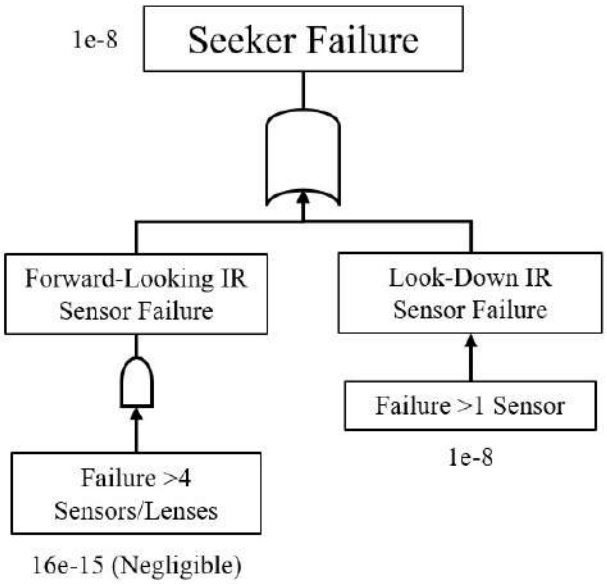

Fig. K.4 Seeker Fault Tree

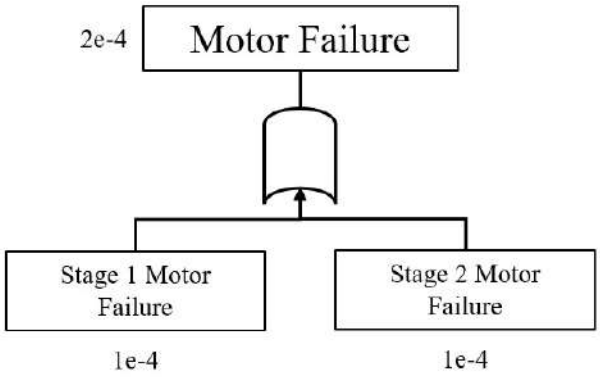

Fig. K.5 Motor Fault Tree

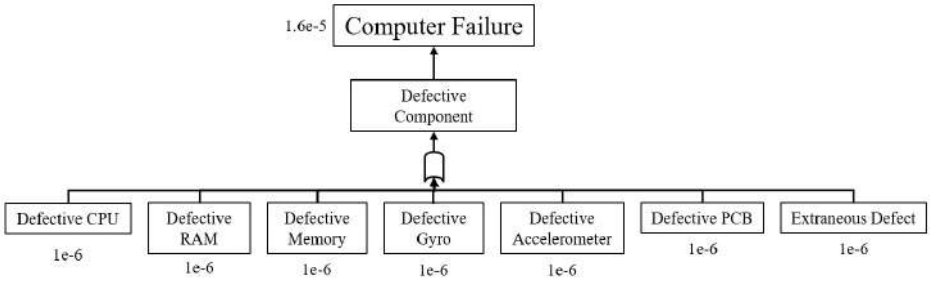

Fig. K.6 Computer Fault Tree

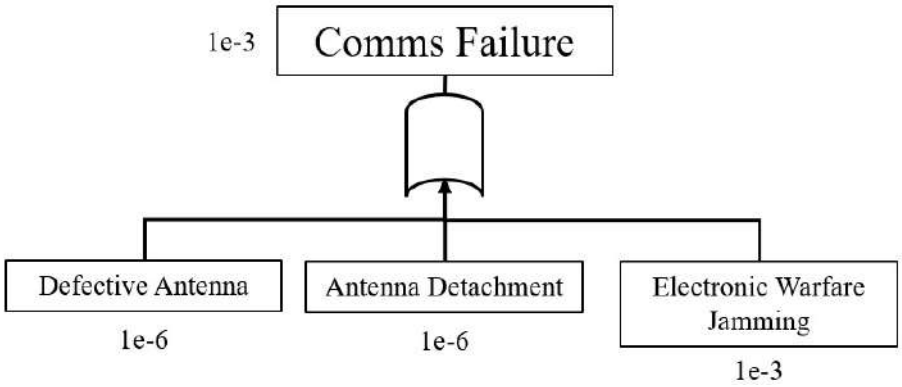

Fig. K.7 Communications Fault Tree

An additional fault tree (shown below in Figure K.8) was made detailing the rate of uncontrollable flights that carry the risk of harm to civilians. The acceptable rate of uncontrollable flights that could result in harm to civilians is set to one in a thousand. Note that dud rates of various munitions are typically in excess of 1%, which pushes the fault rate above the acceptable levels as it prevents a self-destruction. Therefore, the warhead dud rate must be set to 1 in 10,000 as a goal for a reliable design to be developed.

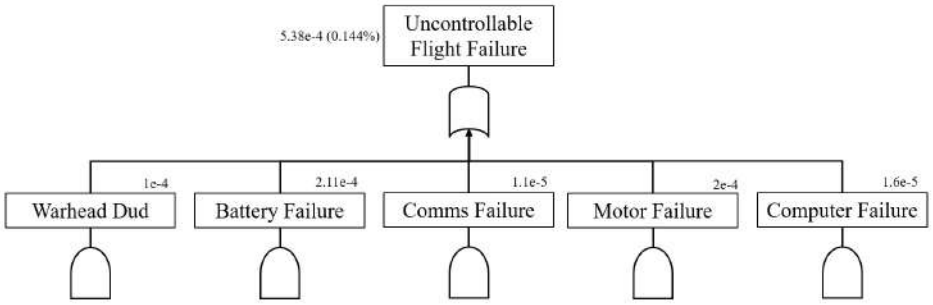

Fig. K.8 Uncontrollable Flight Fault Tree